

UNIVERSITÀ DEGLI STUDI DI GENOVA

SCUOLA POLITECNICA

DIME

**Dipartimento di Ingegneria Meccanica, Energetica,
Gestionale e dei Trasporti**



**TESI DI LAUREA MAGISTRALE
IN
INGEGNERIA MECCANICA**

**Thermomechanical and electromagnetic analyses on a
superconducting demonstrator magnet for Hadron
Therapy**

Relatore:

Chiar.^{mo} Prof. Ing. Alessandro Rebora

Correlatori:

Dott.ssa Stefania Farinon

Ing. Tuukka Lehtinen

Allievo:

Gianluca Vernassa

Marzo 2021

Analisi termomeccaniche ed elettromagnetiche su un magnete dimostratore superconduttore per adroterapia oncologica

Sommario

Il lavoro di questa tesi consiste nell'analisi strutturale ed elettromagnetica di un magnete dimostratore superconduttore per il progetto GaToroid al CERN (Organizzazione Europea per la Ricerca Nucleare). Il magnete in oggetto è il frutto degli sforzi congiunti del dipartimento di ingegneria meccanica (EN-MME-EDS) e di quello di tecnologie (TE-MS-MDT) del CERN, ed ha lo scopo di validare modelli e tecnologie disponibili allo stato attuale volti alla realizzazione di un gantry per adroterapia oncologica. La tesi ripercorre le fasi di sviluppo del magnete e presenta le relative conseguenze strutturali, in termini di stato di tensione, ed elettromagnetiche, in termini di mappa di campo magnetico, che ne derivano. Il risultato è un modello numerico multifisico che verrà sottoposto a breve a validazione tramite misure sperimentali.

Thermomechanical and electromagnetic analyses on a superconducting demonstrator magnet for Hadron Therapy

Abstract

The work of this thesis consists in the structural and electromagnetic analysis of a superconducting demonstrator magnet for the project GaToroid at CERN (European Organization for Nuclear Research). The magnet is the result of the joint efforts of the Mechanical Engineering (EN-MME-EDS) and Technology (TE-MS-SC-MDT) departments of CERN. Its purpose is to validate models and technologies currently available for the realization of a novel gantry for hadron therapy. This thesis traces the development phases of the magnet and presents its consequent responses in terms of stress state and field map. The outcome is a multiphysics numerical model that will be soon compared to experimental evidence for validation.

Table of Contents

1. Introduction to Hadron Therapy	1
1.1. A timeline of Radiotherapy and Hadron therapy	1
1.2. Physical and biological effects of accelerated ions	4
1.2.1 Linear Energy Transfer (LET)	8
1.2.1 Relative Biological Effectiveness (RBE)	9
2. Technical aspects of hadron therapy and the GaToroid idea.....	10
2.1 Accelerators for hadron therapy	10
2.2 Gantries for hadron therapy	13
2.3 Availability of hadron therapy treatment facilities	16
2.4 GaToroid	17
3. The GaToroid Project	19
3.1 Components of the GaToroid gantry.....	19
3.1.1 Vector magnet.....	19
3.1.2 Toroidal Gantry.....	20
3.2 Proton gantry	21
3.3 Carbon ion gantry.....	22
3.4 Demonstrator.....	25
4. Superconductivity	30
4.1 Basics of superconductivity	30
4.2 Superconductors type I and II	33
4.3 Superconductors for the GaToroid magnets	35
4.3.1 Practical superconductors for accelerator magnets.....	35
4.3.2 ReBCO Superconductors	35
4.3.3 Superconductors for the proton gantry	36
4.3.4 Superconductors for the C-ion Gantry	37
5. Finite Element Analyses	39
5.1 The general framework	39
5.2 Mechanics	43
5.3 Electromagnetics	44
5.4 Modeling techniques	46
6. Demonstrator mechanics.....	48
6.1 Geometry.....	48

6.2	Material models.....	58
6.2.1	Elastic properties.....	58
6.2.2	Thermoelastic properties.....	59
6.2.3	Mechanical strength of ReBCO tapes.....	61
6.2.4	Resin inserts.....	61
6.3	Load case scenarios and boundary conditions	62
6.4	Analyses' results	64
6.4.1	Bolts' preloading.....	64
6.4.2	Cryogenic cooldown	65
6.4.3	Powering and magnetic forces	71
6.5	Second design iteration	72
6.5.1	Results.....	73
7.	Demonstrator magnetics	77
7.1	Preliminary studies and validation of the finite element approach	77
7.2	Field calculations on the curved geometry.....	79
7.3	Field calculations with cable jumps	82
7.4	Magnetic instrumentation positioning.....	84
	Conclusions.....	90
	Bibliography	91
	List of Symbols	94
	Appendix A.....	97
	Appendix B	98

1. Introduction to Hadron Therapy

This chapter is an introduction to hadron therapy from a historical and phenomenological point of view. First, the chronological evolution of the therapy is presented in contraposition to the relatively more common radiotherapy. Then, the main characteristics of the interaction between particles and organic matter are introduced, highlighting how heavy ions may have an advantage on other hadrons.

1.1. A timeline of Radiotherapy and Hadron therapy

Only a few months after their discovery in 1895, X-rays had already found their first use for diagnostic and therapeutic purposes. In early 1896, Emil Herman Grubbé attempted to treat a carcinoma with a machine built by himself at the Medical College of Chicago, before any understanding of the biological or physical characteristics of the ionizing radiation that was being used [1]. Such an improvised application, just like many others, was driven by the lack of treatments for some benign and malignant diseases that medicine and physicians were facing at the time.

Over the years, the joint effort of physicists, engineers, biologists, and medical doctors, spurred from the patients' needs for an effective disease control and life quality improvement, has brought to a better understanding of the tools being used, and their optimal use for patients' benefits.

Some authors [1] mark 1901 as the beginning of this discovery era when Becquerel and Curie (Fig. 1.1) reported on the physiologic effects of radium rays [2]. This work stimulated the speculations of many, and already in the first years of the twentieth century, many papers were written on radiotherapy and curietherapy, even though, complete knowledge of the mechanism and its biological implications was not developed yet.

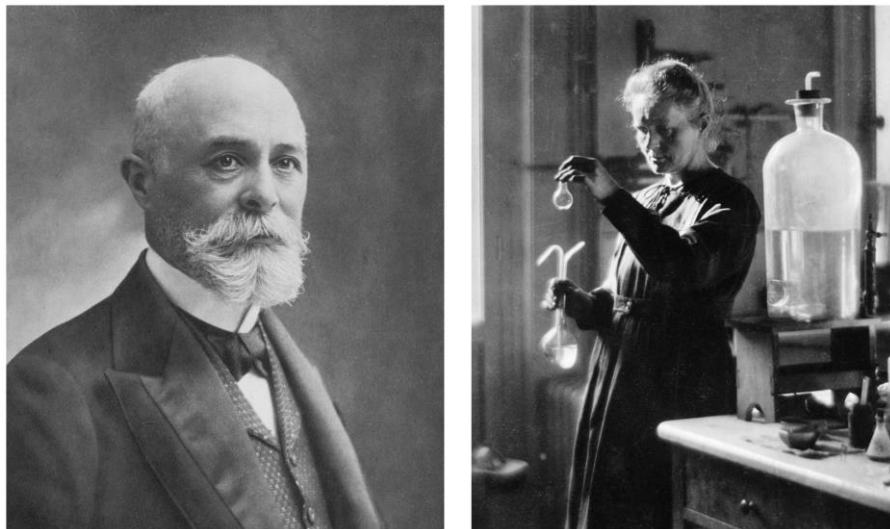


Fig. 1.1 – Henri Becquerel, left, and Marie Curie, right. Together in 1901 they first reported about the biological and physiological effects of ionizing radiations.

The years passed and scientists grew a better understanding of the fundamentals of such a phenomenon, namely the relationship between time of exposure and dose delivered on cell

survival. This culminated between 1927 and 1934 when Regaud and Coutard proposed a fractionated therapy, instead of a single large dose, for stopping completely the genesis of germinal cells [1]. Later, Coutard extended his studies to neck and head cancer, demonstrating how the same therapy induced significantly lower side effects than the ones from the single dose.

In parallel with the clinical and biological experimentations, also physicists made major discoveries, the most remarkable of which would be the atomic structure, with protons, neutrons, and electrons.

It is with Rutherford in 1898 that the concept of charged particle therapy begins. While investigating the spontaneous decay of heavy atoms into lighter ones, he detected two different types of radiations never seen before. He called them alpha and beta rays, which later, around 1907, he found out to be respectively a helium nucleus (He^{++}) and an electron (e^-). Then, in 1919, he demonstrated how nitrogen molecules under alpha radiations would expel hydrogen nuclei, named afterward as “protons”. Finally, the Rutherford-Bohr model of the atom was completed, and soon after it became the standard.

From the technological perspective, during this period high voltage transformers were developed, which combined with Coolidge’s tube, allowed the generation of higher-energy X-rays. As photons’ energy is associated with their depth of penetration, this allowed the treatment of deeper tumors. Up to then, only superficial ones could have been treated.

Super-voltage Coolidge tubes embodied the basic concepts of the more recent cyclotron, developed around 1929 by E. O. Lawrence. In 1932 this allowed the first pioneering in neutron radiation for medical treatments when John Lawrence and Robert Stone investigated the reactions and the elements generated by the bombarding of atoms of various elements by accelerated particles.

Finally, in 1940, the basis of electron beam therapy was established, when Kerst developed a machine, able to accelerate electrons up to 2 MeV, allowing this option to be practical and useful for therapeutic purposes.

During World War II medical research in particle therapy was highly set aside, and the major discoveries in the field of high energy physics were oriented to the nuclear bomb. However, this period formed figures such as Robert R. Wilson, who in the future would be considered as the “father” of hadron therapy, seen the major contribution he gave to this field. In 1946 Wilson would write [3] “Except for electrons, the particles which have been accelerated to high energies [...] have not yet been used therapeutically. [...] This has, in large part, been due to the very short penetration in the tissue of protons, deuterons, and alpha particles from present accelerators. Higher-energy machines are now under construction, however, the ions will in general be energetic enough to have a range in tissue comparable to body dimensions. It must have occurred to many people that the particles themselves now become of considerable therapeutic interest”.

Wilson’s work highlighted the particles’ interaction properties with matter, in particular with tissue of molecular formula $\text{C}_{0.5}\text{H}_8\text{O}_{3.8}\text{N}_{0.14}$, meaning a hypothesized composition of human bodies of 15% proteins and 85 % water, for a unitary density.

His notable theoretical studies showed how protons, or particles in general, are characterized by a maximum penetration depth, the so-called “range”. Such distance depends not only on the speed, or energy, of the particle but also on the composition of the tissue traversed and the nature of the particle itself. Curve I in Fig. 1.2 summarises these properties for protons, showing the energy required for them to reach a certain range. Curve II of Fig. 1.2 shows

instead the downside of the biological properties of ions. It plots the specific ionization, or the number of ions per centimeter of track, as a function of the proton's energy. Such quantity is directly connected to the biological damage produced and therefore is perhaps the most important biological property of this type of radiation.

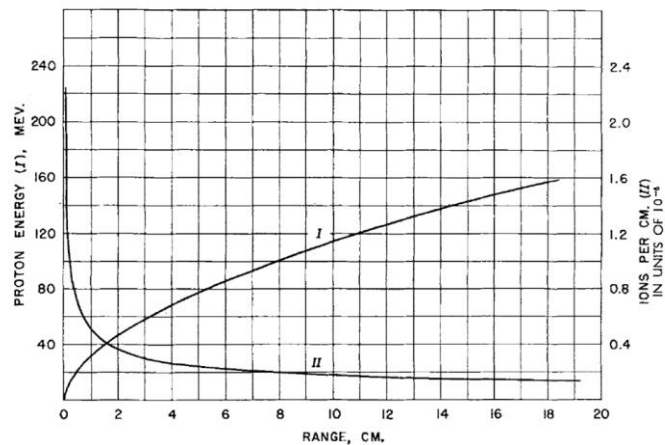
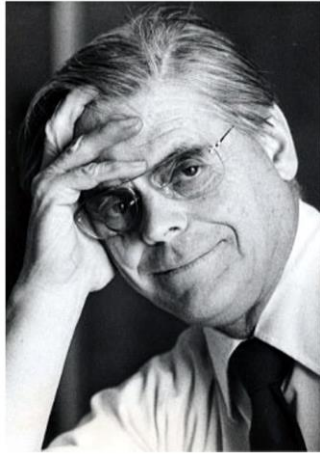


Fig. 1.2 – Left: Portrait of Robert R. Wilson. Right: graph from Wilson's article [3] showing the proton energy required to reach a certain depth, curve I, and the ions generated from the proton of a certain range, curve II.

Wilson himself proposed later in his article manipulation techniques for the graphs he provided, to adapt them for other particles at various energies, i.e. neutrons, alpha particles, and heavier ions.

From a practical perspective, such energy manipulation can only be achieved thanks to the synchrotron. First developed by Veksler in 1944, the new accelerator not only ameliorated the phase stability of the beam, in comparison with the cyclotron, but also allowed the variation of acceleration of charged particles, and therefore their penetration depth. This device is still nowadays at the heart of the therapy.

In the years ranging from 1950 and the 1980 major developments both in radiotherapy and hadron therapy were spurred by the continuous need of treating deeper tumors, giving birth to Cobalt teletherapy, which uses a Cobalt isotope able to produce gamma rays up to 1.3 MeV, and to megavoltage linear electron accelerators, that would be later employed in hadron therapy. However, the former technology still suffered some important limitations on the treatable tumors, mainly due to the side effects produced in normal tissues.

In fact, X and gamma rays were difficult to control in their path, due to scattering phenomena or trespassing of tumoral cells and damaging of normal cells. Attempting to overcome this issue, physicists and oncologists developed fractionated or multifield treatments, delivering a fractionated dose to a larger region. In this way, damage to safe cells was considerably limited. However, the integral dose delivered to the patient was increased. It became evident that the adsorption characteristics, and the natural interactions with normal tissues, were an intrinsic limitation of this therapy.

On the other hand, hadron therapy developed relatively slowly, not because of physical and biological implications, but mainly due to technical difficulties of beam delivery. Milestones in this process were the first clinical use of a proton beam in Berkley, 1954, the development of proton-based Neurological Radiosurgery in Boston in 1961, the treatment of pituitary adenomas at Harvard in 1963, and the subsequent application of fractionated proton therapy.

In 1970 most of the biological prerequisites were already satisfied, but it was only in 1984 that the realization of the first hospital-based proton therapy facility was feasible. The turning point was the development of efficient digital imaging technology in the early 1980s' (computerized tomography) that, integrated with a digital ionization pattern visualization, allowed physicians to optimally define treatment plans, exploiting the beam delivery line capabilities in terms of source directions and energies.

From the physicists' point of view, there was the interest of investigating the effects of heavier hadrons than the hydrogen nucleus, such as helium ions, or even the employment of pi-mesons (particular hadrons made of a quark and an antiquark). However, these found applications only in specific treatments such as bone sarcomas, and no evident advantages were arising clinically.

The few applications, together with the lack of an evident benefit, would not justify from the physicians' perspective the increased cost of developing new ways of delivering heavier ions. Therefore, the therapy struggled to materialize. From 1974 several scientists gave their contribution in this field of research, and as awareness grew among the clinical environment, many ion beam facilities found their way of being financed and are operating nowadays all over the world. A list of the operating treatment facilities in Europe can be found in appendix A.

1.2. Physical and biological effects of accelerated ions

Inside a living cell's nucleus, we find the deoxyribonucleic acid, the so-called DNA. Such acid is made up of a sequence of nitrogenous bases, namely adenine, thymine, cytosine, and guanine, ordered in a way that encodes all the genetic instructions necessary for the functioning, development, and replication of all known living organisms.

Nucleotides in the DNA are connected by hydrogen bonds, and their sequence forms the well-known double-helix structure, seen in Fig 1.3. When replicating, each cell transmits the genetic information by duplicating its DNA. The two strands of the helix separate, and each filament, composed of a single sequence of nucleotides, acts as a model to produce its counterpart. Bombarding cells with ionizing radiation damages the strands of the DNA, either by removing electrons from its atoms, with X and Gamma rays, or by directly breaking the strand, with protons and heavier ions. Fig. 1.3 offers a pictorial summary of such mechanisms.

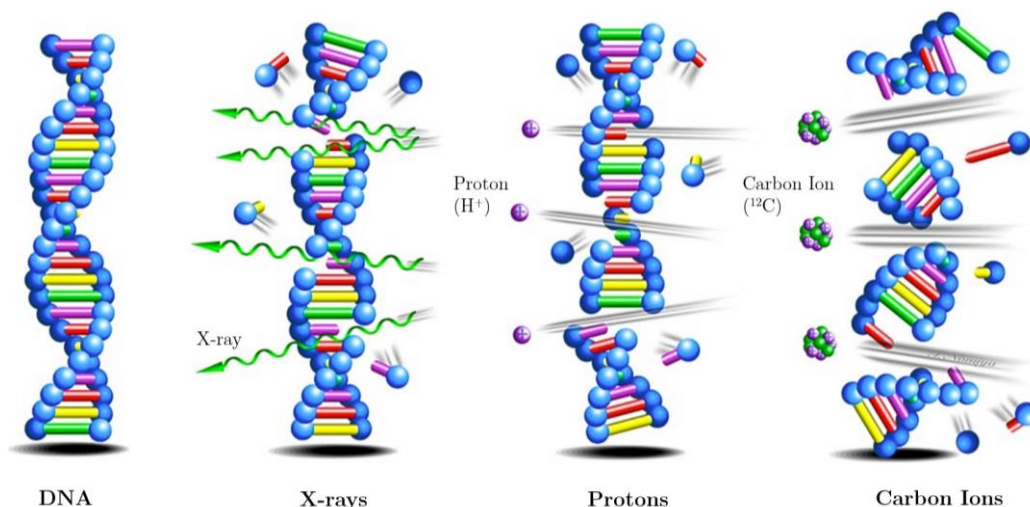


Fig. 1.3 – Pictorial summary of different effects of ionizing radiations on DNA strands [4].

Damage to the DNA greatly reduces the capability of a cell of generating daughter cells. However, in case only one strand of the helix was interrupted, the other strand could help to complete the sequence. The latter is the case of photons, which generally cause damage to the single nucleotide, therefore not ensuring the complete death of the cells. A first fundamental difference is therefore that ion treatment is much more biologically effective, since ions hit the strands more effectively, causing irreversible damage.

A second fundamental difference underlies between radiation and hadron therapy, that is due to the nature of the interaction of the particle involved with matter. Photons used in radiotherapy transfer only a part of their energy to the tumor, through Compton scattering, photoelectric processes, and pair production phenomena. Due to these effects, photons entering a medium are highly scattered immediately after the outer skin and spread out rapidly. This effect is represented by the black curve in Fig. 1.4, which reports the relative dose, or relative deposited energy, by 21 MeV photons when passing through water.

Hadrons instead interact with matter mainly through electromagnetic interaction, i.e. Coulomb forces. The energy loss per unit path length, or stopping power, is described by the Bethe formula¹, to which the effects of the interactions between the ion projectile and the tissues electrons must be added.

As a result, hadrons are characterized by low values of entry doses, and suddenly a sharp rise and fall of deposited energy density, immediately before they come to rest, at end of their range. Such a peak is the well-known Bragg peak, which embodies the benefits of hadrons instead of X-rays. Fig. 1.4 Also shows the relative dose for 150 MeV protons and 270 MeV C-ions, respectively in green and blue.

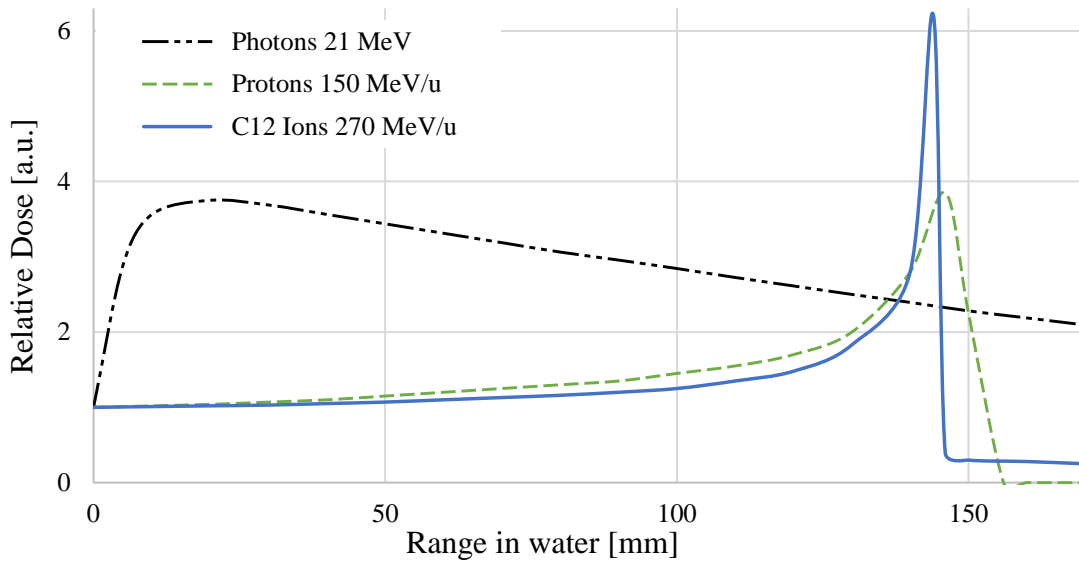


Fig. 1.4 – Relative dose, or relative deposited energy, for 21 MeV photons, 150 MeV/u protons, and 270 MeV/u C-ions in water. Curves for protons and ions also show the well-known Bragg peak, that strongly characterizes hadron therapy.

¹ The energy loss is given by $\frac{dE}{dx} \approx Kn_0 \frac{Z_{eff}}{\beta^2} \left[\ln \left(\frac{2m_e c^2 \beta^2}{I(1-\beta^2)} \right) - \beta^2 \right]$ where n_0 is the electron density of the target material, Z_{eff} the effective charge of the projectile ions, β is the relative velocity of the projectile with respect to the speed of light c , I the mean ionization energy of the target atoms and m_e the mass of the electron.

It emerges that hadrons have a strong advantage on photons, that is that they are suitable to reach tumors at basically any depth in a human body but causing less damage than photons to the surrounding healthy tissues, Fig 1.5.

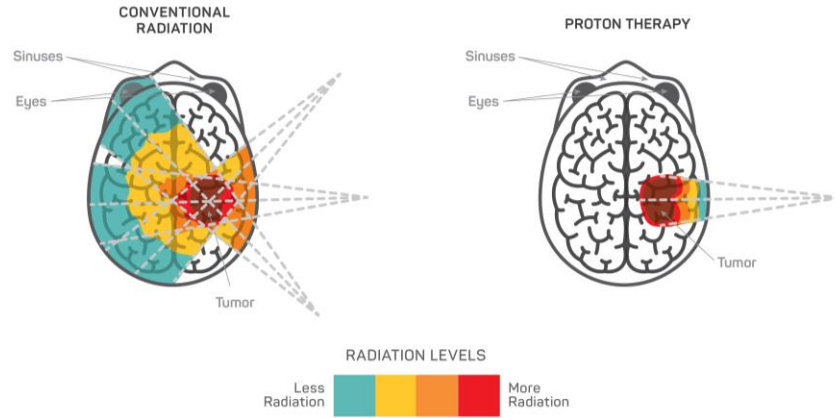


Fig. 1.5 – Integral dose delivered through conventional Radiotherapy (left) and Hadron therapy (right) [5]. Color contours are used to visualize the relative dose delivered to healthy tissues.

The position of the Bragg peak varies as a function of the energy of the particle, as shown on the left of Fig. 1.6, as well as their nature, as shown on the right of Fig. 1.6, since different species have different energy depositions. Moreover, the peak shape changes as a function of the penetration depth. The more particles penetrate in tissues, the more stochastic their interaction would be with target atoms. This phenomenon due to scattering processes is known as straggling and is responsible for the smoothing of Bragg's peak as range (or energy) increases.

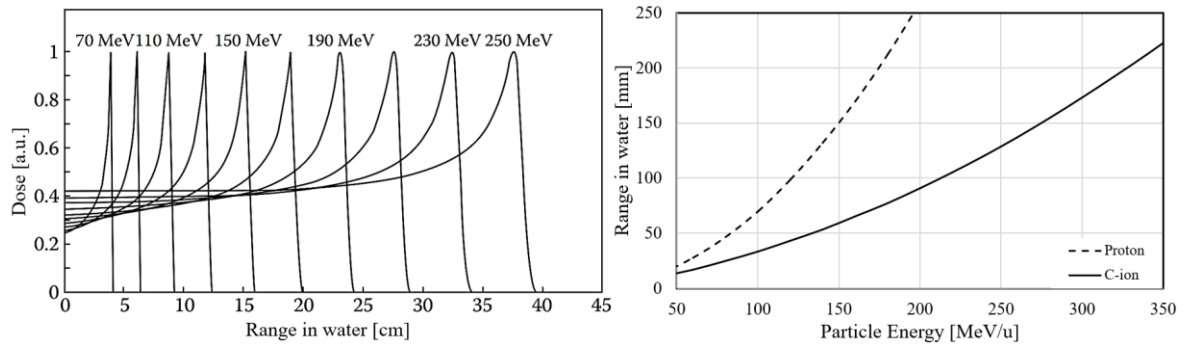


Fig. 1.6 – Left: Bragg peaks for protons at various energies. The smoothing of the peak is the so-called “straggling” effect [6]. Right: penetration depths as a function of the energy for protons and C-ions [7].

Fig. 1.6 gives us also the chance to better understand the energies involved in hadron therapy. Assuming a desired penetration depth of 25-30 cm, which, considering a multi-angled particle beam, allows covering the majority of the interior of a human body, we see that approximately 200 MeV are required for protons and around 350-450 MeV for Carbon ions. This helps an expert reader to understand the order of magnitude of the machines, accelerators, and magnets, involved.

The peculiar shape of the Bragg peak, and its energy dependence, can be exploited to further improve the precision and effectiveness of hadron therapy by using the so-called “Spread Out Bragg Peak”, SOBP Fig. 1.7.

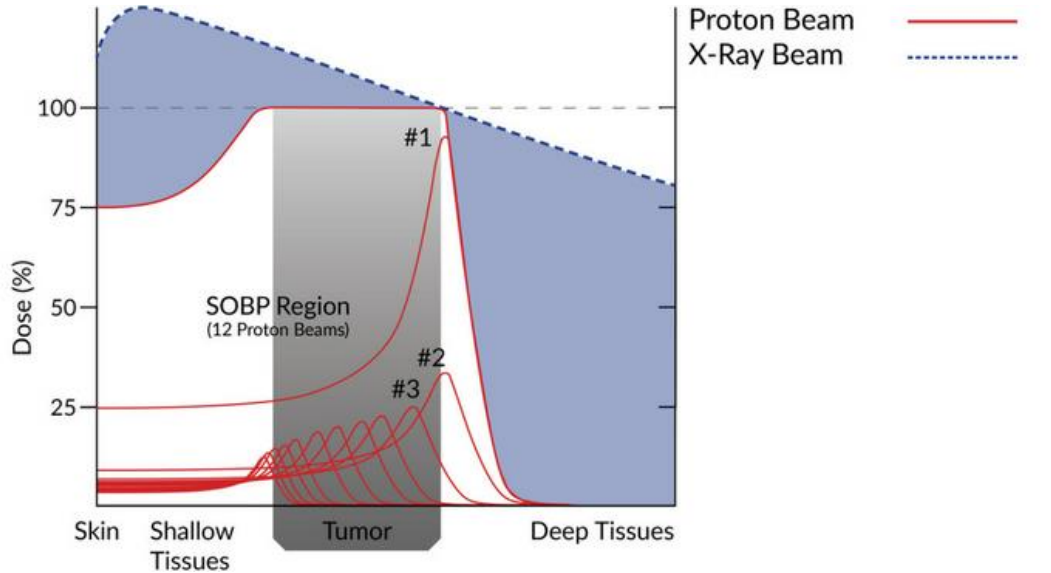


Fig. 1.7 – Spread Out Bragg Peak (SOBP) [5]. The characteristic of hadrons to let the total dose be the superposition of those delivered at different energies. Healthy tissues are spared of much parasitic dose. See the comparison between the white area, for protons, and the blue one, for photons.

By sending hadron beams at different energies the total dose delivered would be the sum of each. The volume integral dose then acquires a significantly different shape compared to that of photons. From the schematization, we can deduce how hadron beams have lower entrance doses, i.e. the dose delivered to tissues preceding the tumor, and almost null exit dose, the dose delivered to those succeeding the tumor. Only the region in which the tumor will be located will see the “plateau”, modulated in depth depending on the tumor extension.

The superposition of different doses is not restricted to the depth dimension only but can be exploited in 3D to give even more beneficial effects. It is the idea of collimating angled beams towards a focusing point, in which the superposition of the doses would create a “hotspot”. This technique follows the principles of the so-called “Gamma knife”, ideated by Lars Leksell in 1968, where gamma rays generated from a cobalt isotope were guided stereotactically towards the focusing point [8].

Nowadays the same principle is applied to hadron therapy, with the advantage of delivering multi-angled fractionated doses, thus reducing the unwanted damage to healthy cells, and obtaining a better 3D mapping of the target tumor, Fig. 1.8.

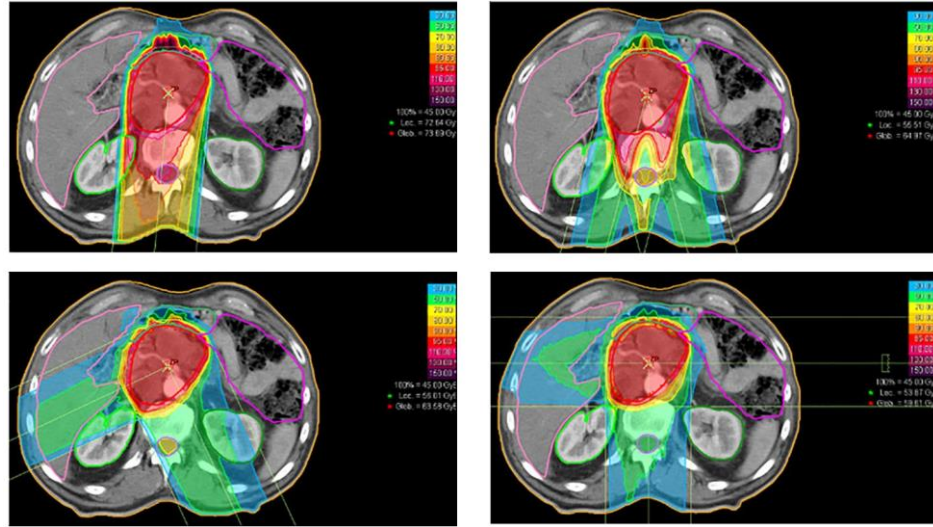


Fig. 1.8 – Various level of delivered doses depending on fractioning [9]. Top left: dose delivered to tissues along the path of a single beam. Others: doses delivered adopting multi angled fractionated doses.

To quantify the differences between photons and ions beyond the qualitative discussion above, two physical quantities need to be calculated. Below the Stopping power, or Linear Energy Transfer (LET), and the Relative Biological Effectiveness (RBE) are presented.

1.2.1 Linear Energy Transfer (LET)

Stopping Power and LET are parameters that allow quantifying the induced damage of ionizing radiation on a certain type of matter. The two parameters are essentially the same, since the Stopping Power describes the amount of energy absorbed by a certain material when crossed by the ionizing radiation. On the other hand, LET quantifies the energetic loss by the latter when interacting with matter. Essentially, they are complementary views of the same property, since they both measure the density of energy deposited as a function of the position in the tissue. In oncological applications, LET describes the density of interactions with healthy and tumoral cells. Therefore, peaked LET is preferable to a distributed one, since allows to effectively deposit a large fraction of the particle's energy in tissues at a precise depth. Fig. 1.9 expresses graphically this statement.

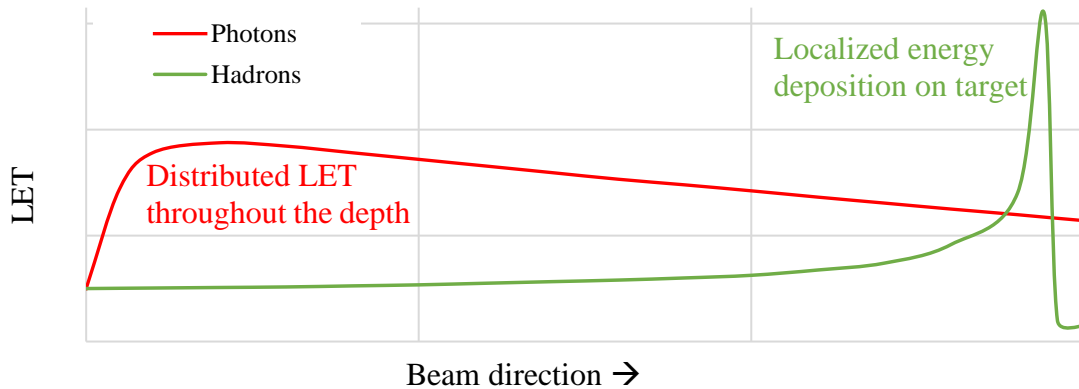


Fig. 1.9 – Comparison of the Linear Energy Transfer of photons and hadrons as a function of depth in matter.

1.2.1 Relative Biological Effectiveness (RBE)

This quantity is the biological effectiveness of certain ionizing radiation or particle, compared to the effects of the same physical dose delivered by a reference radiation. Therefore, it is a “Relative” value. Usually, the references are 250 kV X-rays or Co₆₀ gamma rays. High values of RBE mean lower doses required to achieve the same effects of the reference radiation on tissues. Therefore, high RBE values are preferred, since allows to spare healthy tissues from unwanted damage.

It must be noticed that the physical principles behind the interaction of ionizing particles with matter are still largely debated. It is a very complex and controversial topic of discussion, in which many variables are involved: the energy and nature of a particle, the nature and metabolism of a cell, etc. Therefore, predicted values of RBE are still far from being reliable. However, on a statistical basis, the typical values of RBE can be listed for the most common ionizing radiations and particles, tab. 1.1, and their effects can be translated into the following graphs of Fig 1.10.

Tab. 1.1 – Typical RBE values for the most common ionizing radiations and particles

Photon	Neutron	Proton	Pion	α	Heavy ions (C)
1	2 - 20	2	2	20	20

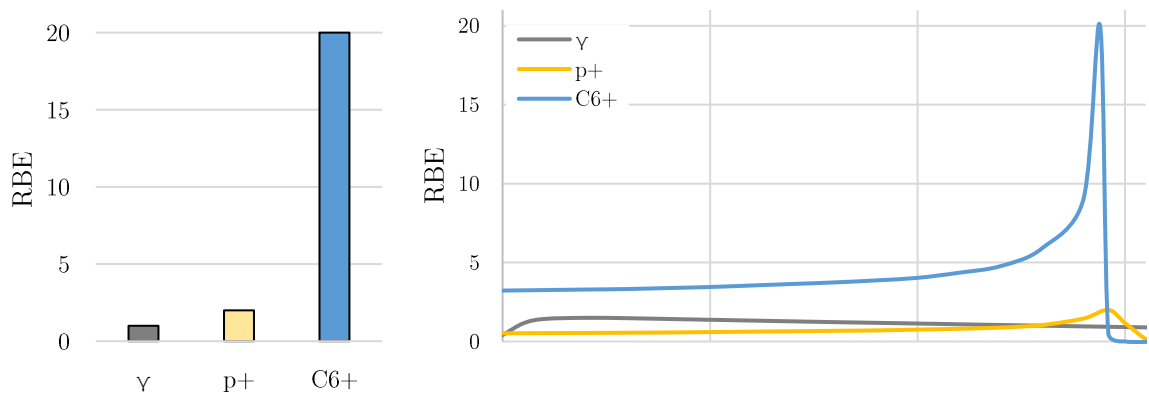


Fig. 1.10 – Graphs of the Relative Biological Effectiveness of photons, protons, and carbon ions. Graph on the left reports the peak RBE values, and the right graph shows the typical trend of RBE along the range in water.

With this quantitative review, the benefits of heavy ions emerge. Studies in the 1980s [1] demonstrated the benefits of C-ions due to the low-LET values on entrance and exit regions, and high-LET in correspondence to the Bragg peak. However, which ion for which therapy remains an open question. In 2008 Eickhoff and Linz would write “systematic experimental studies to find the optimum ion have not yet been pursued” [10]. Research is ongoing, and statistics in future years will lead us towards a rational selection of the particle of choice and treatment plan for a certain disease.

2. Technical aspects of hadron therapy and the GaToroid idea

In chapter 1, the advantages of hadron therapy have been introduced as compared to traditional radiotherapy. This chapter takes a more in-depth look at the technologies involved in the execution of such a therapy and presents, in light of these, the availability of clinics worldwide at the present time. Finally, the principles of the GaToroid project are introduced, showing how it fits in this framework.

2.1 Accelerators for hadron therapy

Most of the facilities operating in the heavy-charged particle radiation therapy use dedicated accelerators, designed on purpose to meet the treatment requirements [11]. Depending on the type of particle, and therefore of therapy, the accelerators range from traditional cyclotrons, synchrotrons, and linear accelerators to modern ones including advanced features, such as intensity modulation, gating, etc. These new functionalities are designed specifically to ameliorate the treatment plan, allowing the delivery of doses in a very homogeneous and conforming way to the tumor, accounting even for the natural movements due to breathing and heart beating.

A fundamental difference would exist between a cyclotron and a synchrotron, that is the modularity of the energy of particles. A cyclotron is a fixed-energy machine, designed to deliver particles at a given energy, while a synchrotron is able to accelerate particles to any energy between its minimum and maximum design energies.

The operating scheme of a modern cyclotron is presented in Fig. 2.1.

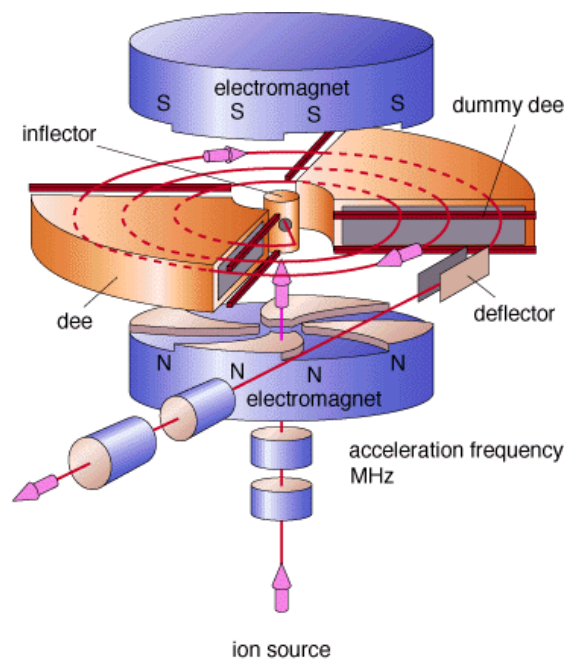


Fig. 2.1 – Pictorial representation of a cyclotron [12].

The main components of the machine are: an ion source (or multiple ion sources) to generate particles to be accelerated; an electromagnet, that can be resistive or superconducting to reduce the sizes of the machine; a radio frequency acceleration system (RF system), that accelerates particles by generating an electric field; and an extraction system (deflector), that guides particles to the delivery line. The system is continuously cooled and operates under vacuum conditions. As a result, the typical dimensions of a cyclotron are around 4 m in diameter.

The principle behind a cyclotron is that the revolution frequency ω of a particle rotating in a uniform magnetic field \mathbf{B} is independent of its velocity and revolution radius. This is given by the following formulae:

$$\omega = \frac{qB}{m} \quad \text{and} \quad f = \frac{\omega}{2\pi} = \frac{qB}{2\pi m} \quad (2.1)$$

Where q is the particle's charge, and m its mass. This frequency f usually falls in the radio frequency range (1-110 MHz) [11], and it can be synchronized with a sinusoidal electric field to accelerate the particle. As particles accelerate, the drift outward follows a spiral path, finally reaching the extraction point where an electrostatic deflector drives them towards the beam delivery line.

A strong advantage of the cyclotron is that it can accelerate particles of different energies at the same time, since the required RF frequency is constant, resulting in a continuous particle beam. On the other hand, the delivery energy is fixed at the design value, and in case of therapeutical applications, an energy degrader is needed for the modulation. This component is essentially a variable thickness polycarbonate wheel, that can be rotated in different positions to absorb variable fractions of the particles' energy. Its major drawback is the radioactivity induced by the collisions, and the beam intensity losses, that can account up to 98%. Therefore, the intensity from the cyclotron needs to be increased as the energy is degraded [11].

A synchrotron instead can cover a whole range of particle energies, thanks to the fact that particle beams are discontinuous in time, and each branch can be accelerated independently to the desired speed. This greatly simplifies the system, since the degrader and the radiation shielding equipment are no longer needed. On the other hand, particle beams are pulsed, and generally no more than 1×10^{11} particles can be delivered every two seconds [11]. A scheme of the Siemen's synchrotron for the Heidelberg Ion-Beam Therapy Center (HIT) is presented in Fig. 2.2.

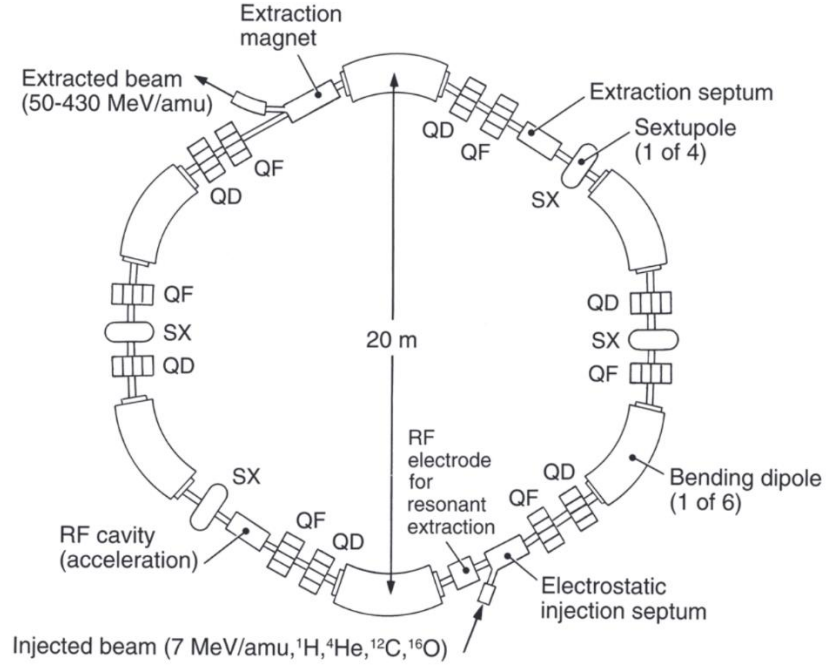


Fig. 2.2 – Schematization of the Siemens heavy ion synchrotron for HIT [11].

All synchrotrons require an injection line that brings a beam inside its orbit at a precise energy. Usually this consists of a radiofrequency quadrupole accelerator (RFQ), reaching around 3 MeV, and sometimes followed by a linear accelerator (so-called “linac”) that brings particles up to around 7 MeV. Particles that entered the synchrotron orbit always around the same radius, and the magnetic and electric systems are synchronized with the revolution frequency and speed to keep them along this path. A radio frequency (RF) cavity is responsible for accelerating the particles, by producing a sinusoidal electric field. The magnetic system modulates the field intensity to steer the particles depending on their speed. When the desired energy is reached, the dipole field is maintained constant and a betatron deflects the beam horizontally out of the ring, towards the delivery line.

The synchrotron’s intrinsic ability of modulating the energy of the beam makes it usually preferable for clinical applications [11]. In addition, other interesting features are under development to make it even more suitable for therapies. One among many, a gating procedure that allows the synchronization of the beam delivery with the patient’s respiratory cycle [11], maximizing the precision with which the particles are delivered to the target tumor.

2.2 Gantries for hadron therapy

It has been remarked how the benefits of hadron therapy are even more enhanced when the particles are delivered from different directions. However, for practical reasons, the particle accelerator needs to be fixed, and therefore the system needs to be adapted.

Moving the patient around fixed beamlines has been attempted, but it resulted in an uncomfortable treatment procedure for the patient himself and it also brought in many further complications due to the non-negligible movements of internal organs. These are such that the prediction on the tumor's position is often far from reality, especially if considering the natural movements associated with heartbeats and breathing. Achieving the correct energy deposition would be therefore an impossible task. Hence the idea of a moving patient has been rapidly abandoned.

Nowadays, two techniques seem to be established for delivering the dose from multiple directions. The first way is to have different beamlines, with particles generated from independent accelerators, and delivered to the focusing point from as many delivery lines. Several treatment rooms, such as CNAO in Pavia (IT), have adopted this technique, which requires a significant economic investment since the accelerating technology needs to be duplicated. Also, the logistics are much affected as this option requires building a wholly dedicated facility. Fig. 2.3 offers a schematization of a plant for such multiple beamline-treatment rooms in the case of Carbon ions.

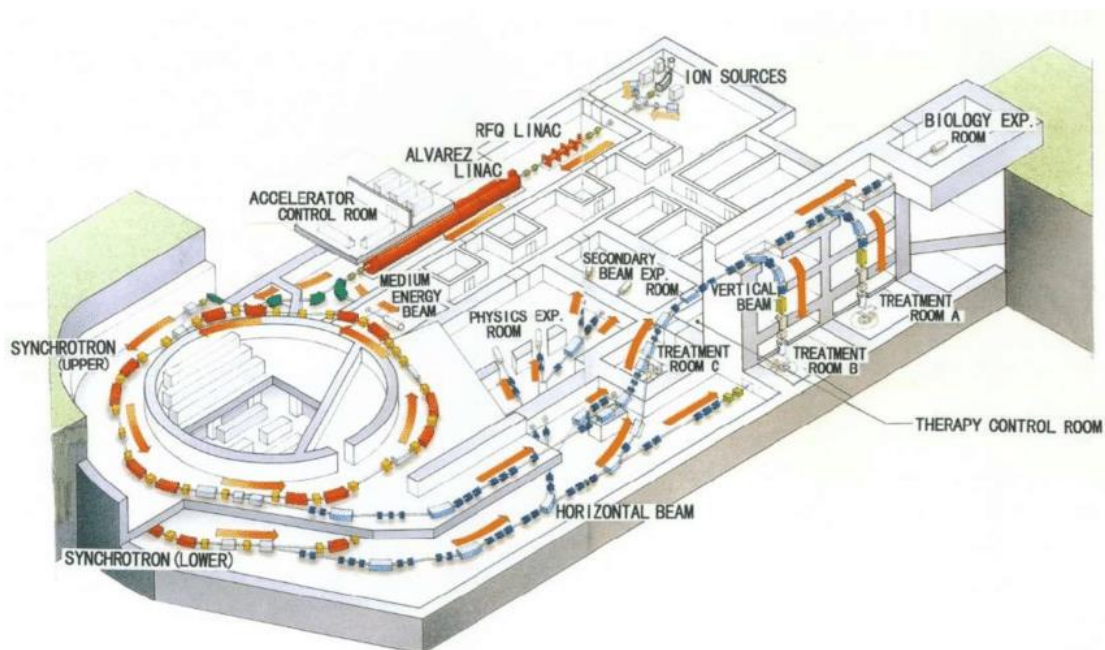


Fig. 2.3 - Plant view schematization of the multiple delivery lines-treatment room at HIMAC: Heavy Ion Medical Accelerator in Chiba (Chiba, JA). [13].

The investment grows even more if we desire more than two beam delivery lines. Considering then the overall trend of performing multiangled treatment plans, this option

seems to not only being financially unsustainable, but also to not being exploiting the full advantages that a painting procedure would offer.

The second option attempts to overcome the apparent complications and limitations of multiple, fixed beam delivery lines, by introducing a rotating structure, namely the gantry, receiving particles from a single accelerator and bending them towards the patient. By rotating, the angle from which the dose is delivered changes, and in principle the range of delivery directions available is the whole spanned by the gantry. The idea of this latter treatment plant is schematized in Fig. 2.4.

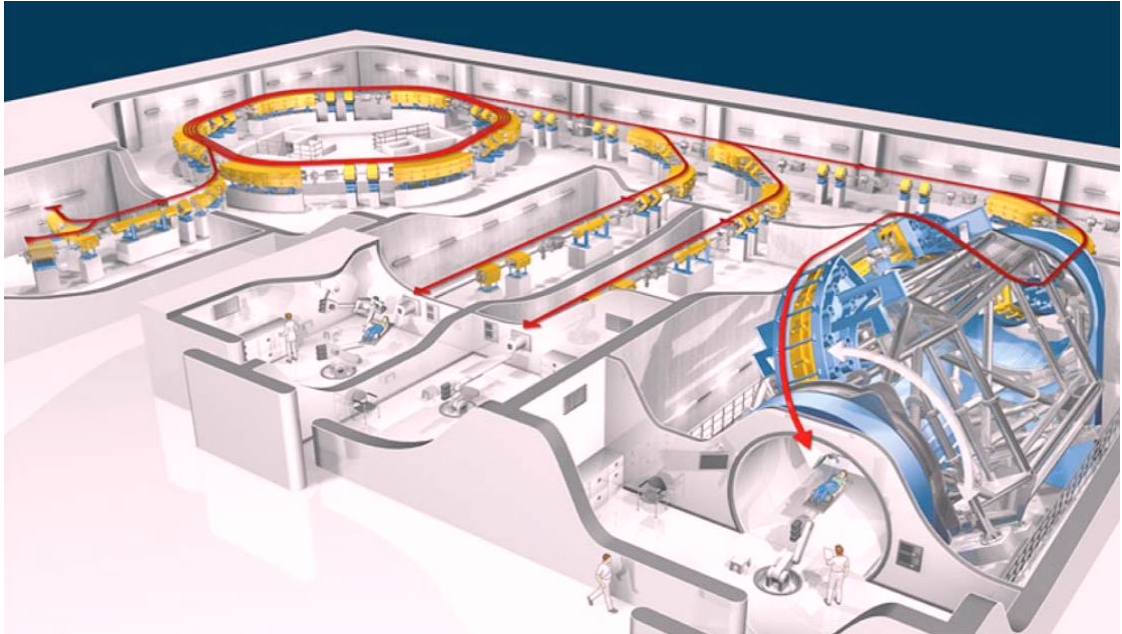


Fig. 2.4 – Schematized plant view of a treatment facility with a single beamline (in red) and a rotating gantry (in blue) at the end of it [14].

This option seems to be more appealing nowadays, and technology in this field is developing relatively quickly. Major challenges come out of the fact that the devices able to bend the beam are magnets, usually bulky, and therefore for the gantry to be precise, it needs to be extremely stiff. It is the case of what has been done at Heidelberg Ion-Beam Therapy Center (HIT), Fig. 2.5, where the gantry carries 3 resistive magnets, with peak field values of 1.8 T. Covering a length of 25 m and a diameter of 13 m, this gantry exceeds 600 tons in weight, most of which originated from structural needs required to meet stiffness requirements.



Fig. 2.5 – Picture of the HIT rotating gantry [15].

The magnetic field can reach significantly higher intensities by exploiting superconductivity. This is the case for the machine built for the HIMAC in Chiba, Fig. 2.6. With around 2.88 T of peak field, all the devices' dimensions can be substantially reduced, and therefore the device's weight. The HIMAC gantry is only 13 m long, 10m in diameter, with a total weight of 350 tons.

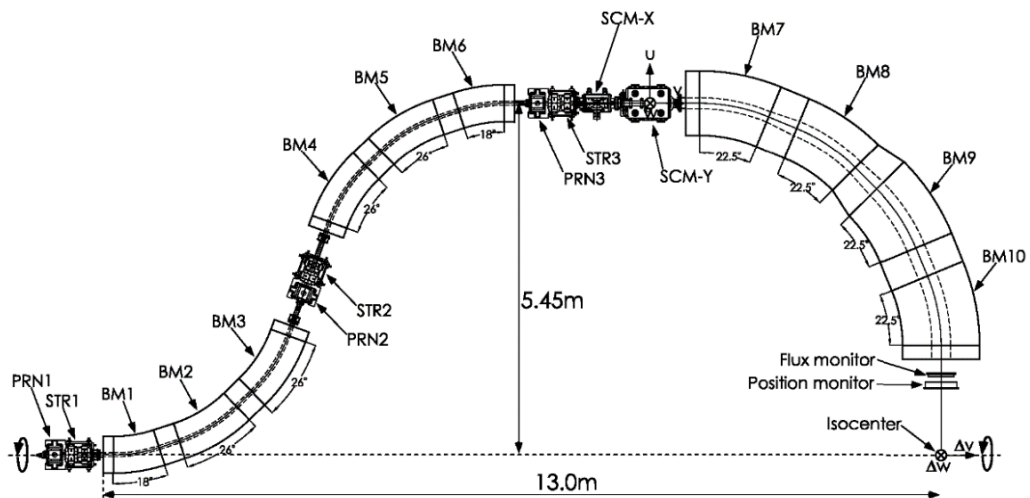


Fig. 2.6 – 3D model of the NIRS rotating gantry, with superconducting magnets along the delivery line [16].

2.3 Availability of hadron therapy treatment facilities

Overall, the stiffness requirements for these machines result in large and bulky structures. The financial investment is significant, and it is associated mainly to the accelerator, the gantry and a completely dedicated building to host them. In light of these facts, hadron therapy struggles to find its way in clinical applications, and therefore is not well established yet. Consequently, only few cases have been treated giving birth to little statistics.

Until 2019, patients who benefited from hadron therapy accounted for just over 220 thousand, of which only 16% were treated with C-ions. Specialists [17] have estimated that approximately 50% of the newly diagnosed cancers could benefit from hadron therapy, which in the future could translate into 10 million people out of the 20 million cancer cases foreseen in 2030. In principle, hadron therapy has better therapeutical potential in the 15-20 % of cases. Therefore, in this hypothetical picture of 2030, 2 million patients per year could benefit from hadron therapy, compared to the 20 thousand patients/year of modern radiotherapy.

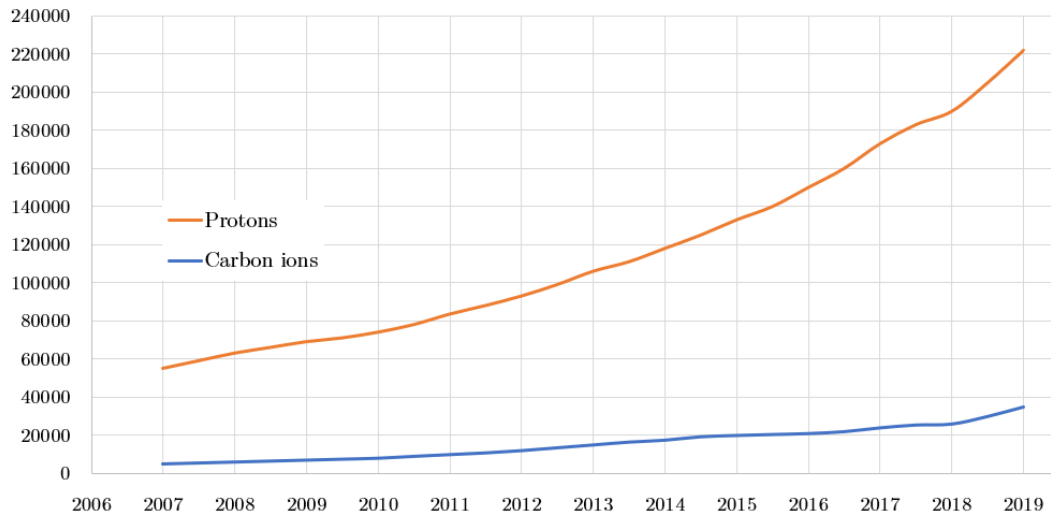


Fig. 2.7 – Patients treated with protons and carbon ions worldwide [18].

From the physicians' point of view, the lack of statistics represents the main concern, and considering the cost of this therapy being more than one order of magnitude higher compared to modern radiotherapy, this keeps them from investing time and resources in developing new treatment plans and facilities.

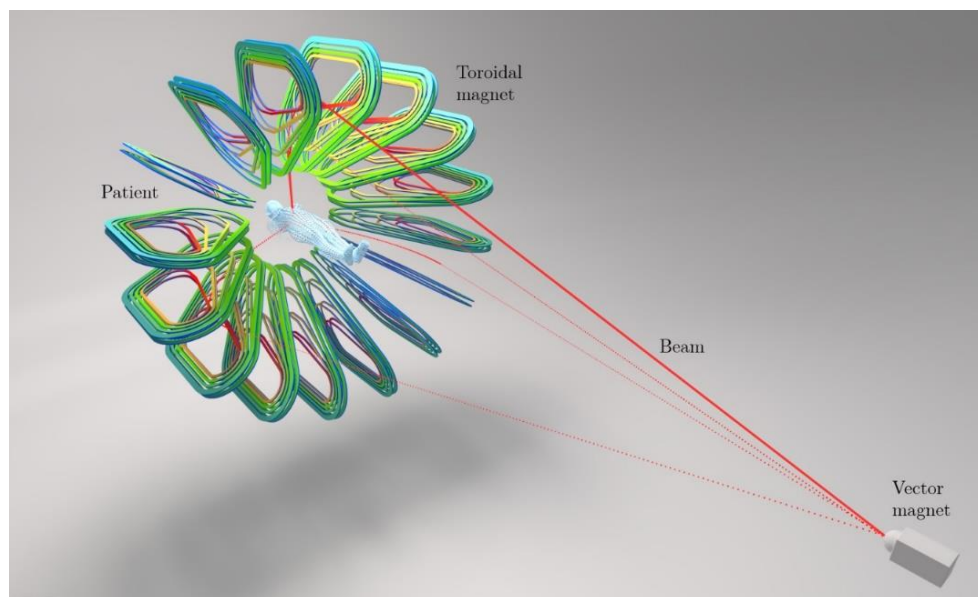
In February 2021, 105 facilities for hadron therapy could be counted worldwide, against 14 200+ facilities for traditional radiotherapy [19]. Out of these 105, 38 are in Europe, with 34 proton therapy facilities and only 4 C-ion ones. The latter are [18] in Heidelberg (GER), Pavia (IT), Wiener Neustadt (AUT), and Marburg (GER). A picture of the locations of European's hadron therapy facilities is represented in Fig. 2.8.



Fig. 2.8 – Availability of Hadron therapy facilities in Europe [19].

2.4 GaToroid

GaToroid is a project born out of the idea of Luca Bottura (CERN) about a revolutionary beam delivery system for hadron therapy based on a steady-state, axis-symmetric field configuration. Instead of the traditional rotating gantries, that would carry resistive or superconducting magnets to send particles from different directions, here the magnet has a toroidal shape, covering the 360 degrees around the patient, and the choice of the treatment direction is driven by a fast in-plane beam kicker called "vector magnet". A schematization of the system is presented in Fig. 2.9.



*Fig. 2.9 - Schematic representation of the components in the GaToroid system.
(Photo courtesy of Daniel Dominguez, CERN Design and Visual Identity Service).*

Several practical benefits arise from such a configuration. The toroidal magnet is static, therefore the gantry designated to accommodate them can be much simpler as any rotation is excluded.

The peculiar shape of the magnets allows them to have large acceptance, meaning that they can receive particles of different momentum to charge ratio p/q . This is given by the combination of the specific magnetic field generated by a torus and the adoption of a grading system for the windings. As a result, particles arriving from different angles can still be bent precisely to the target tumor.

The steady-state nature of the magnetic field, enabled by the aforementioned large acceptance, allows more feasible use of superconducting materials, with all the benefits in terms of weight, field intensity, and footprint that are derived from that.

Finally, the delays in the delivery of beams of different energies and from different directions only depend on the accelerator's ability to generate such particles or the vector magnet's performance in changing rapidly the steering direction.

Depending on the clinical and therapeutical requirements, the toroidal magnet can be varied in the number of coils and dimensions. This allows calibrating the magnets for the required number of treatment directions and the acceptance for the desired ions. Finally, the bore diameter can be varied to accommodate different patient moving or digital imaging systems.

The result has the potential of a relatively simple, lightweight, cheap alternative to traditional gantries that could make hadron therapy more feasible for many facilities. In the next chapter, we take a more in-depth look into the main components of the GaToroid system.

3. The GaToroid Project

In this chapter, we present the main components of the GaToroid system. Then we look at the different configurations for protons and C-ions. And finally, we introduce the demonstrator magnet, the subject of the mechanical and electromagnetic analyses of this thesis.

3.1 Components of the GaToroid gantry

For simplicity, we introduce at this point some reference coordinates that allow us to better explain the scope of the different components. We choose to define a Z direction, coincident with the torus axis, and therefore any plane perpendicular to such axis could be arbitrarily referred to as an X-Y plane. We also define the radial coordinate R as the distance of any arbitrary point from the Z-axis, and θ , representing a generic circumferential direction around the same axis.

3.1.1 Vector magnet

This component bends the particles coming from the beam line of the accelerating system towards the toroidal magnetic field. The circumferential position θ of the particles at the exit of the vector magnet determines the treatment direction. The particle beam's angle with respect to the Z-axis, namely α_e , determines the path length of the particles in the magnetic field. Since in this configuration, a longer path means a higher integral field on the particles, different energy particles can be sent along different paths to reach the same focusing point on the patient, within a certain angle tolerance.

Higher energy particles (around 250 MeV for protons and around 450 MeV for C-ions) are bent to higher α_e 's; their path is more prolonged, allowing the magnetic field to complete the bending process. Instead, lower energy particles (approximately 70 MeV for protons and 120 MeV for C-ions) require less integral field to be bent. Therefore, their α_e 's are such that the path in the magnetic field becomes shorter.

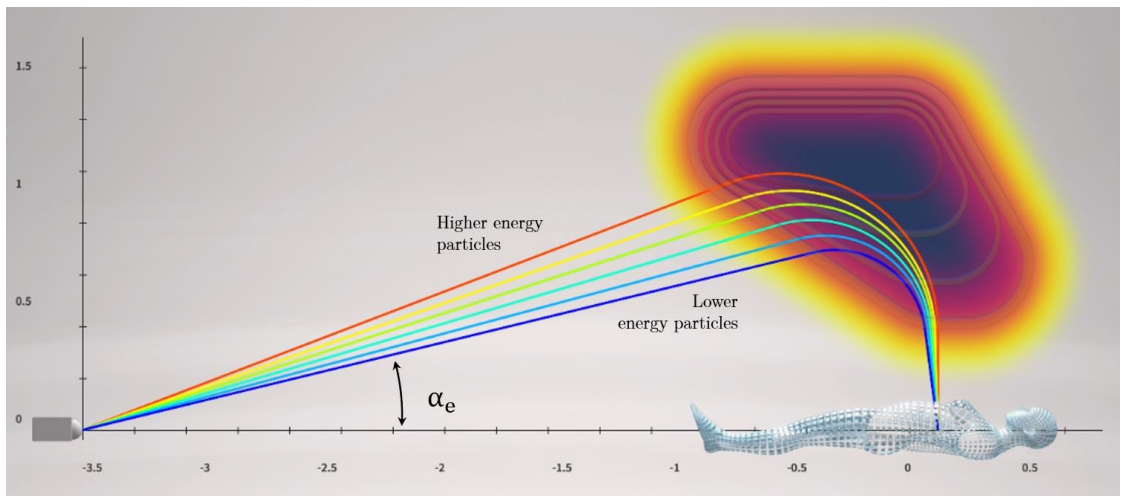


Fig. 3.1 – Schematic of the GaToroid magnet acceptance.

Without entering into details, the concepts behind the latest design of the vector magnet are the following. The three primary functions required from the device are bending the particles depending on their energy, rotating the beam depending on the desired irradiating direction, and steering the beam for painting² the target tumor.

These functions can be assigned separately to three different devices. So far, the most attractive idea is to have two resistive magnets delegated to operate the X-Y switching and subsequently a large aperture superconducting magnet that could finally bend the particles towards the toroid.

3.1.2 Toroidal Gantry

The gantry itself comprises a set of N coils, disposed at fixed angles θ around the Z-axis. The space between neighboring coils is left free so that N channels are defined for the beam passage. As a result, the radiation angles, and therefore the treatment directions, are discrete. However, statistics on the actual treatment plans adopted in several hadron therapy facilities have shown that, on average, the need for a high number of treatment angles is quite low; hence, the GaToroid magnet angles' discretization is not considered a limitation.

The peculiar shape of the coil is the result of an optimization process. Indeed, the ideal magnetic field configuration would be one in which the field inside the torus is constant in the three directions, R , θ , and Z . This would significantly simplify the coil configurations. However, only due to the geometrical configuration, there is a reduction in reluctance near the internal radius that translates with a field intensity that goes with $1/R$ inside the torus, as shown in Fig. 3.2a.

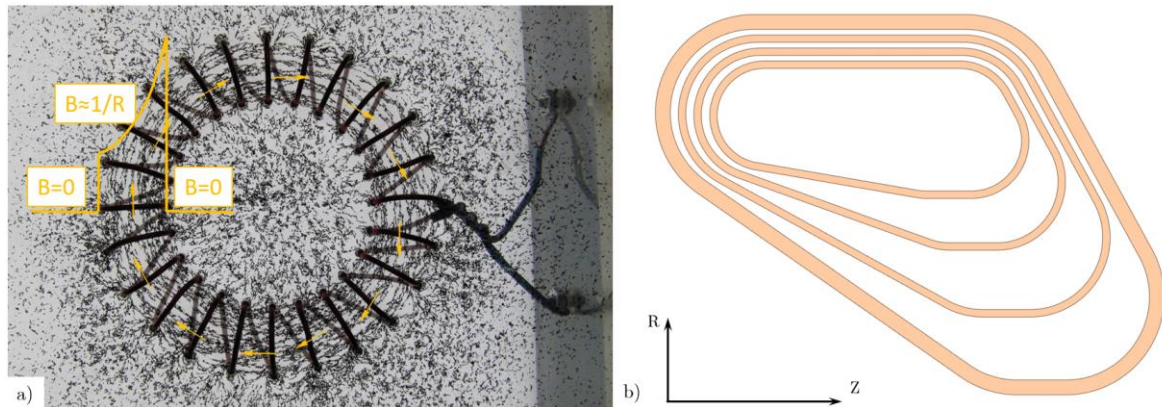


Fig. 3.2 – Schematic of the principles behind GaToroid magnets. To the left a visual representation of the magnetic field inside a torus, and to the right the ideal geometry of the GaToroid coils for proton gantry.

By introducing the grading system, of which Fig. 3.2b shows a representation, we can reduce the field intensity when R tends to the internal radius of the torus. Ideally, an infinite number of grades should be implied to achieve a perfectly constant field intensity inside the torus, but once again, optimization studies demonstrated a compromise between complexity and

² Painting is an expression used to describe the action of “scanning” the section area of a tumor from a given direction. In practical terms, this means moving the focusing point of few millimeters in the plane perpendicular to the beam, to cover entirely the tumor.

adequate field quality. Two versions of GaToroid have been considered so far: a version compatible with proton therapy, and one for ion therapy. In the next two paragraphs we detail the characteristic properties of the two coils separately, starting with the gantry for protons and subsequently the one for carbon ions.

3.2 Proton gantry

The design for protons firmly considers the requirements for the therapy and the characteristics of the magnetic system to minimize complexity and costs. We have already seen in Fig. 1.6 (on the right) how protons with energies between 70 and 250 MeV are practically able to reach any depth in a human body. Given the minor integral field required to bend the particles and considering that we have superconducting materials that allow to reach higher field intensity and increase the magnet acceptance, the size of the system can be dramatically reduced. The optimized design sees an internal bore to host the patient with a diameter of 0.8 m, which is the same size as state-of-art Magnetic Resonance Imaging (MRI) systems. The external diameter is 3.3 m, and the torus is composed of 16 coils. Table 3.1 lists the fundamental characteristics of the proton gantry.

Table 3.1 – Characteristic dimensions and parameters of the GaToroid proton gantry.

Parameter	Detail
Coil	
Number of grades per layer	5
Number of layers	4
Coil Length/Height/Thickness [m]	1.7 / 1.3 / 0.05
Operating Current [kA]	1.8
Engineering current density [A/mm ²]	100
Peak magnetic field [T]	6.8
Torus	
Number of coils	16
Stored energy [MJ]	31
Bore diameter [m]	0.8
External diameter [m]	3.3
Torus length [m]	1.7
Vector Magnet position [m]	3.6
Appr. mass (cold mass / cryostat) [tons]	12 / 17

Fig. 3.3 illustrates a rendering of the proton gantry to give a qualitative representation of the magnet size compared to the average size of a human.

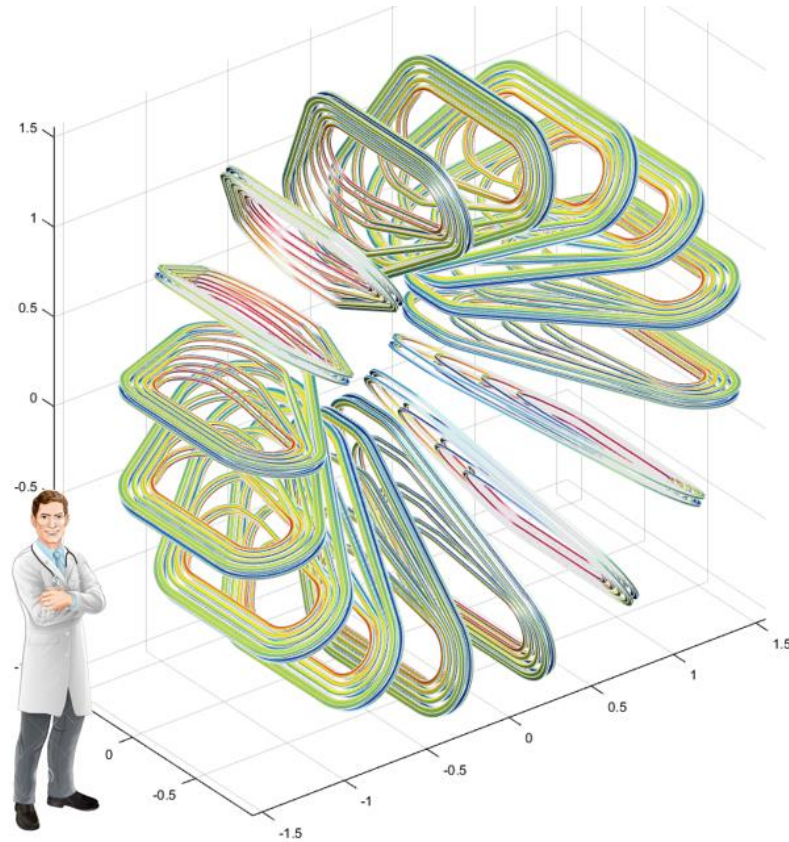


Fig. 3.3 – Rendered image of the proton gantry coils. The schematic uses a 1.8 m tall doctor for size comparison.

3.3 Carbon ion gantry

The carbon ion gantry attempts to meet all the requirements requested by clinics to profit as much as possible of the therapy capabilities. The resulting design embodies all the modern knowledge and technologies into a complete and complex system. Therefore, the differences between this gantry and the smaller proton version are dramatic. Crucial points are the many treatment directions (≥ 20) and an internal bore region of more than 3 m in diameter. The latter is aimed to accommodate efficient imaging systems, and to allow the rotation of the couch for the patient, necessary to perform non-coplanar treatments.

The resulting baseline gantry sees therefore an external diameter of 12.8 m and an internal bore diameter of 3.7 m. The mass of the complete system is estimated to be in the order of 270 tons, but even more impressive is the previewed stored energy in the magnetic field of 1.3 GJ, comparable to one of the Large Hadron Collider (LHC) detectors' torus. The complexity and the size of such a machine, as we can grasp from Fig. 3.4, would not be far from those of traditional rotating gantries, and the benefits of a steady gantry would not be so evident.

Therefore, another option, namely the reduced-size version, is proposed, in which sizes and number of coils are at halfway between the proton and the baseline C-ion gantry. The number of treatment directions is lowered to 8, and the inner bore becomes 2.25 m. The resulting estimations of mass and stored energy are dramatically lowered, respectively 110 tons and 420 MJ. Table 3.3 lists the characteristic parameters of the two C-ion gantries.

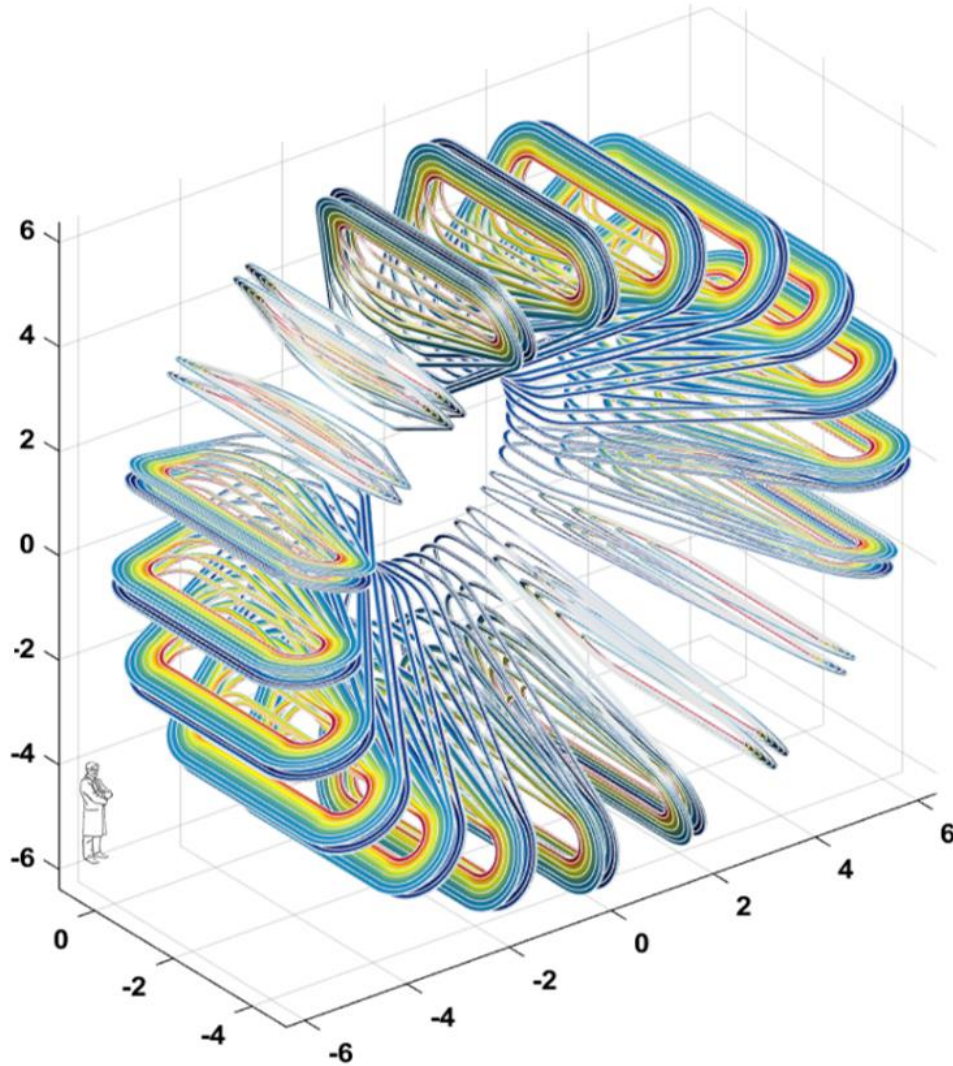


Fig. 3.4 – Render image of the C-ion gantry. Beside, a scaled figure of a 1.8 m tall human for size comparison.

Table 3.2 – Characteristic dimensions and parameters of the full size and the reduced size versions of the GaToroid magnet.

Parameter	Baseline Version	Reduced Size Version
Coil		
Number of grades per layer	6	6
Number of layers	2	2
Coil Length/Height/Thickness [m]	5.8 / 4.5 / 0.036	5.6 / 3.7 / 0.036
Operating Current [kA]	10.8	10.8
Engineering current density [A/mm ²]	68	74
Peak magnetic field [T]	6.1	6.7
Torus	Baseline Version	Reduced Size Version
Number of coils	40 (2x20)	16 (2x8)
Stored energy [MJ]	1300	420
Bore diameter [m]	3.70	2.25
External diameter [m]	12.8	9.7
Torus length [m]	5.8	5.6
Vector Magnet position [m]	9.2	4.2
Appr. mass (cold mass / cryostat) [tons]	270 / 29	115 / 17

3.4 Demonstrator

This paragraph introduces the demonstrator magnet, which is a 1:3 scaled model of the full-size coil for proton gantry, Fig. 3.5. The demonstrator's size has been chosen to fit in the already existing cryostats in the test stations at CERN, hence allowing powering tests at cold.

The interests in building such a prototype are not only related to the technology development but also to have experimental evidence of many different aspects, ranging from engineering calculations to quench protection.

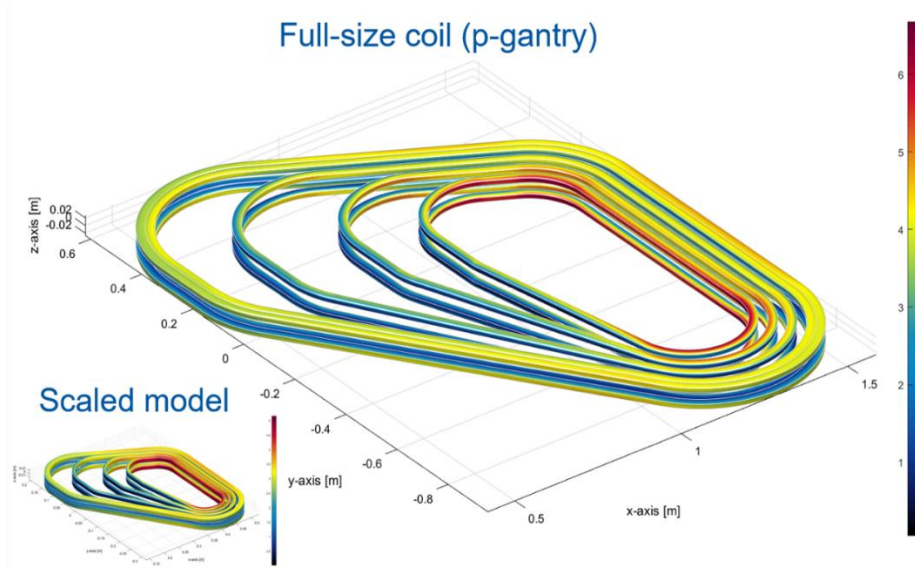


Fig. 3.5 – Schematic representation of the demonstrator magnet beside its full size proton gantry coil.

The demonstrator magnet sees two superconductors' configurations: one made with ReBCO tapes, and one with NbTi cable. The aim is not only to evaluate the magnet performance but also to develop and practice useful tools and processes that will be implemented in the construction of the full-size gantries. With this scope in mind, the whole project's workflow has seen a continuous interaction between the EN-MME-EDS (Engineering - Mechanical and Material Engineering – Engineering Design and Simulation) and TE-MS-CMDT sections of CERN (Technology – Magnets Superconductors and Cryostats – Magnet Design and Technology).

The coil, described in Table 3.3, comprises two quasi-symmetric layers in a double pancake shape, separated from each other by an intermediate plate made of stainless steel, and held together by two stainless steel cover plates. Each layer is made of 5 identical grades, separated by stainless steel spacers. The grades are composed of a stack of 4 cables, and only the two most outer grades are joined to form a single grade of 8 cables. Finally, at the edge of the two most outer grades, we find the so-called rims. Their purpose is to act as the mechanical outer support and containment for the coils. This includes maintaining their shape but also carrying the in-plane expansional forces produced by powering the coil. Naturally, they also work in cohesion with other mechanical components to form the general

structure of the demonstrator. In correspondence with the most inner grades, we also find a stainless steel pole that accommodates the layer jump between the two pancake layers And also serves as the template for winding the correct shape of the innermost grades.

Table 3.3. Main parameters of the GaToroid demonstrator in HTS.

Parameter	Detail
Number of layers	2
Number of grades per layer	5
Number of turns per grade	4
Size ($w \times h$) [m]	0.6 x 0.4
Scale	1:3
Cable length [m]	50
Inductance [mH]	0.64

The whole magnet is conceived to go through an impregnation process that bonds coils and spacers to form a monolithic structure. This process is required to ensure the rigidity of the system and prevent the relative motion of the internal components, which may eventually lead to quenches.

Some preliminary calculations on the magnet's mechanics were done to validate certain general concepts regarding manufacturing. The results of these led to the design and production of a dummy demonstrator would with stainless steel tapes around a 3D printed supportive structure. The design and fabrication of this prototype has not only validated the peculiar geometry of the coil, but also it has helped to develop appropriate winding tools.

The cable configuration for the High Temperature Superconductor (HTS) version requires the simultaneous winding of the 6 tapes (4 HTS and 2 Copper stabilizers) with adjusted tension from 6 different spools. For this reason, the TE-MSC-MDT section at CERN installed and commissioned a new multi-spool winding table, that allows dedicated tension control in 7 spools. A picture of the winding table is presented in Fig. 3.6.



Fig. 3.6 - View of the multi-spool winding table assembled in the TE-MS-MDT laboratory.

Once the tapes are stacked to form the cable, they must be wrapped with an insulating layer capable of allowing the necessary sliding between them. A glass fiber sleeve was selected as the reference insulation scheme with a backup option of using a C-shape layer of Polyimide. Both were successfully tested for winding on the winding table, Fig. 3.7.

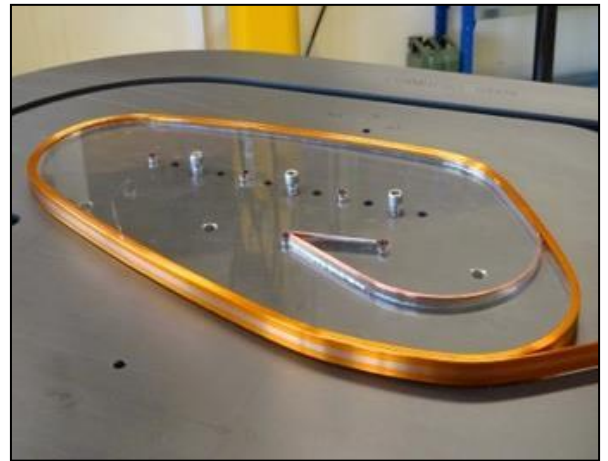
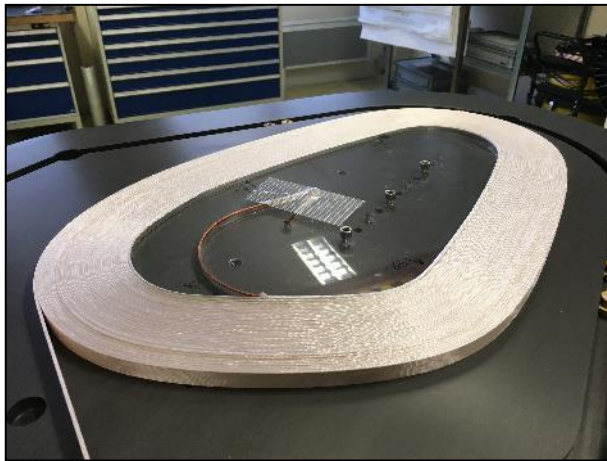


Fig. 3.7 - Winding tests with the 2 options of insulation schemes for the demonstrator: (left) fiberglass sleeve and (right) C-shape Polyimide.

The insulation has 2 main purposes: first, to maintain electrical insulation between the cables; secondly to create a suitable surface for the impregnation resin to adhere to while avoiding an excessive penetration of the resin into the cable.

Indeed, low thermal and electric contact resistances between the tapes constituting the cable must be kept facilitating heat and current sharing in case of a quench. The glass fiber can efficiently absorb the resin creating a strong adhesion between the cables and the spacers,

but it can lead to a relevant resin penetration and consequent loss of contact between the tapes. The geometrical opening of the C-shape, that allows the sliding of the tapes, could be also used by the resin to enter inside the cable and compromise the good contact.

The choice of resin, as well as the amount and the type of filler, can have significant effects in terms contact resistance between the tapes and adhesion to the external cable surfaces. For this reason, an experimental setup for the impregnation of 4 cables stacks was installed at CERN TE-MS-CMDT section for an exhaustive study to be carried out. The impregnation mold, shown in Fig. 3.8, would allow to prepare up to 3 stacks of 4 cables at the same time, varying the insulation scheme, the resin as well as the compression of the cable. The impregnated samples are visually inspected as well as electrically tested for insulation and contact properties. The best candidate will be selected for the demonstrator.

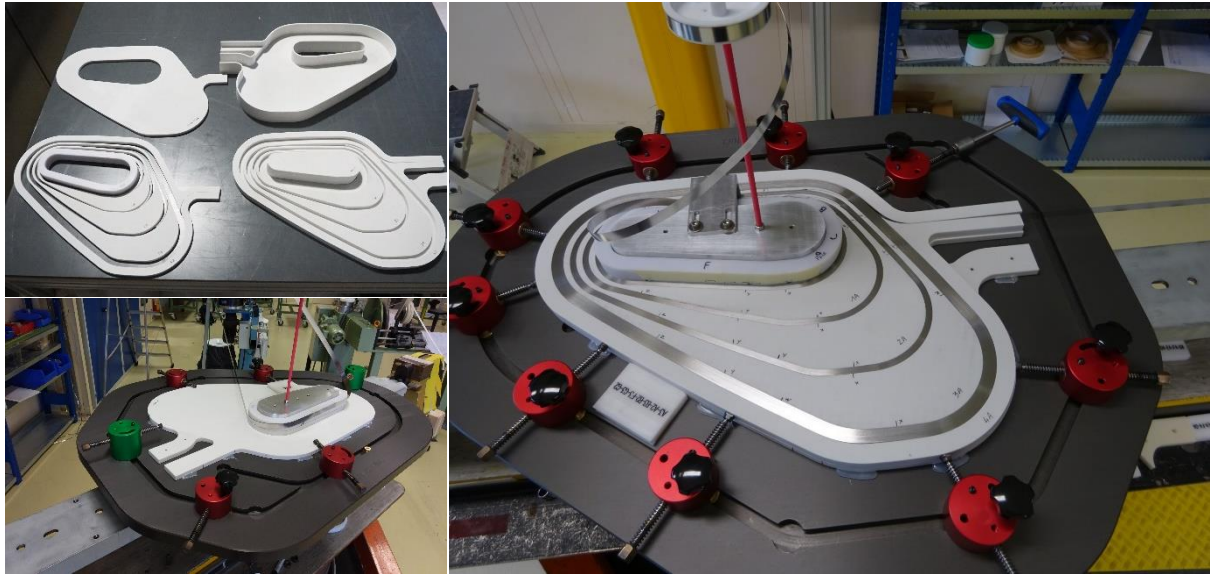
Samples of the impregnated cable stacks can then be used to assess the mechanical properties of the impregnated coils, such as the coefficient of thermal expansion (CTE), Young's modulus and yield strength in the three dimensions. These parameters will be used to refine the mechanical simulations.



Fig. 3.8 - Impregnation mold used for the 4 cables stack impregnation study and a batch of impregnated 4 cables stack.

As a step toward the HTS demonstrator construction, a first version of the demonstrator wound with stainless-steel tapes was built, to validate a first winding procedure and the design, as well as develop the required tools for the magnet assembly (Fig. 3.9Fig. 3.). Furthermore, during the winding process, it became evident how the transitions between the curved and the straight parts can generate waves³ in the conductor. The original GaToroid concept was conceived with a negative curvature. A new version was developed, where a more evident curvature in the spacers will allow a simpler and more accurate winding.

³ Details about this effect will be presented in chapter 6.



*Fig. 3.9 - First layer of GaToroid dummy prototype, wound in stainless steel tape on glass-filled nylon spacers (white), together with the winding plate (black) and the tooling (red).
Top left are the 3D printed spacers.*

4. Superconductivity

In this chapter, the peculiar characteristics of the materials used for the GaToroid magnet are presented. First, the phenomenon of superconductivity is introduced from a historical perspective, then the superconductors practically used for accelerator magnets are briefly discussed, and finally, the cable configurations for the GaToroid project are exposed.

4.1 Basics of superconductivity

In the first years of the twentieth century, the electric behavior of materials at low temperatures was not clear. For relatively small variations around room temperature, it was known that resistivity has different trends depending on the nature of the element. When lowering the temperature, metals, in which the conduction is due to a “gas” of free electrons, have a decreasing resistivity. This can be grasped if we think about the fewer interactions that electrons will have with the lattice structure of the metal, since its vibration decreases when cooled down. Semiconductors instead increase their resistivity when cooled down. This is because conduction electrons are the ones thermally excited to the conduction band: a lower thermal excitation leads to fewer conduction electrons. However, a complete understanding of materials’ behavior at cryogenic temperature was unknown. Three models were proposed by Lord Kelvin, Sir J. Dewar, and Matthiessen. The first was supposing that conduction electrons become free due to thermal vibration, and therefore resistivity should increase exponentially when tending to 0 K. In Dewar’s model electron would have not been obstructed in their path by the thermal vibration of the atoms, and therefore resistivity should have tended to zero. Finally, in Matthiessen’s model, which was then revealed to be the correct one, resistivity was ascribed to two separate phenomena, one related to the vibration of atoms (referred to as “phonons”) and one to the impurities included in the base material [20]. In this framework, if the concentration of imperfections is relatively low, resistivity is given by:

$$\rho = \rho_{\text{ph}} + \rho_{\text{res}} \quad (4.1)$$

where ρ_{ph} is the component associated with phonons, and ρ_{res} , the Residual resistivity, associated with imperfections. This latter varies with the concentration of impurities, lattice imperfections, and grain boundaries. In the case of non-superconducting materials, when reaching low temperatures (ideally 0 K) the phonons’ contribution annihilates and the total resistivity is only imputed to imperfections. In practice a parameter has been adopted to quantify this phenomenon, the Residual Resistivity Ratio (RRR), that also gives a direct indication of the purity of a material [20]. Its formulation is:

$$\text{RRR} = \frac{\rho_{300 \text{ K}}}{\rho_{0 \text{ K}}} = \frac{\rho_{\text{ph } 300 \text{ K}} + \rho_{\text{res}}}{\rho_{\text{res}}} \quad (4.2)$$

It is around 1910 that Heike Kamerlingh Onnes started leading experiments to characterize materials at very low temperatures. Indispensable prerequisites for these studies were his attempts to liquefy helium, that has a boiling temperature in atmospheric pressure of 4.2 K,

in which he succeeded in 1908, reaching the lowest temperature ever achieved on earth at that time, 1.5 K. In 1911 he was then to investigate resistivity at temperatures near the absolute zero. In particular, adopting Matthiessen's model, he was about to measure the phonon branch of resistivity, and he was carrying experiments on gold. The practical difficulties of obtaining high purity gold, spurred him to consider the distillation of mercury as a valid alternative, and eventually he came out with the experimental evidence shown in Fig. 4.1 [20].

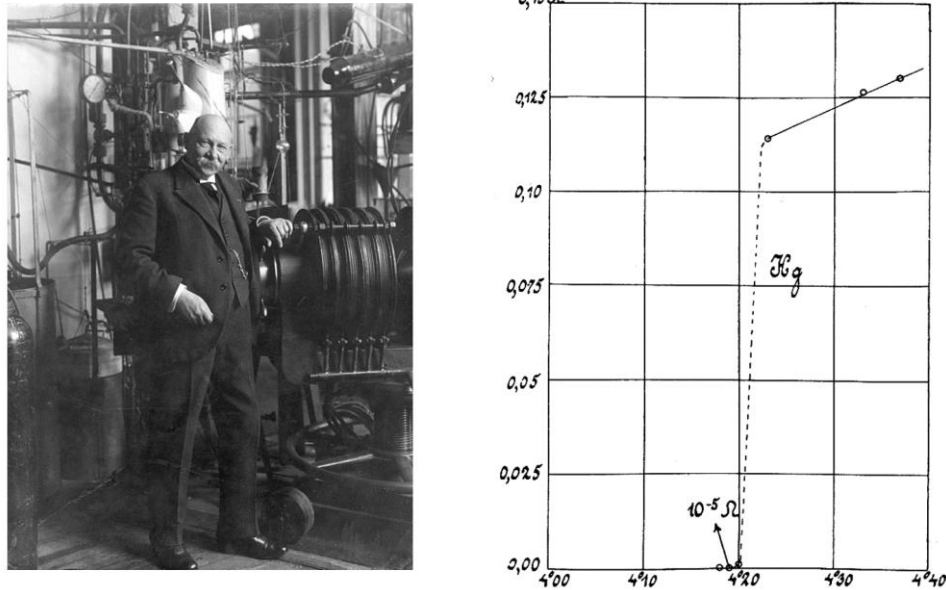


Fig. 4.1 – [21] Kamerlingh Onnes next to his apparatus to cool helium to liquid form (left) and the resistance (Ω) versus temperature (K) of mercury [22].

The graph reports the resistance of a small tube filled with mercury, and both Onnes and his mentor, Professor Johannes Diderik van der Waals, were astonished in finding out the abrupt drop of resistance at around 4.2 K. The experiment was done more times, and finally, they accepted the experimental evidence that the resistance was dropping from 0.1Ω to less than $3 \cdot 10^{-6} \Omega$. Mercury was the first metal to be discovered as a “superconductor”, and 4.2 K is said to be its critical temperature (T_c). Since this discovery, many other pure elements were found to be superconducting below their critical temperatures. The most common ones would be niobium, Nb, with a T_c of 9.3 K, titanium, Ti, with T_c of 2.4 K, and tin, Sn, whose T_c is 3.7 K [23].

However, it was only around 1950 that some alloys were found to have higher critical temperatures than their base elements. It is the case of the well-known NbTi, with T_c of 9.8 K, and Nb₃Sn, whose T_c is 18.1 K. These discoveries were within theoretical predictions based on the physical models available at that time, that were identifying an upper bound of 30 K for the critical temperatures. This threshold was passed in 1988, when a new superconducting material was found with a T_c of 90 K. This represented the holy grail for scientists since, the critical temperature was above the boiling point of nitrogen, and therefore several technological simplifications could be made.

From a phenomenological perspective, the most remarkable advance in superconductivity, after its discovery, was in 1933 when Walter Meissner and Robert Ochsenfeld discovered that superconductors are not only perfect conductors but also perfect diamagnetics. This implies that below a certain field strength called “critical field strength”, B_c , the materials in a superconducting state would expel the magnetic field from their interior. Later it would be found that there is a characteristic length, λ , also known as “penetration depth”, that is associated with the decay of the magnetic field from the surface of the material to the core [23]. A second remarkable discovery was merely theoretical and was done by Alexei Abrikosov in 1957. He predicted that the existence of another type of superconductors, for which the critical field strength was not only a single value, but there would be a lower and an upper bound, B_{c1} and B_{c2} , between which some materials would be in a “mixed state”. In such a case there would be regions characterized by the superconducting state and others where the material would act as a normal conductor. Materials that follow these laws are referred to as “Type II” superconductors, whereas materials with only one critical field strength are “Type I” superconductors.

No matter what the type of superconductor, it was found that there is a dependency of the critical magnetic field strengths (whether only B_c or B_{c1} and B_{c2}) with the temperature. Starting from a theoretically known $B_c(0)$ at 0 K, the law is approximately parabolic [23], as

$$B_c(T) \cong B_c(0) \left[1 - \left(\frac{T}{T_c} \right)^2 \right] \quad (4.3)$$

Moreover, another parameter is involved in determining the state of a superconductor, that is the current density J . The explanation resides in the fact that a superconductor is also perfectly diamagnetic. Since the field B is null inside the core of a superconductor, by applying Ampere’s law it derives that also the current needs to be zero. Therefore, in a superconducting material current should theoretically run on the surface of the conductor. In reality, we know that there is a thin layer, associated with λ , in which the current runs. In this thin layer, the motion of electrons generates a magnetic field that sums to the one applied from the extern. Therefore, depending on the current density, and on the shape of the conductor, the local magnetic field can exceed the critical values.

Given these considerations, the state of a superconductor is determined at least by three parameters: temperature T , Magnetic field strength B , and current density J . And the “limit” state can be represented as a surface in 3D, called critical surface. [24] Temperature and field dependence of J_c can be modeled with semi-empirical formulae, for example Bottura’s formula for NbTi [25]:

$$\frac{J_c(B, T)}{J_{c,ref}} = \frac{C_{NbTi}}{B} \left[\frac{B}{B_{C2}(T)} \right]^{\alpha_{NbTi}} \left[1 - \frac{B}{B_{C2}(T)} \right]^{\beta_{NbTi}} \left[1 - \left(\frac{T}{T_{C0}} \right)^{1.7} \right]^{\gamma_{NbTi}} \quad (4.4)$$

Where $J_{c,ref}$ is the critical current density at 4.2 K and 5 T (e.g. ~ 3000 A/mm²) and C_{NbTi} (~ 30 T), α_{NbTi} (~ 0.6), β_{NbTi} (~ 1.0), γ_{NbTi} (~ 2.3) are fitting parameters [24]. A representation of the critical surface for a common alloy of NbTi is presented in Fig. 4.2.

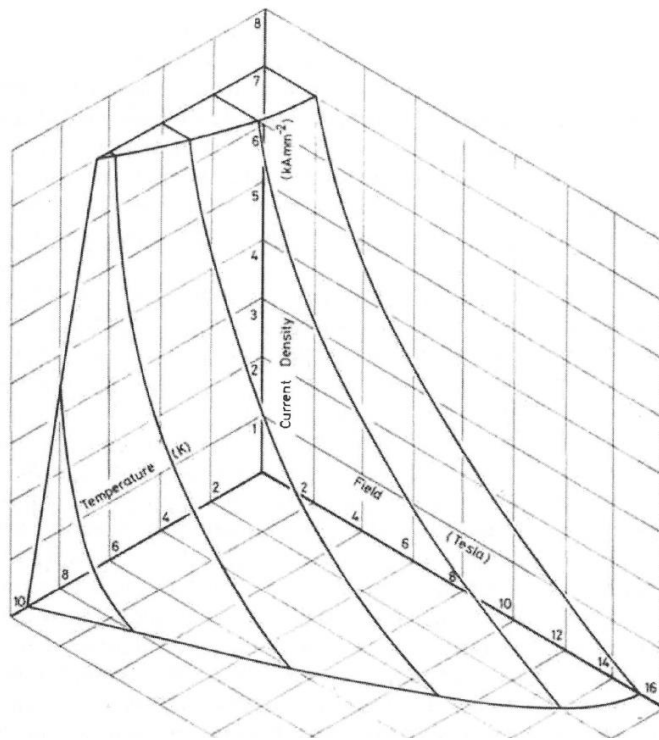


Fig. 4.2 – Representation of the critical current density (J_c [A/mm]) surface over temperature (T [K]) and magnetic field intensity (B [T]) of NbTi [26].

4.2 Superconductors type I and II

These types of superconductors differ substantially in their reaction to external magnetic fields of a certain amplitude. Let us consider first the type I.

When an external magnetic field is applied in such a way that its field lines are slightly perturbed from the present of a perfect diamagnet, i.e. the conductor in SC state, type I superconductors show only a single critical magnetic field, below which the whole conductor remains diamagnetic. However, when the field is oriented in an unfavorable way, field lines are highly perturbed, and locally the field strength can reach high values. In very unfavorable configurations, even fractions of the critical field B_c can quench superconductivity locally. Materials in this case present a coexistence of superconducting regions and normal conducting ones, the so-called “intermediate state”. Slightly diamagnetic materials can be placed on the surface of specimens such as those in Fig. 4.3b, to visualize regions where the field intensity is lower, i.e. the surfaces of the superconducting regions.

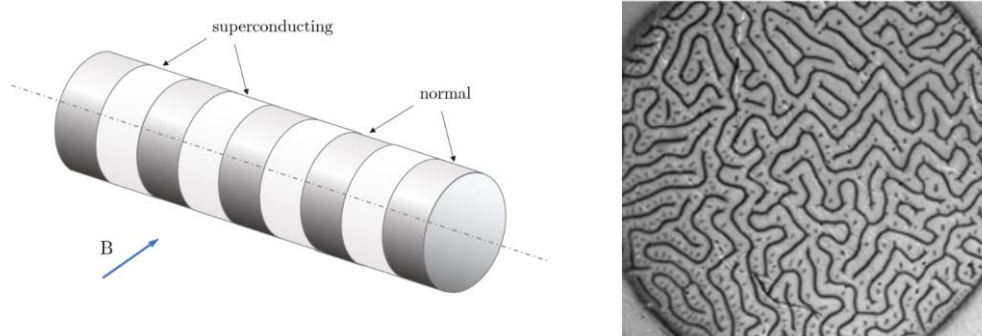


Fig. 4.3 – Visual representation of the intermediate state for type I superconductors [27].

Almost all the pure elemental superconductors are type I, with few exceptions like niobium. Most used materials are instead type II superconductors, which are generally superconducting alloys.

The concepts just described about the unfavorable field configuration apply also to type II superconductors. However, the most peculiar characteristic arises even in a normal field configuration. As mentioned earlier these materials have two critical field strengths. But above the lower bound the transition to the normal state is not sudden. Small regions appear in the conductor, namely the “normal cores”, characterized by normal conducting state. The superconductor is then said to be in the “mixed state”, or “Abrikosov state” from the name of the scientist that predicted it.

These regions arrange themselves in ordinate lattice structures along the conductor and their density increases as the field increases from B_{c1} to B_{c2} . Each core is surrounded by a vortex or circulating current, and it is crossed by a precise field flux, that is the quantum of magnetic flux, given by:

$$\phi_0 = \frac{h}{2e} = 2.07 \cdot 10^{-15} \text{ T m}^2 \quad (4.5)$$

In which h is Planck’s constant and e is the charge of the electron [23].

The graphical representation of the mixed state is presented in Fig. 4.4a and beside it in Fig. 4.4b we find a micrograph of a material in mixed state with ferromagnetic particles deposited on the surface, highlighting therefore the normal cores.

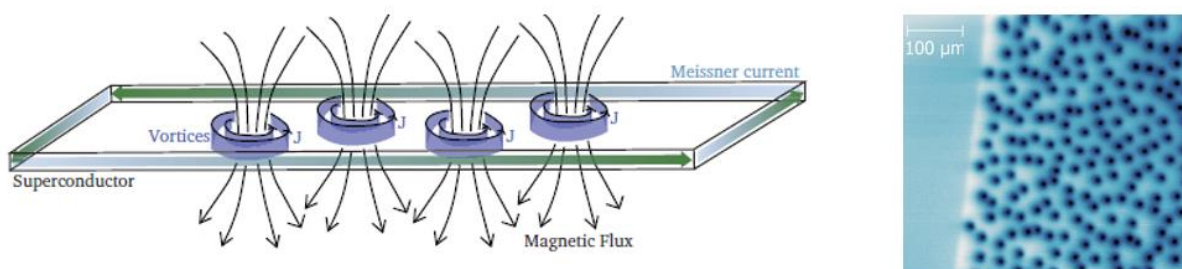


Fig. 4.4 – Visual representation of type II superconductors in mixed state [28] and images of vortices in 200 nm thick YBCO film by Scanning SQUID Microscopy [29].

The reason why this type of superconductor is the only one used for accelerator magnets is that only these materials can withstand a magnetic field, thanks to the penetration in quantized fluxoids. Another advantage would be the high values of B_{c2} , if compared to the B_c of type I ones. This is the case of NbTi and Nb₃Sn, whose upper critical fields are in the order of 10 T, making them suitable for high energy physics, fusion, and many other applications.

4.3 Superconductors for the GaToroid magnets

In this paragraph we will introduce the typical superconductors used for magnets and then discuss the available options for the toroid.

4.3.1 Practical superconductors for accelerator magnets

We shall at this point make a distinction between Low Temperature Superconductors (LTS) and High Temperature Superconductors (HTS), whose naming scheme leads already to a first distinction. Despite this qualitative intuition, there is a fundamental difference of physical nature lying under this distinction. The behavior of LTS material has been thoroughly explained by the Bardeen-Cooper-Schrieffer (BCS) theory, in 1957. This theory explains that at low temperatures the electrons of some materials (superconductors) find it energetically more favorable to group in pairs (quasi-particles). Thus, the zero resistance occurs because the scattering does not excite the quasi-particle [30]. On the other hand, the behavior of HTS materials has not been theorized yet, and the physical mechanism at the atomic scale remains still unknown. In terms of critical temperatures there is no clear threshold that could be mentioned. However, even if the boundary is not well defined, the typical superconductors for magnet applications can be targeted with no doubt to the one category or the other. Traditional materials like Nb₃Sn and NbTi are Low Temperature Superconductors, with T_c respectively of 18 K and 10 K. High Temperature Superconductors are instead the most recently discovered (1986/1988) ones, e.g. the cuprate BSSCO and the ceramic YBCO, namely Bismuth Strontium Calcium Copper Oxide, and Yttrium Barium Copper Oxide.

4.3.2 ReBCO Superconductors

Among the high temperature superconductors, great interest has arisen around Rare-Earth-Barium-Copper-Oxide (REBCO) coated superconductors. These materials (such as Yttrium-Based-Copper-Oxide, YBCO) are finding more and more industrial applications in [31] fusion energy and devices with unparallel magnetic fields and operating current densities, such as high-resolution Nuclear Magnetic Resonance (NMR) spectrometers. [32] For these materials, cooling with liquid helium is no longer needed, and very high current densities (above 10 kA/mm²) can be achieved.

A few fundamental properties for technical applications must be mentioned about these superconductors [32]. First, ReBCO are ceramic compounds, brittle at the point that are manufactured in 1 – 5 μ m thick layers to allow for some flexibility. Secondly, for [32] high performances the ReBCO must come in a single-crystal form, with only a small spread of grain orientations. For this purpose, a buffer layer can be used deposited with sputtering

techniques on top of a stainless steel substrate. This latter is also aimed to provide structural resistance to the tape, withstanding loads that may develop during operation. Finally, the stack of layers is enclosed by two copper strips that act as stabilizers in case of quench. A schematization of the ReBCO tapes composition is presented in Fig. 4.5.

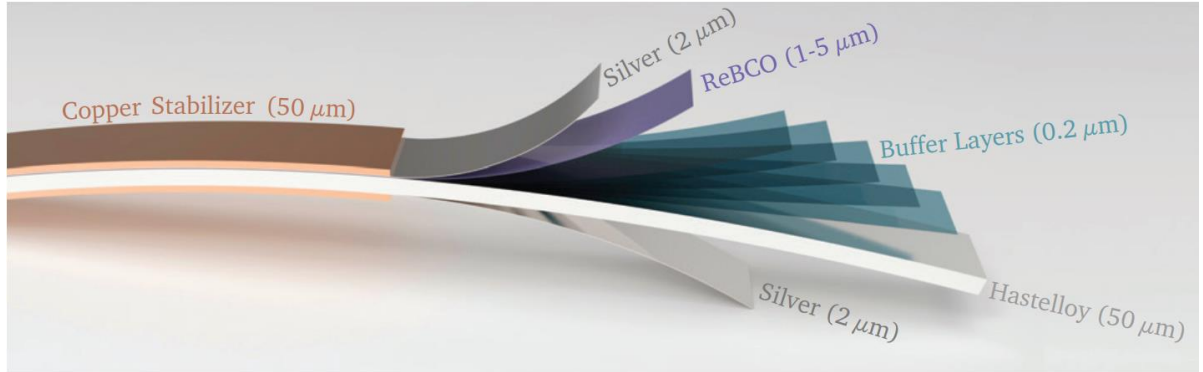


Fig. 4.5 – Schematization of the architecture of ReBCO tapes [28].

4.3.3 Superconductors for the proton gantry

In the GaToroid project context, the requirements for protons in terms of magnetic field are such that a maximum peak of 6.8 T is foreseen on the conductors. The modest entity of the latter leaves the doors open for the choice between LTS and HTS. To limit the heat losses and complexity of the system also the current density has been brought down to modest values, and therefore the choice of the superconductor could be between 0.5mm strands of Ni-Ti Rutherford cable, or a Non-Twisted stack of three ReBCO tapes, represented both in Fig. 4.6. Table 4.1 lists the characteristic parameters resulting from the two options.

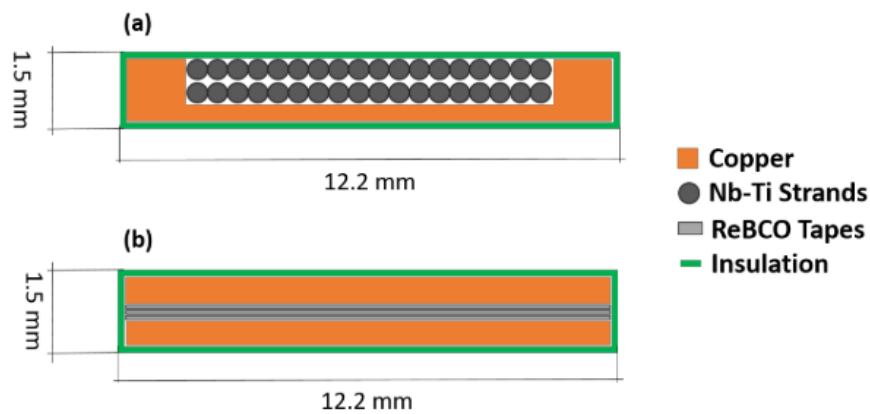


Fig. 4.6 – Schematization of the NbTi Rutherford cable (top) and the ReBCO cable (bottom) for the proton gantry.

Table 4.1 – Characteristics of the LTS and HTS options for the proton gantry.

Parameter	LTS	HTS
Superconductor	NbTi	ReBCO
Cable topology	Rutherford	Non-Twisted Stack
Number of strands / tapes	36	4
Cable width [mm]	12.2	12.2
Cable height [mm]	1.5	1.5
Cu to Sc ratio (conductor)	3	7.3
Length [km]	2.5	2.5
Operating Current [kA]	1.8	1.8
Operating Temperature [K]	4.5	20
Engineering Current Density [A/mm^2]	100	100

4.3.4 Superconductors for the C-ion Gantry

For this gantry the reference conductor will be a $12.1 \text{ mm} \times 1.7 \text{ mm}$ Rutherford cable consisting of 22 strands of NbTi superconducting wires, embedded into a nominal rectangular Oxygen-Free-High-Thermal-Conductivity (OFHC) Copper stabilizer of $6.4 \text{ mm} \times 16 \text{ mm}$. The cable is schematized in Fig. 4.7. Copper only serves as stabilizer and could be changed to Aluminum if willing to reduce the size.

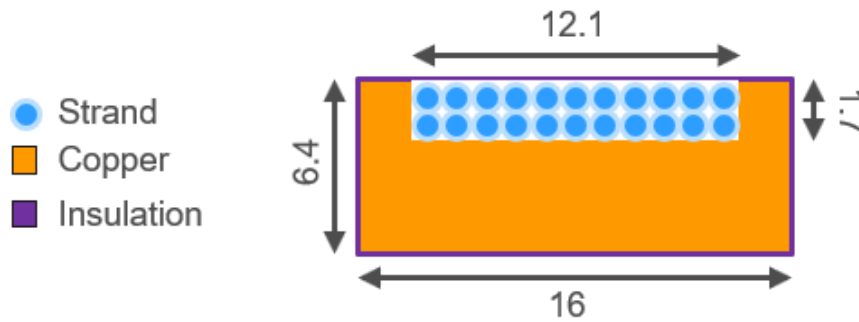


Fig. 4.7 – Schematization of the LTS NbTi cable for the C-ion gantry.

Table 4.2 – Characteristic parameters of the NbTi cable for the C-Ion gantry.

Parameter	Detail
Superconductor	NbTi
Conductor material	Cu-(NbTi) in rectangular Cu profile
Number of strands in the cable	22
Number of filaments in each strand	54
Strand diameter [mm]	1.00
Filament diameter [μm]	45
Cu to Sc ratio (strand)	1.35
Twist pitch [mm]	15
Cable width [mm]	12.1
Cable height [mm]	1.7
Profile width (mm)	16.0
Profile height [mm]	6.4
Cu to Sc ratio (conductor)	12.5
Length large/small [km]	105.2 / 46.4
Critical current @ 4.2K and 6T [A]	16 016
Engineering current density [A/mm ²]	68

5. Finite Element Analyses

In this chapter the Finite Element Method (FEM) is introduced. This numerical technique born around the 1950s' is largely adopted nowadays to solve a great number of engineering tasks, spanning a wide range of physical phenomena. This method allows the calculation of approximate solutions to physical problems inside complex domains, whose governing differential equations often do not offer a closed form solution. In the context of the GaToroid project, this method has been used to compute the mechanical response of the demonstrator magnet to assembling, cryogenic and powering loads, as well as its electromagnetic behavior. At first, an introduction to the general concepts of FEM is offered. Then the fundamental equations underlying structural and electromagnetic problems are presented. And finally, the mechanical and magnetostatic model of the demonstrator magnet are described.

5.1 The general framework

Many continuum problems that arise in physics and engineering are described by a set of differential equations and a set of boundary conditions that the unknown solution functions need to satisfy [33]. In general terms the solution is an unknown function \mathbf{u} (scalar or vector of several variables) that satisfies a set of equations \mathbf{F} , inside a domain Ω , of the kind:

$$\mathbf{F}(\mathbf{u}) = \begin{Bmatrix} \mathbf{F}_1(\mathbf{u}) \\ \mathbf{F}_2(\mathbf{u}) \\ \vdots \end{Bmatrix} = 0 \quad (5.1)$$

together with boundary conditions \mathbf{B} on the boundaries $\partial\Omega$:

$$\mathbf{B}(\mathbf{u}) = \begin{Bmatrix} \mathbf{B}_1(\mathbf{u}) \\ \mathbf{B}_2(\mathbf{u}) \\ \vdots \end{Bmatrix} = 0 \quad (5.2)$$

For such problems, finite element procedures identify a standard discrete system [33] in which:

- the continuous domain is subdivided into a finite number of elements, the behavior of which can be understood by a finite number of parameters.
- a finite set of variables, \mathbf{a}^e , becomes the unknown of the problem, to be determined uniquely at the boundaries of the elements (that can be nodes, edges, or surfaces).
- the solution of the global system is achieved with the same procedure that would apply to standard discrete problems.
- the extension of the global solution inside the elements' boundaries, \mathbf{u} , is done by a set of functions, the so-called "shape functions", \mathbf{N} .

As an example, the solution \mathbf{u} inside a finite element defined by the general boundaries a , b , c can be approximated by:

$$\mathbf{u} \cong \mathbf{u} = \sum_{i=a,b,c} \mathbf{N}_i \mathbf{a}_i^e = [\mathbf{N}_a, \mathbf{N}_b, \mathbf{N}_c] \begin{Bmatrix} \mathbf{a}_a \\ \mathbf{a}_b \\ \mathbf{a}_c \end{Bmatrix}^e = \mathbf{N} \mathbf{a}^e \quad (5.3)$$

These shape function \mathbf{N} need to ensure the continuity of the solution between adjacent elements. However, depending on the choice of these, local violation of the equilibrium conditions may occur inside the element and on its boundaries [33]. And finally, their choice may also affect the degree of approximation.

In any case, shape functions are the key entity that allows to discretize a continuum problem, and therefore are at the basis of all FE procedures. They allow to pass from the differential form of the equations describing a physical problem, to their integral one, and the solution of the global system can be sought as the sum of the solutions inside all the subdomains:

$$\int_V f \, dV = \sum_e \int_{V^e} f \, dV \quad (5.4)$$

Generally, such an integral form of the governing equations can be achieved by choosing an appropriate functional representative of the energy of the system. In the case of elasticity problems, this is the sum of the virtual work of the external loads and the virtual work of the internal forces. No matter the physical nature of the problem though, it has been recognized [34] that the finite element approach is equivalent to the direct minimization of the total potential energy of the system. The well-known Rayleigh-Ritz procedure.

In case the shape functions are chosen correctly, the finer discretization of the domain ensures convergence towards the correct, but unknown, solution. In the case of structural mechanics, the criteria to ensure that the shape functions are chosen correctly are the following [35]:

- i. “The displacement function chosen should be such that it does not permit straining of an element to occur when the nodal displacements are caused by a rigid body displacement.
- ii. The displacement function has to be of such a form that if nodal displacements are compatible with a constant strain⁴ condition such constant strain will in fact be obtained.
- iii. The displacement functions should be so chosen that the strains at the interface between elements are finite (even though indeterminate).”

⁴ Notice that “strain” in this context assumes a broader concept than the mere first derivative of displacements. The definition depends on the problem analyzed. As an example, in the FE theory of plates and shells strains may be referred to both the first and to the second derivative of the displacements.

Nowadays, shape functions of a large family of elements are well established, and they can be found relatively easily implemented in several finite element codes (ANSYS, ABAQUS, NASTRAN, etc.).

To give an example we shall consider a rectangular element of dimensions $2a$ and $2b$ in a 2D cartesian domain, whose centroid is at the coordinates x_c and y_c , as shown in Fig. 5.1 [36].

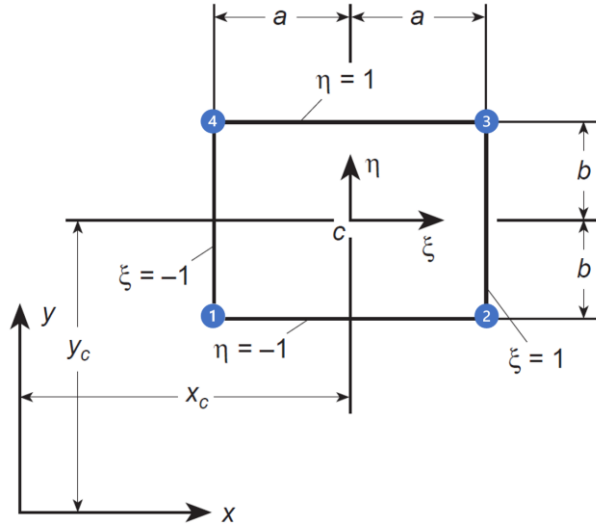


Fig. 5.1 – A first order rectangular element connecting nodes numbered from 1 to 4.

It is convenient to use normalized coordinates ξ and η , so that their values are ± 1 at the element boundaries.

$$\begin{aligned}\xi &= \frac{x - x_c}{a} \\ \eta &= \frac{y - y_c}{b}\end{aligned}\tag{5.5}$$

Shape function must be at least of C^0 continuity, and the simplest choice falls on polynomial type functions in most of the cases. The degree of the polynomial employed depends on the number of conditions that can be applied to uniquely define the shape function inside the element domain. This number coincides with the number of nodes, therefore in the case of the quadrilateral element of Fig. 5.1, its shape functions can be uniquely defined by four coefficients. Therefore, the trend of the variable \hat{u} (or degree of freedom, DOF) inside the element can be described by a polynomial like the following:

$$u = \alpha_1 + \alpha_2 \xi + \alpha_3 \eta + \alpha_4 \xi\eta\tag{5.6}$$

The coefficients α_i are then obtained by solving the following system of equations:

$$\begin{Bmatrix} a_1 \\ \vdots \\ a_4 \end{Bmatrix} = \begin{bmatrix} 1 & -1 & -1 & 1 \\ \dots & \dots & \ddots & \vdots \\ 1 & -1 & 1 & -1 \end{bmatrix} \begin{Bmatrix} \alpha_1 \\ \vdots \\ \alpha_4 \end{Bmatrix}\tag{5.7}$$

And then the final approximation of the variable \hat{u} can be rewritten to highlight the shape function matrix \mathbf{N} as:

$$\mathbf{u} = \mathbf{N}(\xi, \eta) \begin{Bmatrix} a_1 \\ \vdots \\ a_4 \end{Bmatrix} \quad (5.8)$$

For more complex elements, an easier and more systematic ways of defining the coefficients have been developed. The most common one employs Lagrange polynomials [36] for the singular coordinates $l(\xi)$ and $r(\eta)$, thus obtaining the coefficients N_{ij} of the shape function matrix as:

$$N_{ij}(\xi, \eta) = l(\xi) \cdot r(\eta) \quad (5.9)$$

As mentioned earlier, shape functions play a fundamental role in allowing the definition of an integral form for the physical problems being investigated. These integrals are solved inside the element's domain thanks to techniques of numerical of integration, the most common of which is the one of Gauss. Once these are defined, the solution of the integrals inside the elements' domain allow to define its characteristics and behavior. These are finally described in a matrix \mathbf{K} , that in case of structural mechanics takes the name of “Stiffness matrix”. By assembling the stiffness matrixes of all the elements, the systems' stiffness matrix is achieved, and the physical problem is generally described by a set of algebraic equations of the form:

$$\mathbf{f} = \begin{Bmatrix} f_1 \\ \vdots \\ f_n \end{Bmatrix} = \begin{bmatrix} K_{11} & \cdots & K_{1n} \\ \cdots & \ddots & \vdots \\ K_{n1} & \cdots & K_{nn} \end{bmatrix} \begin{Bmatrix} a_1 \\ \vdots \\ a_4 \end{Bmatrix} = \mathbf{K} \mathbf{a} \quad (5.10)$$

being \mathbf{f} the vector of external loads, and n the total number of degrees of freedom.

The modern computing resources are able to rapidly solve problems proposed in a matrix form, especially if processed with partitioning and Gauss elimination methods. Therefore, this method makes it particularly suitable to be implemented in software codes to solve different physical problems.

It is worth mentioning that elements like the one in Fig. 5.1 are usually referred to as “first order” elements, since their shape functions are at most linear in the coordinates ξ, η . Elements of the serendipity family instead, are able to involve higher polynomial degrees of two or higher by introducing a set of “midside” nodes and are therefore usually referred to as “second” order (or higher) elements. These elements not only allow to better approximate the solution inside the element's domain, but are also able to replicate geometries better, since the edges passing through their nodes are defined by a two-degree polynomial. For these reasons, this element technology has nowadays become the standard for several problems.

5.2 Mechanics

[35] For structural mechanics problems the solution implies knowledge of the displacement field, the stress and the strain ones, inside the elastic continuum. In finite element procedures the solution is sought in the form of displacements \mathbf{u} at the nodes. By applying the congruence equations, strains can be calculated from eq. 5.3 involving a linear operator \mathbf{L} such that:

$$\boldsymbol{\varepsilon} = \mathbf{L} \mathbf{u} = \mathbf{L} \mathbf{N} \mathbf{a} = \mathbf{B} \mathbf{a} \quad (5.11)$$

Being $\mathbf{B} = \mathbf{L} \mathbf{N}$. In the simple case of a 2D geometry, given the displacements u and v , in plane stress conditions, this is:

$$\boldsymbol{\varepsilon} = \begin{Bmatrix} \varepsilon_x \\ \varepsilon_y \\ \gamma_{xy} \end{Bmatrix} = \begin{Bmatrix} \frac{du}{dx} \\ \frac{dv}{dy} \\ \frac{du}{dy} + \frac{dv}{dx} \end{Bmatrix} = \begin{bmatrix} \frac{d}{dx} & 0 \\ 0 & \frac{d}{dy} \\ \frac{d}{dy} & \frac{d}{dx} \end{bmatrix} \begin{Bmatrix} u \\ v \end{Bmatrix} \quad (5.12)$$

Materials' properties are included in the transition from strains to stresses. An appropriate elasticity matrix \mathbf{D} can be assembled, such that:

$$\boldsymbol{\sigma} = \mathbf{D} (\boldsymbol{\varepsilon} - \boldsymbol{\varepsilon}_0) + \boldsymbol{\sigma}_0 \quad (5.13)$$

accounting for initial strains, that could be due for example to thermal expansion ($\boldsymbol{\varepsilon}_0 = \alpha \Delta T$), and residual stresses $\boldsymbol{\sigma}_0$, that for example could be due previous manufacturing operations.

With this formulation, the element's characteristics from a global point of view can be resumed in an elementary stiffness matrix \mathbf{k}^e , that can be derived from energy principles in the form of:

$$\mathbf{k}^e = \int_{V^e} \mathbf{B}^T \mathbf{D} \mathbf{B} dV \quad (5.14)$$

At this stage, by equating the virtual work of external loads to the one of internal ones we reach the general form of finite element problems in structural mechanics:

$$\mathbf{q}^e = \mathbf{k}^e \mathbf{a}^e + \mathbf{f}^e \quad (5.15)$$

being \mathbf{f}^e the vector of internal loads

$$\mathbf{f}^e = \int_{V^e} \mathbf{B}^T \boldsymbol{\sigma}_0 dV - \int_{V^e} \mathbf{B}^T \mathbf{D} \boldsymbol{\varepsilon}_0 dV - \int_{V^e} \mathbf{N}^T \mathbf{b} dV \quad (5.16)$$

and \mathbf{b} the vector of the distributed loads interesting the volume V^e . Such distributed loads are in most cases due to gravity or accelerations, but in the case of electromagnetic systems this contribution accounts also for Lorentz forces.

Integrals in equations 5.14 and 5.16 are solved with the numerical integration techniques mentioned earlier, and the so-computed matrixes and vectors are assembled in the global equation system in the form of eq. 5.10.

5.3 Electromagnetics

The laws governing electromagnetic fields are described in Maxwell's equations. Of these, Ampere's law (eq. 5. 17), and the magnetic induction continuity law (eq. 5.18) describe the properties of a magnetic field.

$$\nabla \times \mathbf{H} = \mathbf{J} + \frac{\partial \mathbf{D}}{\partial t} \quad (5.17)$$

$$\nabla \cdot \mathbf{B} = 0 \quad (5.18)$$

Where \mathbf{H} is the magnetic field, \mathbf{J} is the current density, \mathbf{D} is the electric flux density and \mathbf{B} is the magnetic induction (or magnetic flux density). Current density is by far the dominant source of \mathbf{H} field in the case of superconducting magnets [37]. Thus, the \mathbf{D} contribution can be neglected for simplicity.

In finite element procedures, Ampere's equation can be re-written in a more suitable way. Introducing the magnetic vector potential (m.v.p.) \mathbf{A} , related to the magnetic flux density \mathbf{B} by the equation:

$$\nabla \times \mathbf{A} = \mathbf{B} \quad (5.19)$$

and changing from distributed to lumped parameters, Ampère-Maxwell's law can be re-written in matrix form as [38]:

$$\nabla \times ([\boldsymbol{\nu}] \nabla \times \mathbf{A}) = \mathbf{J} \quad (5.20)$$

where \mathbf{J} becomes the only excitation, and $[\boldsymbol{\nu}]$ is the reluctivity diagonal matrix, containing the directional reluctivities (inverse of permeability μ) in case of anisotropic media.

Therefore, given a spatial distribution of current densities J_x, J_y, J_z , and an appropriate set of Neumann and Dirichlet boundary conditions, the solution of the finite element problem involves the knowledge of the three components of the m.v.p., A_x, A_y, A_z , from which the magnetic flux density is retrieved as:

$$B_x = \frac{\partial A_z}{\partial y} - \frac{\partial A_y}{\partial z} = A_{zy} - A_{yz} \quad (5.21)$$

$$B_y = \frac{\partial A_x}{\partial z} - \frac{\partial A_z}{\partial x} = A_{xz} - A_{zx} \quad (5.22)$$

$$B_z = \frac{\partial A_y}{\partial x} - \frac{\partial A_x}{\partial y} = A_{yx} - A_{xy} \quad (5.23)$$

A suitable energy functional \mathbf{F} , that allows to write this differential problem into its integral form (of the kind of eq. 5.4) has been proposed by Demerdash [38], where:

$$\mathbf{F}(\mathbf{A}) = \int_V \mathbf{f} \, dV = \iiint_V \frac{1}{2} (\mathbf{B} \cdot \mathbf{H}) - \mathbf{J} \cdot \mathbf{A} \, dx \, dy \, dz \quad (5.24)$$

By applying variational approaches, the stationarity points of this functional can be sought ($\delta \mathbf{F}(\mathbf{A})/\delta \mathbf{A} = 0$), which is equivalent to solving the partial differential equations governing the field problem, satisfying at the same time the Neumann and Dirichlet type boundary conditions [38]. The equations to be solved by numerical integration are therefore the following:

$$\frac{\partial \mathbf{F}(\mathbf{A})}{\partial A_x} = \iiint_V \left[\frac{\partial}{\partial A_x} \left(\frac{1}{2} \nu_x B_x^2 + \frac{1}{2} \nu_y B_y^2 + \frac{1}{2} \nu_z B_z^2 \right) - \frac{\partial}{\partial A_x} J_x A_x \right] dx dy dz \quad (5.25)$$

$$\frac{\partial \mathbf{F}(\mathbf{A})}{\partial A_y} = \iiint_V \left[\frac{\partial}{\partial A_y} \left(\frac{1}{2} \nu_x B_x^2 + \frac{1}{2} \nu_y B_y^2 + \frac{1}{2} \nu_z B_z^2 \right) - \frac{\partial}{\partial A_y} J_y A_y \right] dx dy dz \quad (5.26)$$

$$\frac{\partial \mathbf{F}(\mathbf{A})}{\partial A_z} = \iiint_V \left[\frac{\partial}{\partial A_z} \left(\frac{1}{2} \nu_x B_x^2 + \frac{1}{2} \nu_y B_y^2 + \frac{1}{2} \nu_z B_z^2 \right) - \frac{\partial}{\partial A_z} J_z A_z \right] dx dy dz \quad (5.27)$$

5.4 Modeling techniques

The modeling procedures of mechanical and electromagnetic problems are significantly different, even though the base geometry is the same (the demonstrator magnet). While elastic bodies can be discretized independently, and then mutually connected with adequate element types (contact, bolt, etc.), in the case of magnetostatic problems the whole domain of interest must be discretized coherently. This means that elements of different components must share the same boundaries (nodes), to ensure the continuity of the field. Here below the models are presented, differentiating upon the analysis type.

The finite element model of the coil for structural analyses is presented in Fig. 5.2. The windings are meshed with first order brick (8-nodes hexahedral) elements, which offer much better performances than the first order tetrahedrons. The reference element in the ANSYS library is SOLID185.

Bolts are modeled as beam elements, BEAM188, and their pretension load is applied with PRETS179 elements. This combination allows to greatly simplify the model and requires significantly fewer computing resources. The bolts head and thread are connected respectively to the cover plates and intermediate plate by rigid joint elements, MPC184, that allow to couple the DOFs of different elements. Finally, the contact interfaces between different components are covered of CONTA174 and TARGE170 elements, the behavior of which will be described in chapter 6.

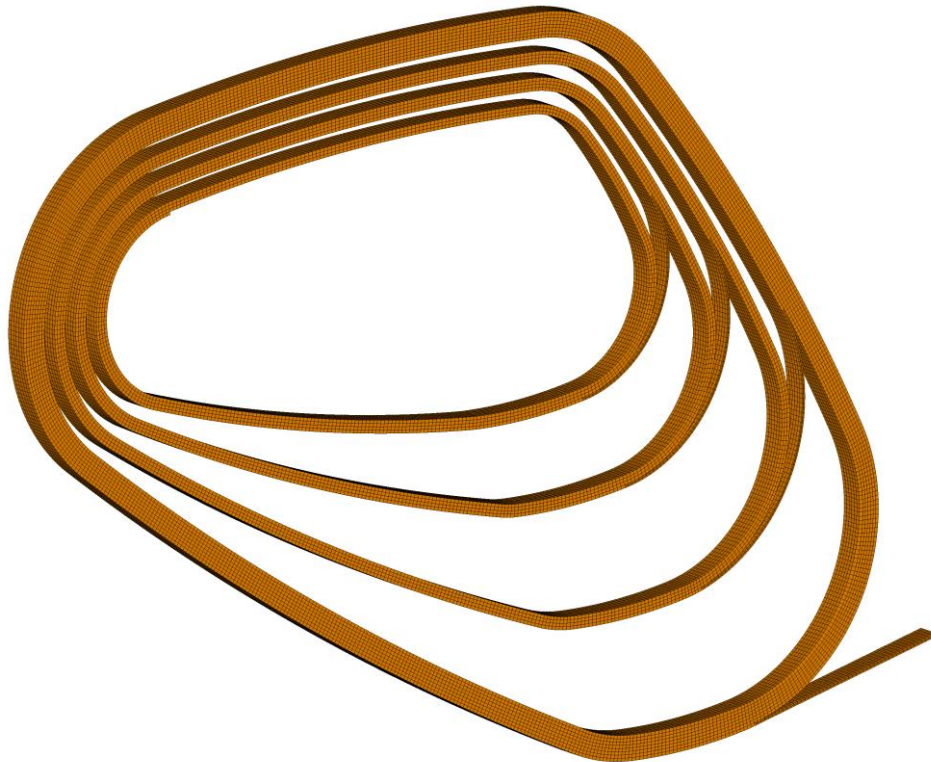


Fig. 5.2 – Finite Element model of one side of the windings.

As mentioned earlier, the whole domain of interest must be modeled properly for a magnetostatic analysis. This includes therefore both the windings and the surrounding air region.

Prior to any magnetic calculations however, the current density distribution inside the conductors must be known. It is necessary therefore that an accurate preliminary electric analysis is done to find \mathbf{J} at all nodes. The first element type employed is therefore the 3D coupled field SOLID5 element, with the appropriate option to make voltage (VOLT) being the DOF at its nodes.

Once the current density distribution inside the coil is known, the elements can be turned to the 3D electromagnetic SOLID97 type. Now the calculated \mathbf{J} 's act as external loads, and the field can be computed inside the domain discretized. To grasp the behavior at infinite distance, elements with a peculiar integro-differential formulation, INFIN111, must surround the air region, and their length must be of the same order of the whole domain of interest, as shown in Fig. 5.3.



Fig. 5.3 – Schematic of the finite element model for electromagnetic calculations.

6. Demonstrator mechanics

In this chapter the detailed design process of the demonstrator magnet is presented. Starting from the ideal coil, the mechanical structure is built around it to meet various requirements. Structural components are added, and the stress state inside the magnet is assessed. Based on the results of the analyses and developments with prototyping at the magnet technology workshop at CERN, further geometrical changes are suggested, and again the response of the magnet is evaluated with FEM analyses.

6.1 Geometry

Chapter three introduced the concepts and the scope behind the building of the demonstrator. We shall now recall some concepts and eventually elaborate them to understand the simulations' principles and outcomes better.

The demonstrator's heart resides in the coils, composed of two pancake layers (double pancake), each of them composed of four grades. Two superconductors have been considered for this application: NbTi as LTS option and ReBCO tapes as HTS one. Only the latter is considered in this thesis, since it is the option chosen for the fabrication of the demonstrator.

As the ideal field for the GaToroid would be homogenous along the torus radius R , the purpose of the grades is to homogenize the field intensity, that would otherwise see the typical dependency of $1/R$, as shown in Fig. 3.2a. The three most internal grades have four cable turns, while the most outer one has eight of them; hence it is usually considered a double grade. Fig. 6.1 illustrates the optimized ideal geometry of the magnet, driven by only beam delivery requirements.

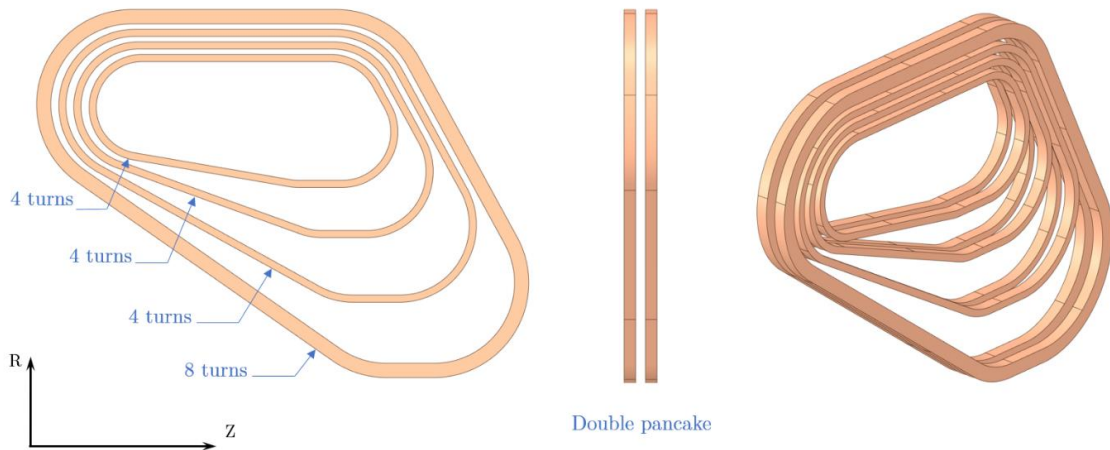


Fig. 6.1 – Baseline ideal coil configuration deriving from magnetic optimization.

An ideal magnet would be composed of grades only, a succession of circular arcs connected by straight lines. However, the coil's geometry needs to be adapted to a more realistic configuration, and several components must be added to satisfy different requirements.

First, other components are needed to guarantee sufficient structural strength and rigidity. We shall remember that even though the focus is now on the demonstrator, its geometry is derived from the full-size magnet for proton and c-ion gantries. To have a complete technological assessment, all the structural requirements of the full-size gantry must be fulfilled. The nature of the forces that develop during operation are magnetic and can be synthesized in formula 6.1.

$$\vec{F}_{\text{mag}} = \iiint_V \vec{f}_{\text{mag}} dv = \iiint_V \vec{J} \times \vec{B} dv \quad (6.1)$$

Where \vec{J} is the current density and \vec{B} the magnetic flux density. If considering the whole magnet and the electric circuit above, the integral becomes closed and the resulting magnetic force is zero⁵. However, this is not the case of the single grades. Both in the toroidal version and in the single demonstrator one the resulting force on each grade differs from zero. This is due to the mutual influence of different grades, and of different coils in the full gantry scheme. It is indeed the variation of the magnetic field intensity along the conductors' path that generates different elementary contributions \vec{f}_{mag} , leading to a non-zero integral force. These forces on each grade will be in general referred to as F_g , as schematized in Fig.6.2a.

In the case of an isolated single magnet, such as the case of the demonstrator, the vectorial sum of all forces F_g is zero. In a toroidal configuration instead, the resultant is directed along the torus' radius, towards the axis. This force tends to drive it towards the center; therefore, it is generally referred to as “centering force”, F_c .

In the unfortunate case of a quench occurring in one of the coils, e.g. the $(K+1)$ -th coil, another force F_ϕ may develop. This will be different from coil to coil but in principle tends to separate them from the one that quenched, and it is due to the imbalanced field, that differs from the ideal toroidal one. Fig. 6.2b schematizes the two forces F_c and F_ϕ on the K -th coil.

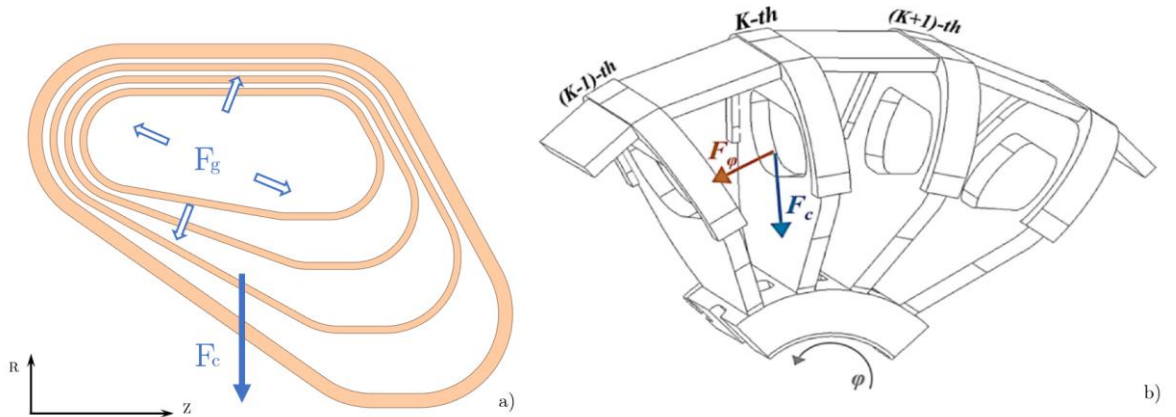


Fig. 6.2 - Schematic of the forces acting on the coils. Fig. a): forces acting on grades F_g , the sum of which gives birth to the centering force F_c . Fig. b): development of F_ϕ in the case of a single coil quenching ($(k + 1)$ -th coil).

⁵ This is always true in the ideal configuration of just the magnet surrounded by non-ferromagnetic material.

As said, F_ϕ develops only if the (K+1)-th coil quenches. F_c instead is always present. A buckling cylinder has been assigned to withstand these forces at the torus's inner radius. A rough dimensioning of it has been performed, employing the analytical solution for axis-symmetric solids under external pressure. Forces' values and bore's dimensions are listed in table 6.1.

Table 6.1 -List of operational forces acting on the C-ion gantry and preliminary dimensions of the buckling cylinder.

Parameter	Detail
Centering force F_c [MN]	1.43
Fault force F_ϕ [MN]	1.92
Cylinder thickness [m]	0.06
Cylinder length [m]	0.5
Cylinder hoop stress [MPa]	121
Inter-coil hoop stress [MPa]	63

Focusing now on the single coil, it has been decided to add metallic spacers to restrain grades and provide structural stiffness. Several configurations have been investigated by means of Finite Element calculations, and it was decided to support the coil with three spaces between each grade, an internal pole, an outer rim, and three plates to enclose the whole magnet. Fig. 6.3a offers a schematization of such components in the coil's plane, and 6.3b a section-view in the R- Φ plane.

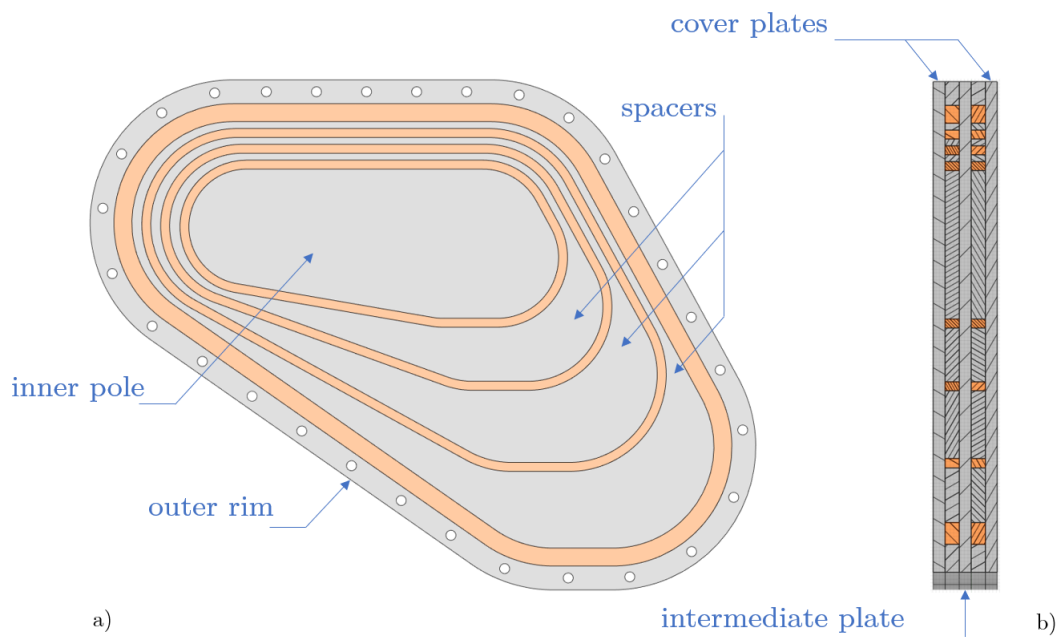


Fig. 6.3 – Structural components added to the ideal coil to guarantee structural rigidity.

The whole system will be held together by bolted joints, since it is a necessary practice to maintain structural stability and stiffness of the magnet, especially during the cool-down and powering phases. If an adequate contact pressure is ensured between components, these would be prevented from sliding one respect to the other. Therefore, a correct preload on bolts is a key factor for preventing slippage.

Several configurations of joints have been considered in the mechanical analyses since no immediate solution arose. In fact, the way the magnet is bolted together depends not only on the stability required but also on the assembly procedure. For this reason, the final configuration of screws has been decided only in the latest phases of the design process. In all preliminary simulations, the cover plate and the rim would have through holes, and only the intermediate plate's holes would have been threaded. An example of such a configuration is presented in Fig. 6.4.

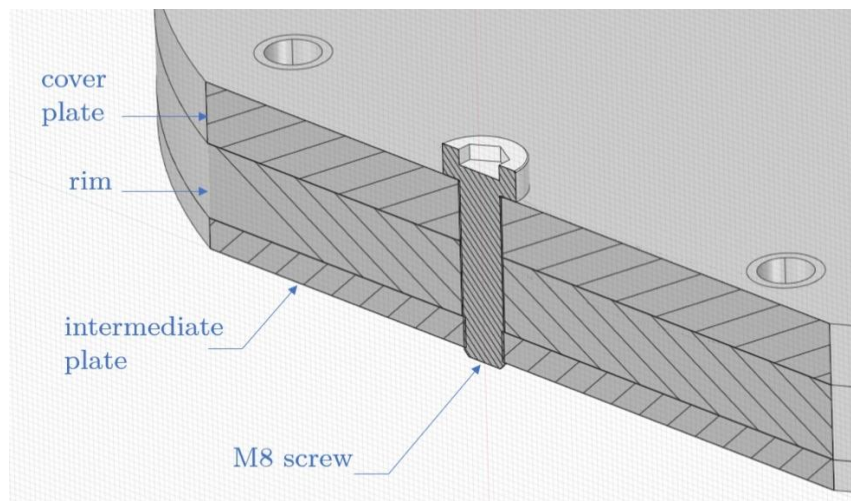


Fig. 6.4 – Section view of a bolted connection between a cover plate and the intermediate plate.

Bolts have been preliminary dimensioned according to ISO3505 standard, foreseeing a pretension load of 13.3 kN which tends to be slightly conservative for its scope. However, this can be revised in a second phase once the complete structural behavior of the magnet is simulated and understood.

Another important process to guarantee the stability of the components is the impregnation of the coils. In fact, small movements can cause frictional stresses that turn into heat. But when operating at cryogenic temperatures, even only 10 μm are sufficient to make the superconductor quench locally. Impregnating components with resin creates a stiff monolithic structure, giving an important contribution to prevent components from moving. For this reason it has become routine practice in magnets' manufacturing. For the GaToroid demonstrator, impregnation tests are being done on dummy stacks of copper tapes to replicate the HTS ReBCO superconductors. Fig. 6.5 shows the impregnation mould used to impregnate dummy cable stacks, as well as a batch of three cable stacks on the side. Different combinations of insulation and resin are being considered. The former between fiberglass and Kapton (Polyimide), and the later between different epoxies: MY750, CTD101K, and NHMFL 61.

The choice of one combination is driven by mechanical requirements, in terms of toughness and adhesion strength, and electric requirements, mainly insulation between different tapes. As an example, CTD101K shows the better adherence to the underlying components, however it presents cracks already after the first thermal cycles, as can be seen in Fig. 6.5 in the bottom-right picture. Therefore, no solution has clear advantages on the others, and tests are still ongoing.

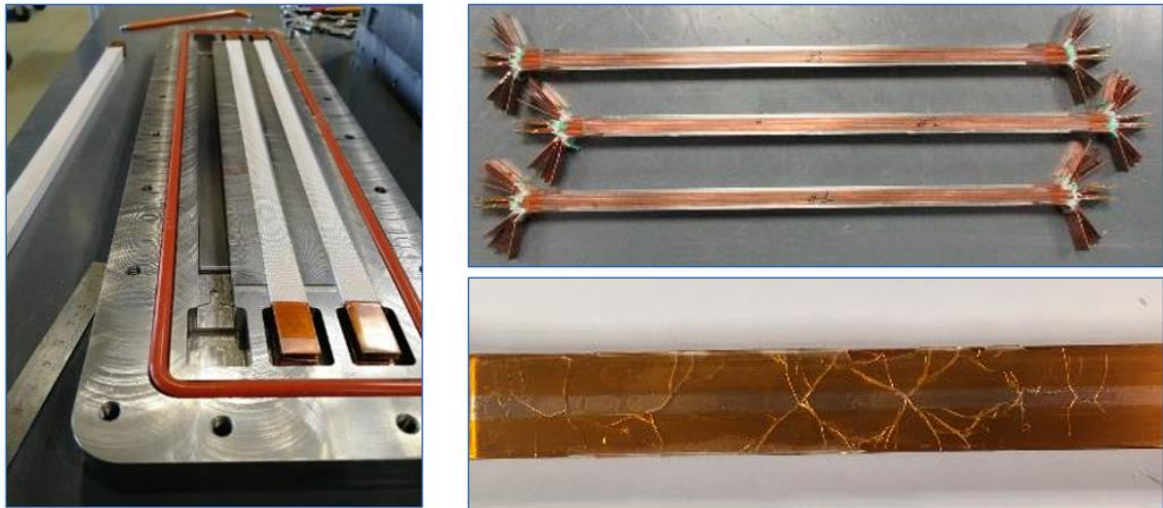


Fig. 6.5 – Impregnation study on cable stacks: the impregnation mould with two cable stacks (left), a batch of three cable stacks (top-right) and observations on resin cracks after thermal cycles (bottom-right).

Preliminary mechanical analyses have shown that impregnating together cables and spacers may be beneficial in terms of stresses in the magnet. The magnet casing will be therefore used as a impregnation mould, allowing to impregnate together all internal components at once. This implies a variation in the geometry, considering the insulation layer's thickness on every impregnated surface, and from a structural point of view it also defines clear interfaces' relationships between components. Cables and spacers will act as a monolithic piece, in the hypothesis that the resin matrix will be able to withstand operational stresses. On the other hand, all the other interfaces will be characterized by frictional contacts. Fig. 6.6 schematizes the behavior at different interfaces.

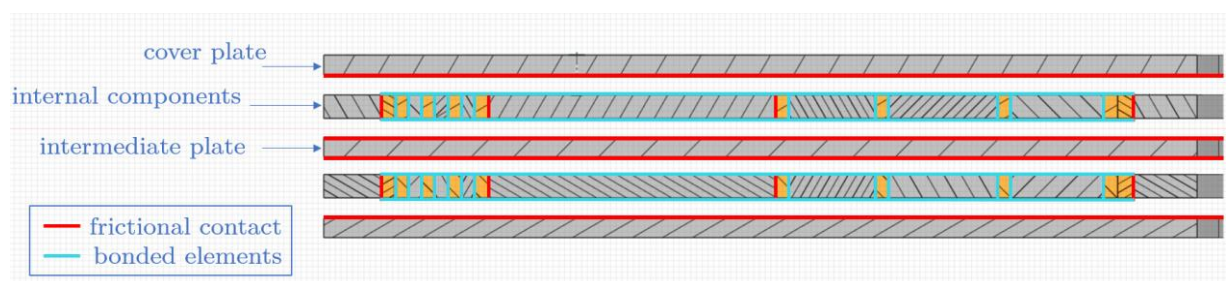


Fig. 6.6 – Schematization of contact interfaces and characteristic behavior of each.

The contact breakdown is presented in table 6.2, listing all interfaces and their relative friction coefficients. These are extracted from an experimentally based database, available at CERN.

Table 6.2 – Contact interfaces and relative behavior.

Interface	behavior	Friction coefficient μ
Cables – Spacers	bonded	-
Cables – Pole	frictional	0.3
Cables – Rim	frictional	0.3
Rim – Cover plate	frictional	0.15
Cables – Cover plate	frictional	0.3
Spacers – Cover plate	frictional	0.3
Rim – Intermediate plate	frictional	0.15
Cables – Intermediate plate	frictional	0.3
Spacers – Intermediate plate	frictional	0.3

As mentioned earlier, bonded contacts are justified if the resin layer is strong enough to withstand the stresses that develop on the surfaces. The origin of such stresses are mainly the differential thermal contractions of the components and magnetic forces, and it is well-known in practice that resin may break in the first powering tests. In fact, real coils are never capable of replicating the theoretical performances of the sole superconductor. Typically, when testing, quenches occur at much lower currents than the ideal ones, and this phenomenon is commonly called “degradation”. However, when repeating subsequent tests, magnets are more and more able to approach the critical current of the cable, and this second phenomenon is called “training”. This has become usual practice in magnet manufacturing, because in fact, the magnet is settling towards a minimum energy configuration: when magnetic forces start acting, there may be regions in which the cable isn’t perfectly supported by the surrounding structure; the cable moves towards the least energetic configuration causing frictional stresses and temperature increase. Quench occurs and the magnet loses all its embodied energy turning it into heat. Once the system has been cooled down it can be powered again and the training proceeds, allowing the coils to be more and more stable. Fig. 6.7 is a typical graph for magnet training, reporting the normalized quenching current I_q/I_c over the number of quenches occurred.

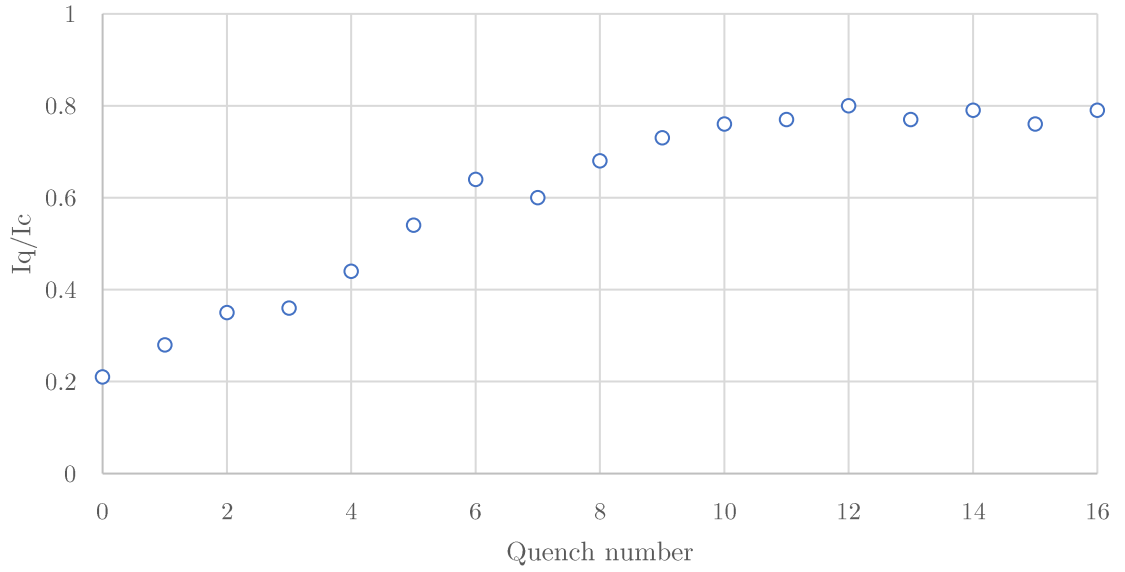


Fig. 6.7 - [26] Typical trend of the normalized quenching current over number of quenches during magnet training.

It is therefore expected that in first tests coils will quench at much lower currents than the characteristic one of ReBCO tapes. Some resin cracking may occur, and mechanical simulations could highlight the most favorable spots.

Now we shall consider some operational necessities and their impact on the magnet design. It is necessary to vary from the ideal coil, composed of grades only, considering the need for electric continuity between grades, layers, and power source. The position of the so-called “grade jumps” and “layer jump” needs to be calibrated to reduce side effects, since their presence perturbs the magnetic field map. This happens in two ways: the presence of a current flowing in a conductor brings a contribution to the field that superposes to the one originated by the ideal magnet. The second perturbation is related to the fact that, near the jumps, grades will see a number of turns that differs from the nominal. There will be two jumps on each grade: one seeing a cable separating from the grade, and the other one seeing a cable merging to the grade. It cannot be avoided that in the section between these two jumps, the total number of cable turns is less than the nominal, and to minimize this effect grade jumps must occur in the shortest distance compatible with the cable’s flexibility.

Jumps and electric connections are decided to happen in the “back” of the magnet, i.e. at greater axial coordinate Z , since the field perturbations decay directly with the distance from the conductor. This ensures minimal field variations, and beam delivery properties are maintained close to the nominal. The two options viable for the grade jumps are both implemented in the magnet, in each of them in a distinct pancake layer, and they are respectively shown in Fig. 6.8 (left) and 6.8 (right).

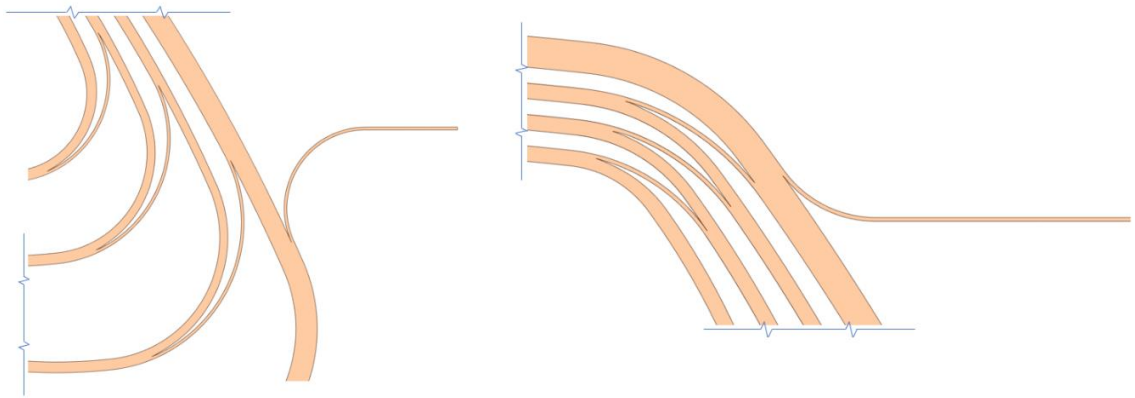


Fig. 6.8 – The two configurations of grade jumps and external electric connections implemented in the demonstrator magnet.

The same issues encountered for the grade jumps apply to the layer jump, that connects the two planar coils. However, the choice of its position is not only driven by operational considerations but involves many manufacturing aspects as well. The cable width of 12.2 mm confers it great stiffness, therefore making it difficult to bend it out of the plane. Multiple choices are available, each one with its advantages and drawbacks. Both the options see the jump between the most internal grades from the two layers; one however occurs in the straight section (Fig.) and the other would happen around the grade. Tools for manual attempts have been machined and different trials have been done looking for the easiest and more robust solution.

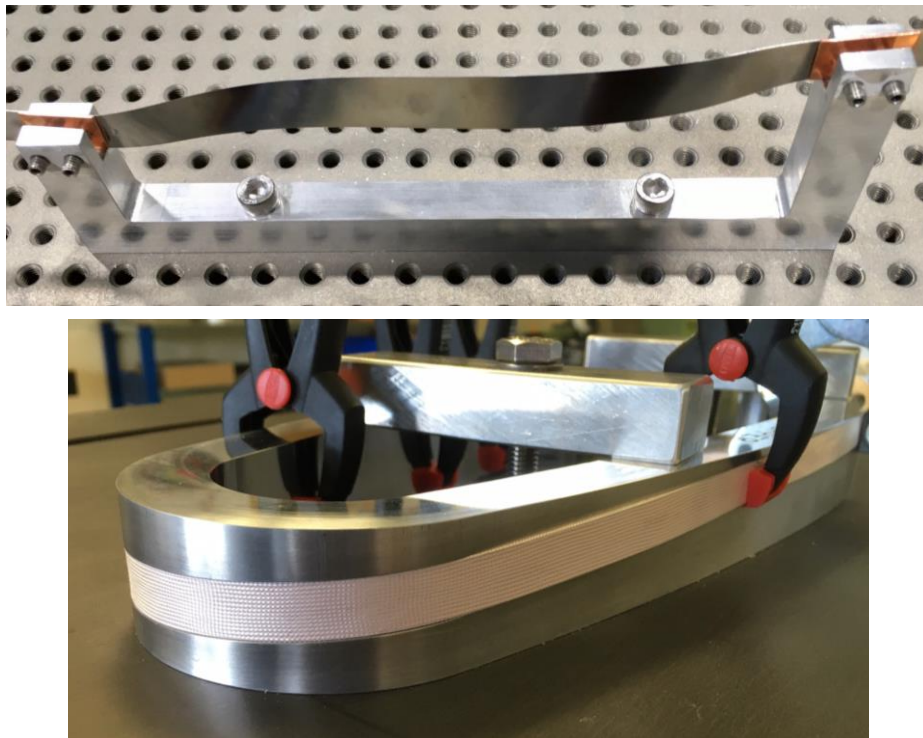


Fig. 6.9 – The two configurations of the layer jump being studied manually.

The layer jump configuration therefore must meet not only the field map requirements but also the structural and manufacturing ones. A similar approach is being followed in the actual design of grades. Fig 6.10 shows the first stainless steel “dummy” coil produced at CERN. Purpose of this demonstrator was to test the winding procedure and tooling to verify its applicability to the real coil, so instead of using copper and ReBCO tapes, stainless steel tapes were wound. Apart from the material, all other parameters, such as the winding tension, were kept as nominal.

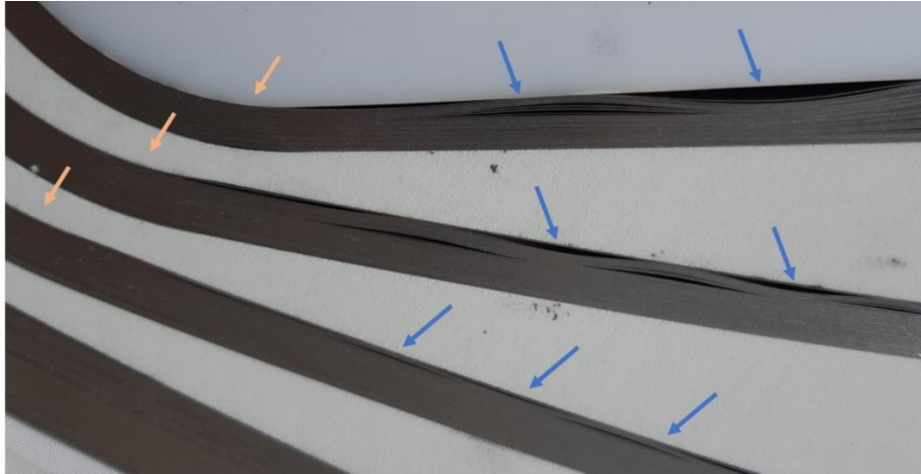


Fig. 6.10 – Undulations manifesting in straight parts of the grades (blue arrows).

The problem that arose after winding is the development of some unwanted undulations in each grade, that we can see pointed from the blue arrows in the picture. After consulting winding experts, it has been established that this effect happens for two reasons. First, there is the settlement of the cables after the winding tension is released; this is an intrinsic characteristic of the process and therefore there is little that design can do to avoid it. The second reason is likely because cables cannot replicate the nominal geometry of the coil made of only circular arcs and straight lines. The imprecision in the shape accumulates at each cable or tape turn, and it produces then this “snaking” effect.

To overcome this latter issue, the design of grades has been varied, replacing the straight grades with large radius-arcs. Therefore, in the regions pointed from the orange arrows, cables will see a smoother transition, thus they should be able to copy it better. All the other structural components follow that configuration resulting in a completely new geometry, illustrated in Fig. 6.11. This geometry represents the baseline of the analyses in this thesis.

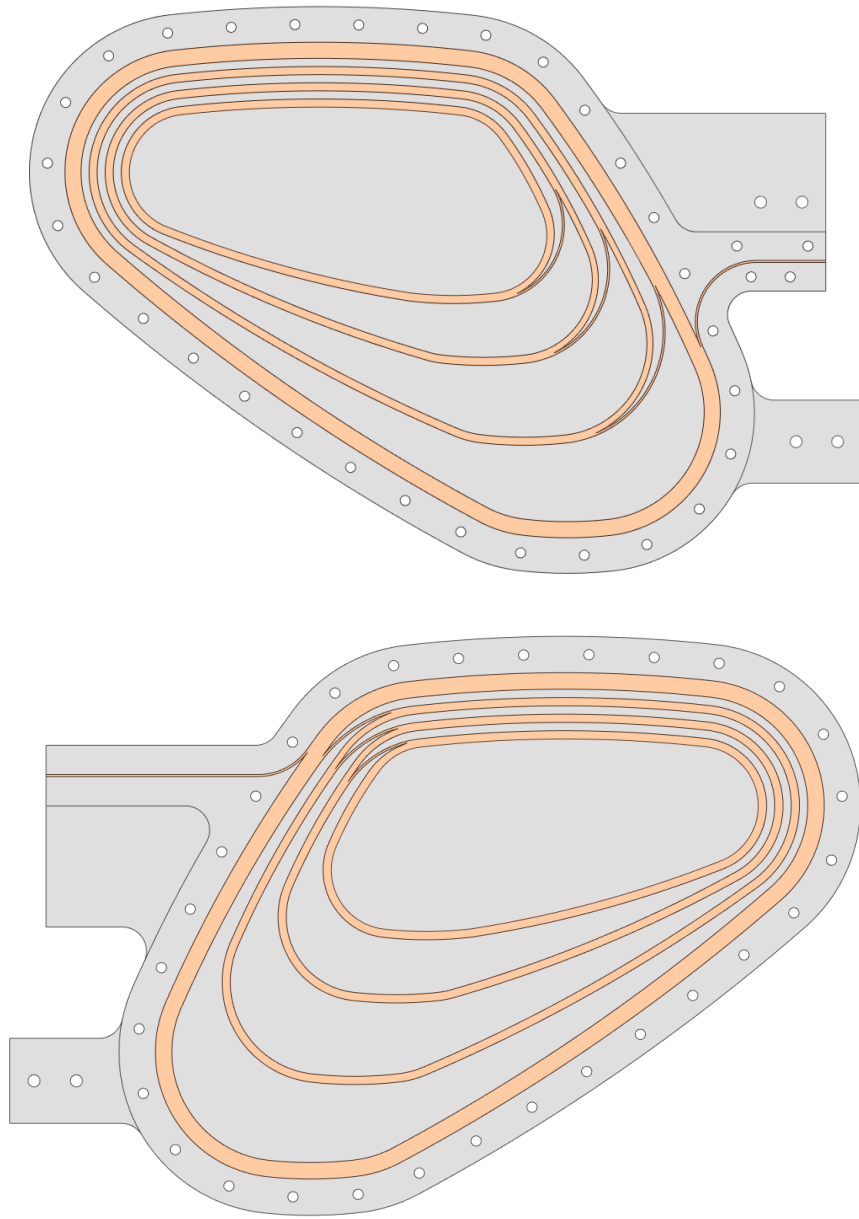


Fig. 6.11 – Baseline geometry of the demonstrator magnet for detailed mechanical analyses.

6.2 Material models

6.2.1 Elastic properties

Most of the components in the assembly would be made of AISI 316L stainless steel, which in the elastic range is easily modeled as perfectly linear, isotropic material. The only exception are coils, the modeling of which requires particular attention.

Coils are made of a stack of cables, wound around steel spacers to match a certain number of turns per grade. The superconductor of choice is the HTS ReBCO (Fig. 6.12a), that comes only in the form of a 100 μm thick tape, due to its manufacturing process. To make one cable, 4 HTS tapes are required. These are piled together without any bonding agent, so that during operation they behave like a single superconductor, and are surrounded by two layers of copper of 550 μm of thickness. Copper acts as a “stabilizer”, which in the magnets’ terminology indicates the conductor that in case of quench carries all the current previously running in the superconductor. For this reason, it is important for the stabilizer to have small resistivity, especially at low temperatures, and usually the choice of a good stabilizer is made upon the RRR. Common solutions are high purity aluminum or Oxygen-Free High thermal Conductivity copper (OFHC), and the latter has been chosen for the GaToroid demonstrator magnet.

The stack of four tapes and two copper strips is then enveloped by a 100 μm insulation layer that can be Kapton or fiberglass, impregnated with epoxy. Ideally the cable’s thickness is of 1.7 mm, resulting from the natural addition of all the nominal dimensions. However, there is much variability due to manufacturing tolerances and process imperfections, and 100 μm of tolerance per cable are kept as a reference for all the components’ dimensioning. A cable becomes 1.8 mm and the cable stack, representative of one grade (Fig. 6.12b), becomes 7.2 mm thick.

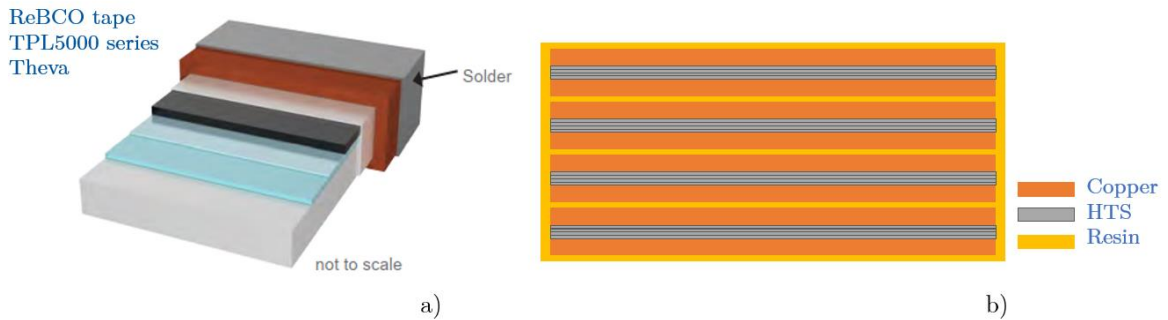


Fig. 6.12 – [32] Architecture of the ReBCO tapes of the TPL5000 series from Theva (a), and cable stack configuration for the GaToroid demonstrator magnet (b).

For mechanical analyses, it must be considered that the material composing the coils is far from being homogeneous and isotropic. However, in absence of data from testing campaigns, a simplified material model can be considered, provided that the elastic parameters (Young modulus E and Poisson ratio ν) are calculated coherently with the loading mode.

Theory and practice of magnet design, but also heuristic studies, show that stresses in coils are generally oriented longitudinally to the cable when cooling and powering. In the case of a planar coil such as the one of the GaToroid demonstrator, Lorentz forces acting in the plane tend to expand the magnet. But since it is wound to make loops, the stresses inside the wire are of tension in the hoop direction. Fig. 6.13 schematizes this situation, where stresses are mainly oriented longitudinally to the windings.

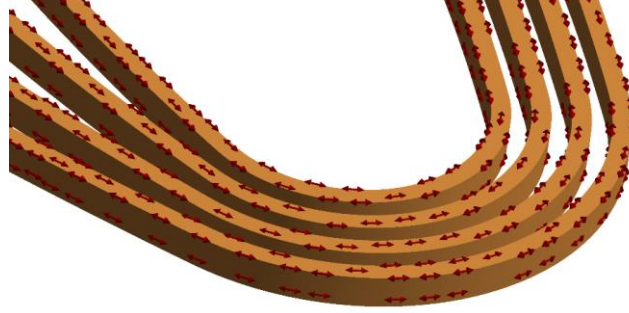


Fig. 6.13 – Expected stress state inside the windings of the demonstrator magnet.

With these assumptions an approximation of the material properties of the cable is made applying the rule of mixtures, looking at a transversal section of the cable and considering the materials' fractions. ReBCO tapes considered as a reference for this study are the TPL5000 PRO-LINE HTS WIRE from THEVA. For this series, the superconductor is deposited on top of a 50 μm thick Hastelloy C-276⁶ substrate, and it is surrounded by a 10 μm thick copper layer. Therefore, these materials' fraction account for approximately 80 % and 20 % respectively, considering negligible the fractions of solder and buffers. Given the substrate's Young modulus, E_{SS} , and the copper one, E_{Cu} , E_{HTS} of a single tape can be calculated as:

$$E_{\text{HTS}} = E_{\text{SS}} \cdot 0.8 + E_{\text{Cu}} \cdot 0.2 = 205 \cdot 0.8 + 117 \cdot 0.2 \cong 187 \text{ GPa} \quad (6.2)$$

Applying once again the rule of mixtures, this time based on the thickness of the tapes, t_{HTS} , and of the copper stabilizers, t_{Cu} , we can compute E_{cable} as:

$$E_{\text{cable}} = (E_{\text{HTS}} \cdot 4) \cdot t_{\text{HTS}} + (E_{\text{Cu}} \cdot 2) \cdot t_{\text{Cu}} \cong 135 \text{ GPa} \quad (6.3)$$

6.2.2 Thermoelastic properties

During the cool down phase, differences in thermal contraction of materials lead to internal stresses in the system. Since this may be the most delicate phase the challenge is to find materials with the closest Coefficients of Thermal Expansion (CTEs), to minimize the differential contractions. As a remark, sensitivity studies for certain CTE's variations have shown how a 10 % difference in CTE can lead to a 100 % difference in average stress in the magnet.

⁶ Hastelloy C-276 is a trademark of Haynes International.

Thermal contraction data are available at CERN [39] for different materials, based on a database of experimental measurements of the relative contraction $\Delta L/L_{293}$ over temperature. Starting from 293 K, thermal contraction information can be plotted over temperature, and as an example Fig. 6.14 represents the ones for the materials involved in the demonstrator.

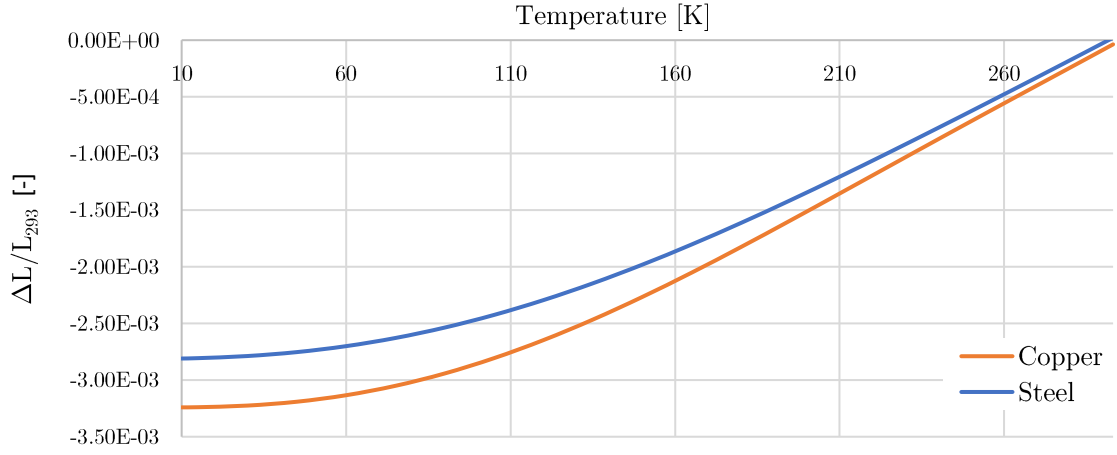


Fig. 6.14 – Thermal contraction data for copper and stainless steel.

Even though mechanical analyses involving contacts have intrinsic non-linearities, materials models in preliminary analyses can be considered linear. This assumption leads to considering the analysis as an evolution between two static configurations, the undeformed and the deformed one, neglecting the stress state evolution between them. The final deformation is clearly affected by such approximation, but the errors committed are comparable with the uncertainty in thermoelastic behavior of real materials. Therefore, instead of an instantaneous CTE value for each temperature (α_t), an integrated CTE (α_s) can be extracted for all materials, considering a thermal contraction ΔL_i and dividing it for the respective thermal excursion ΔT_i . The contraction is therefore considered linear, with slope α_s , and fig 6.15 schematizes this behavior.

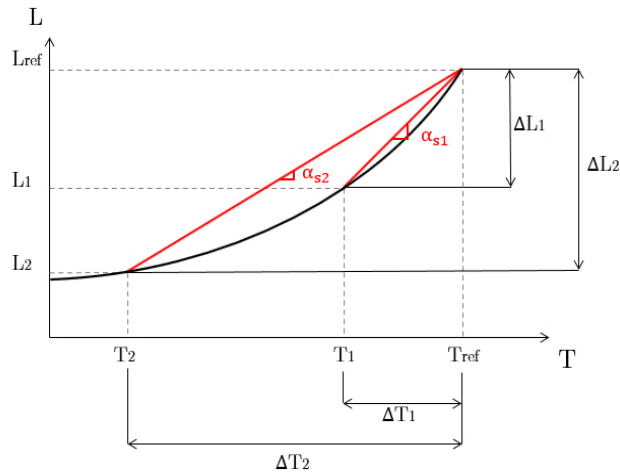


Fig. 6.15 – Schematization of the integration procedure of CTEs’.

6.2.3 Mechanical strength of ReBCO tapes

Even though these properties cannot be considered implemented in the simulation models, we shall recall some important characteristics of the ReBCO tapes regarding their resistance. These generally apply to cables too, and they will allow us to define some qualitative failure criteria. Fig. 6.16 schematizes the most common load case scenarios, and reports for each the relative strength of ReBCO tapes.

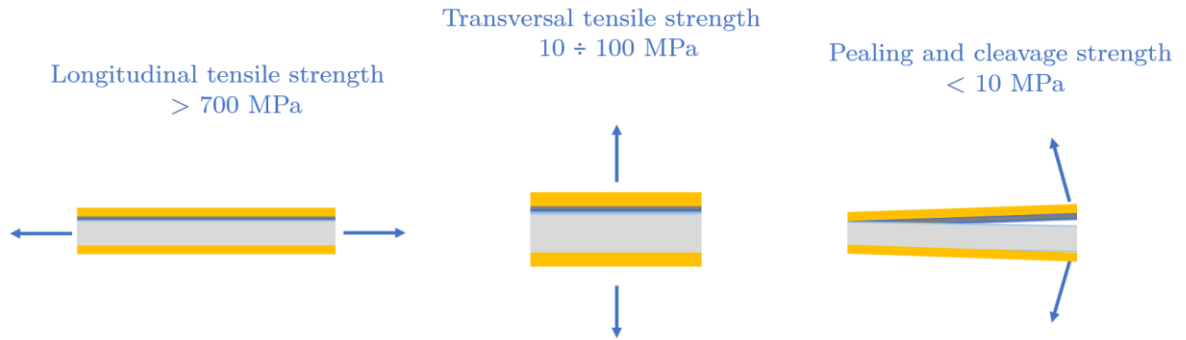


Fig. 6.16 – Schematization of loading scenarios for ReBCO tapes and relative strengths.

Since these tapes come in the form of a stack of plies, deposited onto a stainless steel substrate, solicitations in the transverse direction tend to insist on the bonding strength of the different plies, rather than their mechanical strength. Therefore, ReBCO tapes, and consequently the cables' stacks, must be subjected to loads in a proper manner, to avoid undesired delamination. By looking at the orders of magnitude it emerges that longitudinal tensile stresses are loading the tapes in the most favorable way, allowing the full exploitation of their mechanical strength. On the other hand, transversal tensile stresses are dangerous as much as peeling stress modes, since they are acting directly on the bonding agent which has very little resistance. Therefore, the simulations' results must be carefully interpreted, evaluating the stress modes and eventually proposing solutions to avoid unfavorable loading conditions.

6.2.4 Resin inserts

During an impregnation process resin is generally heated up to temperatures around 150°C . This confers it great fluidity, facilitating the flow between components and ideally allowing the filling of any empty space. To avoid short circuits⁷, the geometry must be accurately designed to let a maximum gap of 0.3 mm between different components. However, such low tolerancing is unattainable in practice, due to the intrinsic nature of the manufacturing process, and some gaps will necessarily be filled by fiberglass fillers. In these locations, so-called resin inserts will be found, consisting of an inhomogeneous mixture of fiberglass and a resin matrix.

In some of the structural analyses led on the magnet it has been decided to account for these effects, to assess the coil response. Seven regions per pancake layer have been recognized

⁷ In this context it means preferential ways for the resin flow, that would prevent the impregnation of the whole structure.

to be likely affected by this problem, and a resin insert has been modeled for each, with a minimum height of 0.3 mm. Fig. 6.17 points out those high-risk regions.

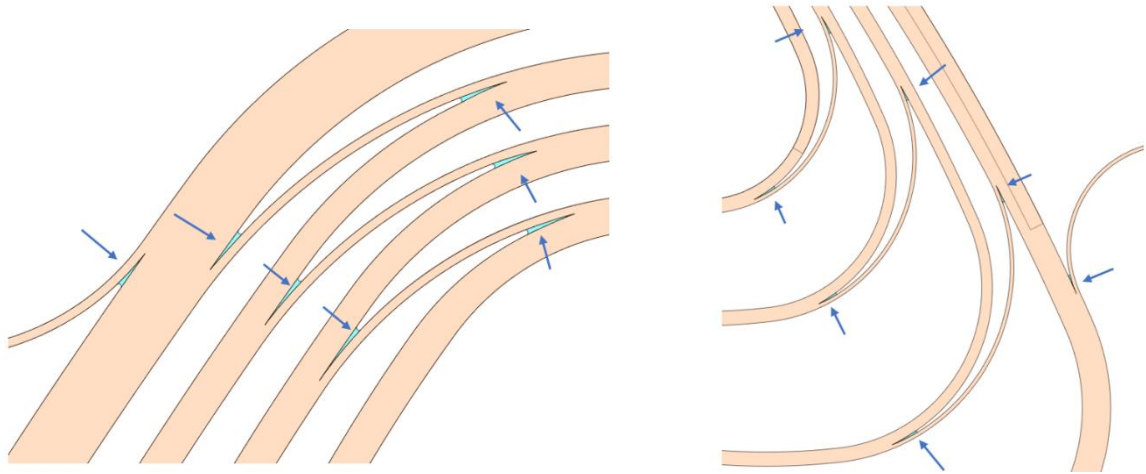


Fig. 6.17 – Resin inserts at cable separations from grades.

However, it must be noted that the effect of these resin inserts on the global stress state of the coils is limited. This is due to their high elasticity, as well as their small dimensions, as compared to the ones of the other components. Moreover, results in the first iteration have shown how these inserts may brake already during the first cooldown. Thus their presence in the model is justified only in the first phases of the cold test.

For these reasons, only two models include these inserts among all the ones analyzed. While the others are left with a gap between coils and spacers, simulating the situation after the resin breakage.

6.3 Load case scenarios and boundary conditions

Among all the processes involved in the operation of the demonstrator magnet we identify the assembling (bolting) process, the cool-down, and the powering, as the most determinant phases for the stress state inside the coil. Even though the first one mainly interests the cover plates and the rim, it is still developing the contact pressure on the impregnated components that will guarantee stability of the system. It is therefore necessary to include this phase prior the others, to evaluate if the bolt pretensioning and the friction developed is sufficient to avoid the slippage of coils and spacers.

The mechanical analyses are led with ANSYS Mechanical and only for some configurations ANSYS APDL was used in batch mode. In any case, the load scenario was divided into three consecutive load steps, each of them accounting for geometric non-linearities. This technique forces the software to update the stiffness matrix of the model at each sub step completed, and the final stress state is much more accurate than the mere superposition of three separated solutions.

To reduce computational resources and allow mesh refinements, the symmetry modeling technique can be adopted. This is justified by the peculiar shape of the magnet, consisting of a quasi-identical double coil layers, in conjunction with the force scheme involved, that

develops mainly in the coils' planes. However, both the sides need to be studied since there are significant differences at the small scale, and the structural response locally can be much different. The two separate models are usually referred to as "Side 1" and "Side 2", and they are separated by a symmetry-plane located in the middle of the intermediate plate, as fig. 6.18 schematizes.

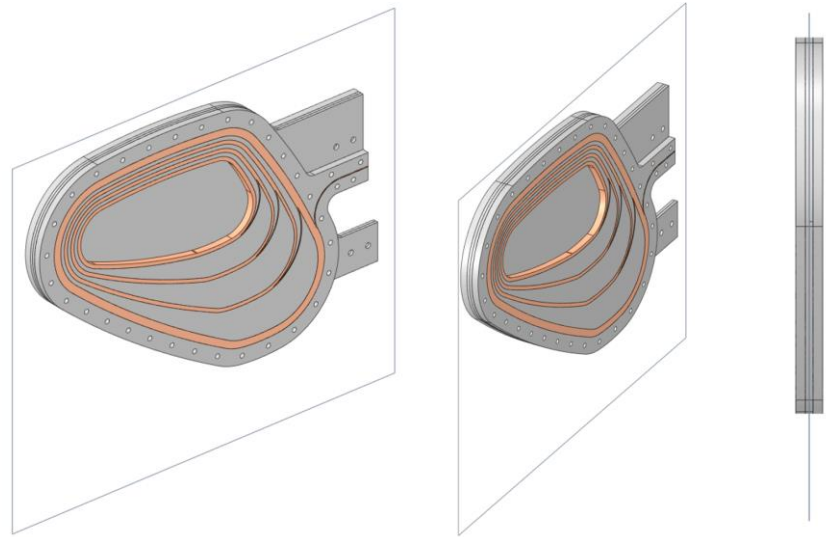


Fig. 6.18 – Schematization of the reference symmetry plane and individuation of Side 1 and Side 2 of the magnet.

The finite element model sees appropriate boundary conditions on the nodes interesting the symmetry plane region. Such constraints avoid any penetration or gap in the direction normal to the plane, but let the nodes freely move parallel to it.

Depending on the approximations made in the electromagnetic model, Lorentz forces may have zero resultant. In principle this should not be the case if considering the sole magnet, since current does not make a closed loop, and the integral of eq. 6.1 is not zero. However, as it will be discussed more in depth in chapter 7, some simplified electromagnetic models do not include grade jumps, and grades make closed loops. Only in this case the model should have no other constraints than the ones to suppress rigid-body motions. However, the ever-present numerical errors drive the necessity of applying external constraints also in this configuration. Four holes to host bolted joints have been disposed for this purpose, to which fixed constraints are applied.

6.4 Analyses' results

As previously mentioned, the mechanical analyses will consist of three different load steps, in which first the bolt pretensioning will be applied, then the cool down to 20.4 K, and finally the magnetic forces. To maintain a coherent framework results for each side of the magnet are presented distinguishing the stress state for each load step. After describing the analyses' outcomes, finally the new geometry of the magnet is presented, and the new stress state following the load steps routine is discussed.

6.4.1 Bolts' preloading

Bolted connections in the FE model are defined in way to represent the configuration schematized in fig. 6.19. The zone of influence of the bolt head and washer has been evaluated according to the ISO standards, characterized by a diameter of 11.5 mm for an M8 screw. Such region has been attached to the screw head, with a “rigid joint”, that would couple all the nodes' translational degrees of freedom. The lower part of the bolted joint is modeled with the same approach, even though the rigid joint is between screw's thread and the cylindrical face of the hole. The preload of the screw in the first load step is ramped from 0 to 13.3 kN, and if it will not unscrew, the bolt's behavior is set to “locked” for the following steps.

As expected, the most solicited regions are those near the bolts, especially in the cover and intermediate plates. With this preliminary value of preload, stresses in such regions reach values of around 380 MPa, which is in most cases high enough to yield structural steel. However, it is common to encounter yielded regions near a bolted connection, therefore these values are reasonable for the purpose set.

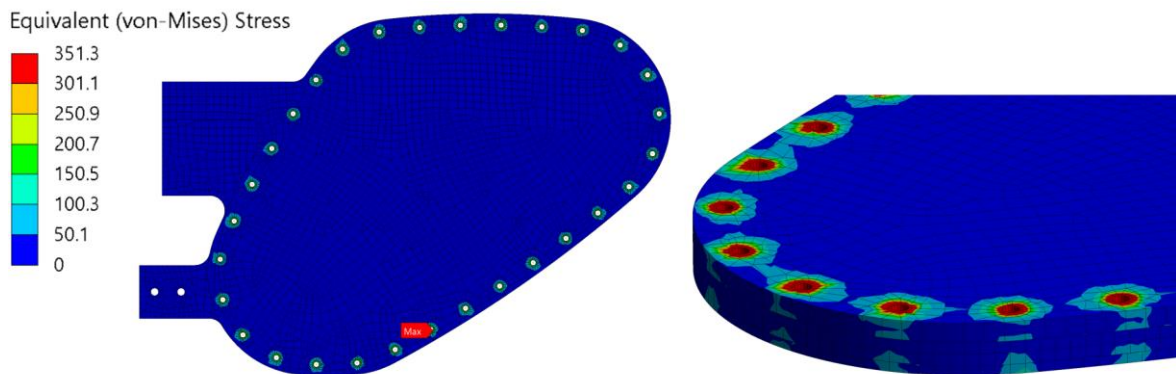


Fig. 6.19 – Visual representation of the FE results after the bolts' pretension. Stresses are expressed in [MPa].

It is instead interesting to focus on the coil and see the effects induced on them by the preload. Accordingly with the previous preliminary studies, the contact between the most outer cable and the rim has been set to frictional with a friction coefficient μ of 0.3. Because of this high value, when the rim is compressed by the bolts' preload, the force transmits also to the windings through tangential stresses that develop on their outer surface, tending to compress them too. The effect happens on both sides of the magnet but with different stress

peak values; however the deformed shape is similar, and an example can be appreciated in fig. 6.20.

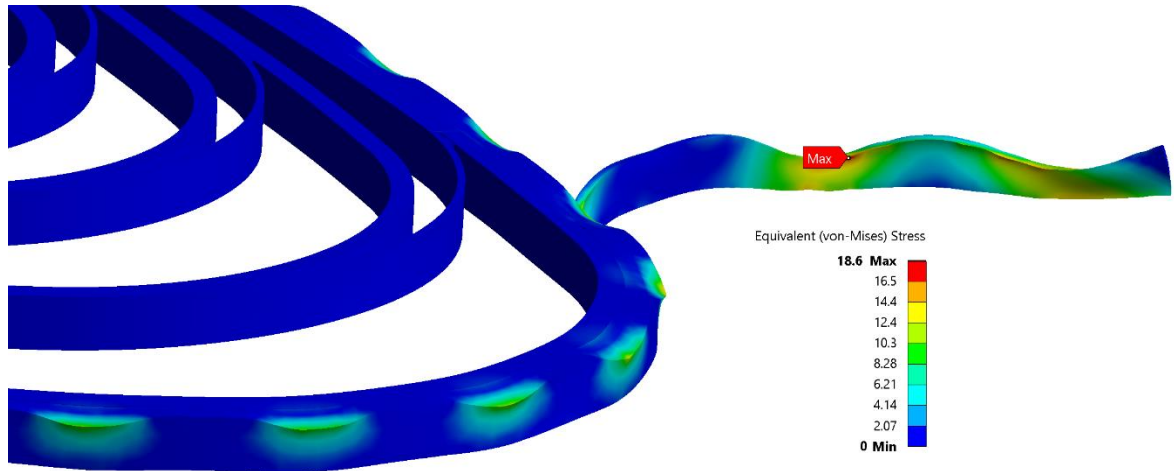


Fig. 6.20 – Visualization of the effect of the bolts' pretension on cables. Stresses are expressed in [MPa]. Deformed shape enhancement factor: 500x.

If the stress peak values can be considered by no means dangerous, it has to be noticed that the stress mode is peculiar, and considering the cable's architecture, non-linearities could arise such as tapes slippage and debonding. In light of these considerations, a surface coating on the rim to reduce its friction on the cables is justified. Based on internal practices at CERN the best option seems to be a Polytetrafluoroethylene-based spray, to be applied before assembling.

6.4.2 Cryogenic cooldown

For both sides of the manet this phase represents the most severe one in terms of stresses, and the cause are the materials' different CTEs'. It must be mentioned that these results are also strongly dependent on all materials' properties, hence variations not only in CTEs' but also in Young moduli E and other elastic properties may have a strong impact on the magnet response. Moreover, the model is approximated, and a strong difference is made by the lack of the pole in the simulations. Therefore, these results are ment to highlight eventual problematic regions basing on the coils' configurations only, and to produce an indicative stress map to be considered in the geometry optimization process, independently of the material properties.

Prior to any in-depth analysis of the stress state, which can be done only through Finite Elements Modeling, it is useful to have an analytical counterproof of the total deformation of the magnet, since it is the only quantity that can be computed manually with a sufficient degree of accuracy. Fig. 6.21a shows the measured distance between the two furthest regions in the CAD geometry, accounting for around 760 mm. Considering an integrated CTE for Stainless steel of $9.9 \times 10^{-6} \text{ }^{\circ}\text{C}^{-1}$ and a thermal excursion ΔT of $-274.75 \text{ }^{\circ}\text{C}$, from room temperature ($22 \text{ }^{\circ}\text{C}$) to 20.4 K, we can compute the expected thermal contraction Δl as:

$$\Delta l = \alpha_{ss} \cdot l \cdot \Delta T \cong -2.06 \text{ mm} \quad (6.4)$$

Comparing it to the Finite Element calculations, Fig. 6.21b, it emerges that results differ of about 0.05mm, accounting for 1.5 % of the total deformation; hence the two models are considered coherent withing enough tolerance for our purposes.

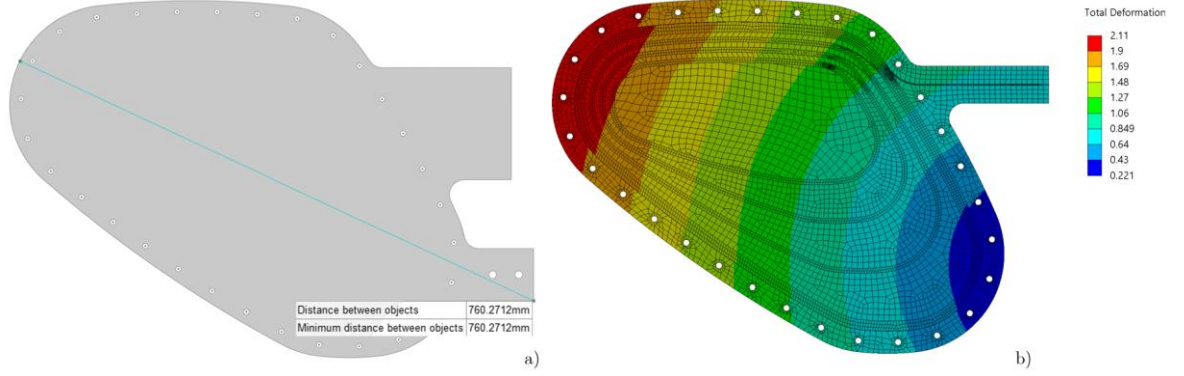


Fig. 6.21 – Dimension scale of the demonstrator magnet (a) and global contraction upon cryogenic cooldown (b). Total deformation units are [mm].

At this stage, a consideration shall be done on the components' thermal contraction, to have a qualitative estimate of the stress state. Since the material model for the HTS cable stacks has a higher CTE compared to the one of Stainless Steel, respectively $11 \times 10^{-6} \text{ }^{\circ}\text{C}^{-1}$ against $9.9 \times 10^{-6} \text{ }^{\circ}\text{C}^{-1}$, the coils are expected to be constrained by the spacers in their contraction, since the latter would eventually shrink less. Therefore, cables are forced to cover a greater distance along the winding path, and the resulting stress is positive and orientated longitudinally. Below a certain threshold, this stress mode is compatible with the material's strength characteristics, since we have seen schematized in Fig. 6.16 that even ReBCO tapes can withstand high longitudinal stresses before yielding.

In light the global adherence of the Finite Element model to the analytic one, an analysis of the stress state calculated inside the windings is done. For practical reasons, the results on the Side 1 of the magnet are presented first. Here a vector plot helps understanding the first principal directions and lets immediately emerge the coherence of the model to the qualitative estimation just made. Red arrows in Fig. 6.22 are representative of principal stress directions at different locations, and it can be noticed how almost all of these are directed tangentially to the windings. Only a few perturbations can be spotted, especially in the grade jumps regions, due to some stress concentrations effects.

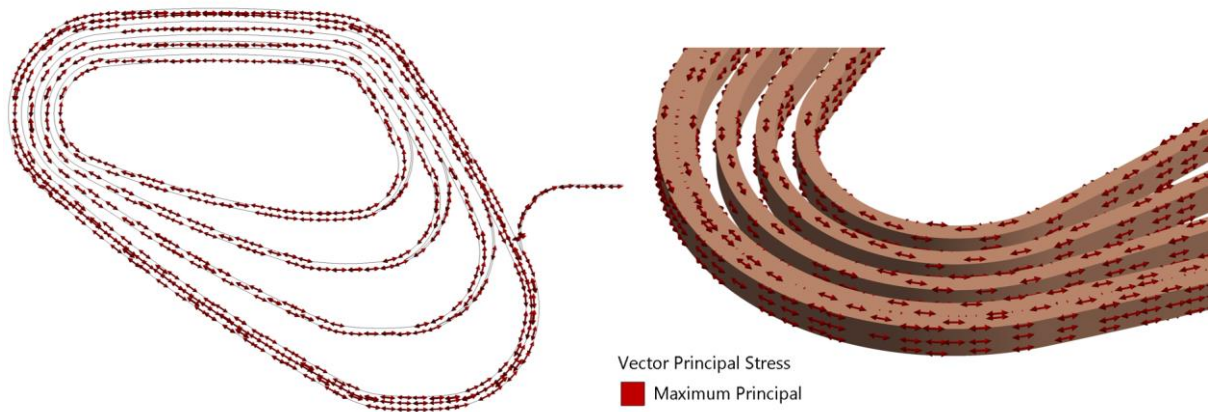


Fig. 6.22 – Major principal stress directions inside the windings after cooling.

Another proof of the coherence of the results may be the contact pressure at the various interfaces. This is made easy by the modelling technique adopted, that instead of having a conforming mesh between the impregnated components sees bonded contacts at all round the various interfaces. The stresses retrieved with ANSYS contact tool are plotted in Fig. 6.23 in the form of contact pressure. Positive values are to be intended as compressive pressure, whether negative values represent tension stresses at the interface.

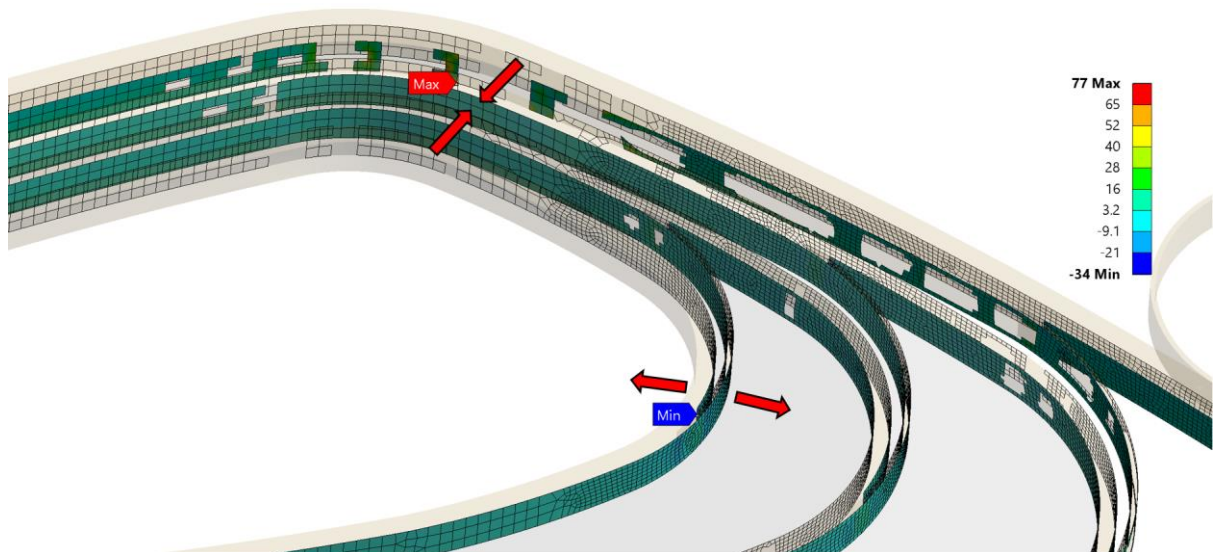


Fig. 6.23 – Visual representation of the contact pressure at various interfaces. Pressure units are [MPa].

The region identified by the “Max” label, coincides with the interface between a cable stack and the more internal steel spacer. Here, the positive pressure that develops indicates the will of the coil to shrink more than the spacers and is hence coherent with what mentioned before. Apart from this specific region where the peak develops, that could be also due to numerical imprecisions, the rest of the coil sees a more even distribution of the contact pressure, with values oscillating between 10 and 20 MPa.

If positive contact pressure is not dangerous for the cable integrity, negative values are. It is therefore necessary to investigate on the nature of the minimum “peak”, identified by the label “Min”, that develops during cooldown.

Once again, this can be imputed to the CTEs’ differences, since the most internal grade shrinks more than the spacer just surrounding it, and a decohesive tension develops then between these. It must be remembered however, that the central pole is missing from this model for the aforementioned reasons. In a different configuration that would see its presence, the internal grade would see another component to restrain its shrinkage, and this would happen from the inside. At this stage, the contact pressure values cannot be estimated, but clearly the new constraint develops a positive pressure at the interface, and this is by no means harmful for the coil. On the contrary, the presence of the pole is expected to have beneficial effects on the whole coil, and it is the reason why it has been included, basing on the preliminary studies mentioned at section 6.1.

The general picture of the maximum principal stress is presented below in fig. 6.24.

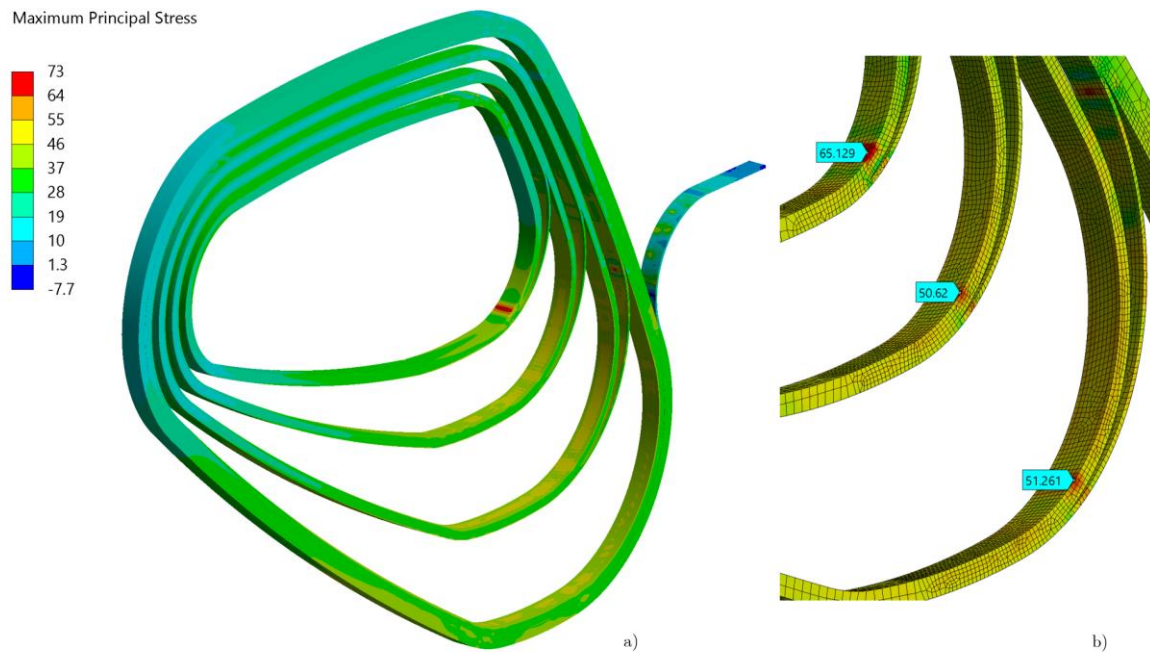


Fig. 6.24 – Representation of the global stress state after cryogenic cooldown. Stresses expressed in [MPa].

The even coloring of grades is sign of a well distributed and homogeneous stress state inside the windings, sitting on average at around 30 – 40 MPa. However some of the retrieved punctual values of the stresses, shown in Fig. 6.24b, highlight some localized effects nearby grade jumps⁸. Given the peculiar shape of the windings in such regions, this phenomenon may be understood as the usual stress concentration near a sharp edge, that would lead to a delamination of the cable stack and a crack propagation.

⁸ Note that the color band scale has been re-set in fig. 6.24b, to enhance the visualization of the stress peaks.

In fact, an in-depth analysis has been carried out to find out the nature of these stresses. Starting from a mesh sensitivity study it has been noticed how peak values are mesh-sensitive: a coarse mesh for the stainless steel spacers has a great impact on the stress at the interfaces with cables, since the curved contour is worse approximated and the sharp angles at nodes produce unwanted stress spikes. Fig. 6.25 below clarifies this statement with a theoretical schematization on the left, and the results of a mesh refinement on the right.

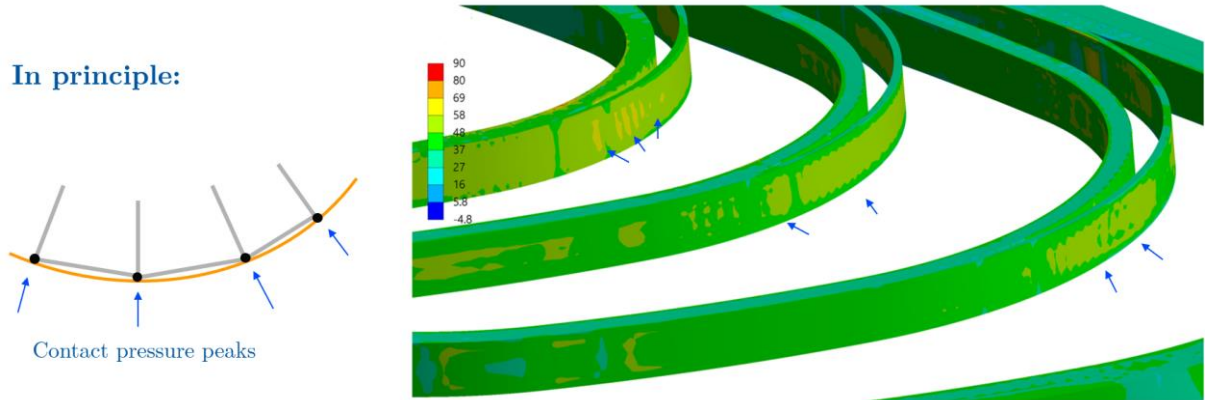


Fig. 6.25 – Schematization of the effect of a coarse mesh approximating curved boundaries (left), and stress spikes at nodes locations (right). Stresses expressed in [MPa].

A finer mesh for the spacers leads to more uniform results along the windings, and in fact this trend is the opposite of what some would expect when investigating stress concentrations. Therefore, since the model is tending towards uniformity in stresses, and since further mesh refinements imply serious consequences on the computational time demanded, it has been agreed that the latest results are valid, and the stress peaks are considered as numerical imprecisions.

Moving now to the second side of the demonstrator, the global stress state remains the same. Even though this side is characterized by shorter and sharper grade jumps, as can be seen in Fig. 6.11, these cause no perturbation to the winding stress mode. Principal stresses are still dominated by the longitudinal fraction developed during cool down, and again they amount for around 30 – 40 MPa evenly distributed round the windings.

Fig. 6.26a shows the overall picture of the stress state in the windings. The uniform green color of the windings remarks what said about the stress homogeneity⁹ along in the cables; however, the red and purple region near the inlet cable are clear signs of a stress concentration. In Fig. 6.26b, a close-up view of the stress peak area shows in fact how there are two subsequent high-stress regions.

⁹ Note that this picture represents in fact the Von Mises Equivalent stress, based on the well-known formula:

$$\sigma_{eq} = \sqrt{\frac{1}{2}[(\sigma_{xx} - \sigma_{yy})^2 + (\sigma_{yy} - \sigma_{zz})^2 + (\sigma_{zz} - \sigma_{xx})^2 + 6(\tau_{xy}^2 + \tau_{yz}^2 + \tau_{zx}^2)]}$$

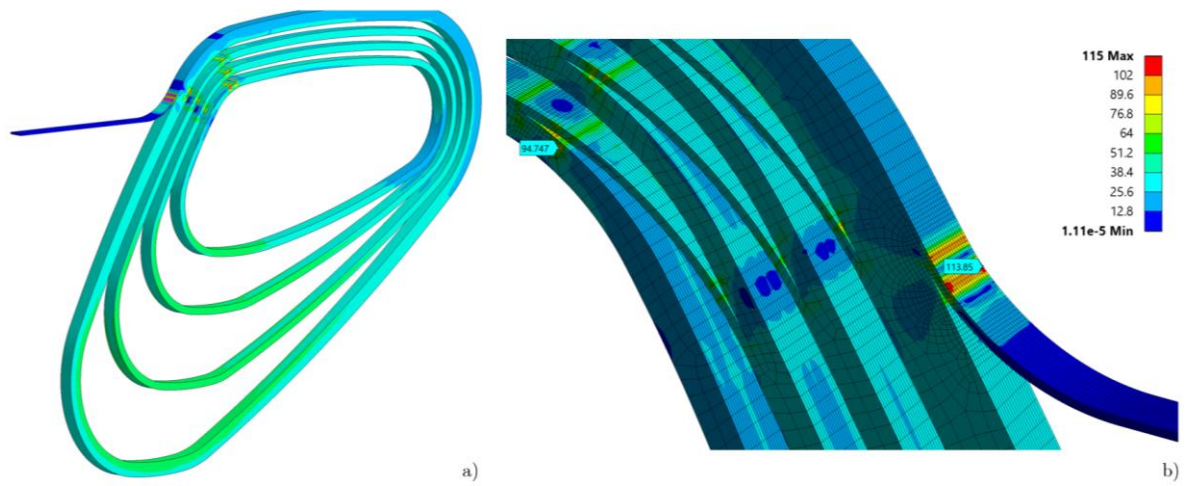


Fig. 6.26 – Overall picture of the stress state inside the windings (a) and close-up view of stress concentration in a specific location (b). Stresses expressed in [MPa].

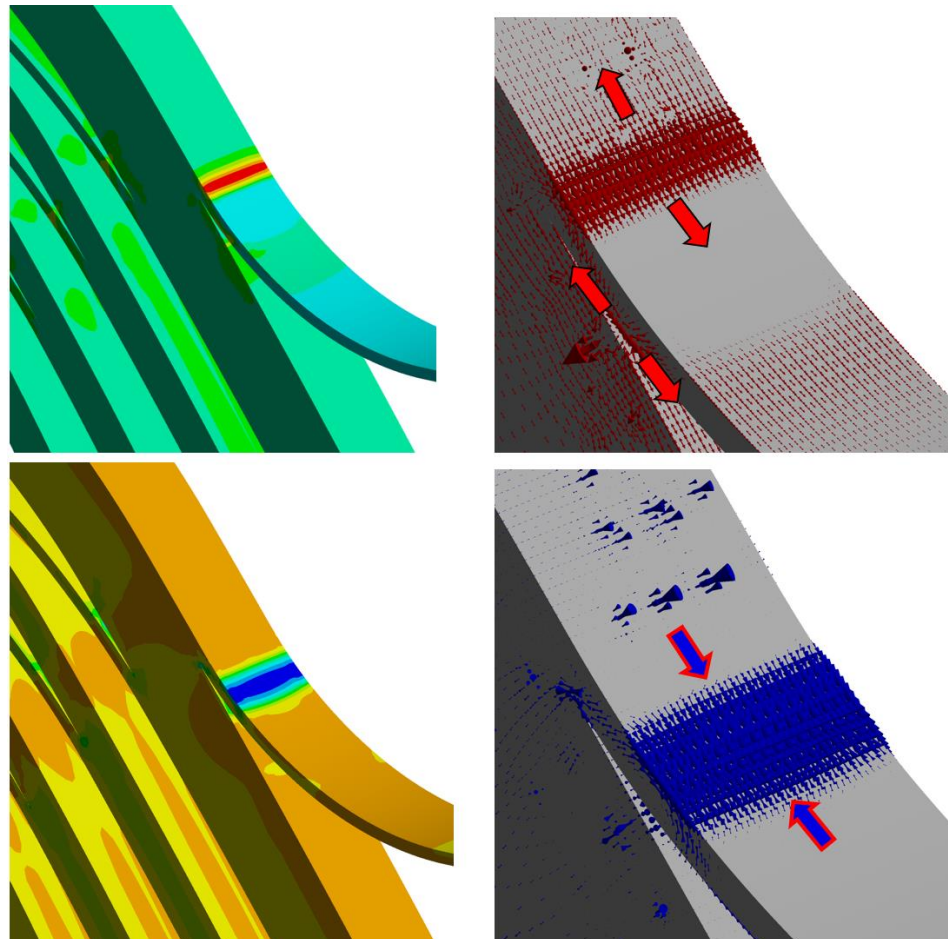


Fig. 6.27 – Close-up view of the stress concentration regions and investigation on the principal stress directions.

The region is characterized by an alternation of tensioned and compressed regions, Fig. 6.27, usually characteristic of a non-linear buckling behavior. Since a non-linear solver is used, effects like this can be grasped.

Most likely this phenomenon occurs because the current inlet follows a long and straight path from the outside toward the coil. In its final region, the arc followed by the cable may be too abrupt and the accumulated tangential stresses release find a way to release in this high-curvature region.

Despite this effect being very clear qualitatively, the model is made up of too many assumptions and approximations to repute significant the numerical values. Therefore this stress analysis can only evidence the presence of an eventual structural problem if this winding configuration is maintained.

6.4.3 Powering and magnetic forces

Source of Lorentz forces are the electromagnetic calculations described in the following chapter. After calculating the current density inside the windings, and the magnetic field generated from them, forces acting on the single elements are computed as described in equation 6.1.

The general forces map has been calculated with a simplified coil configuration that avoids modelling cable jumps and current inlet or outlet. This has been justified by different considerations that will be found in the relative chapter. Post-processing of these forces has however been necessary to correct forces F_g acting in the coil plane, since numerical errors in the FE approximations led to non-zero resultant. The forces' pattern can be appreciated in Fig. 6.28 that also offers a more detailed view of the force map in proximity of the high-field region.

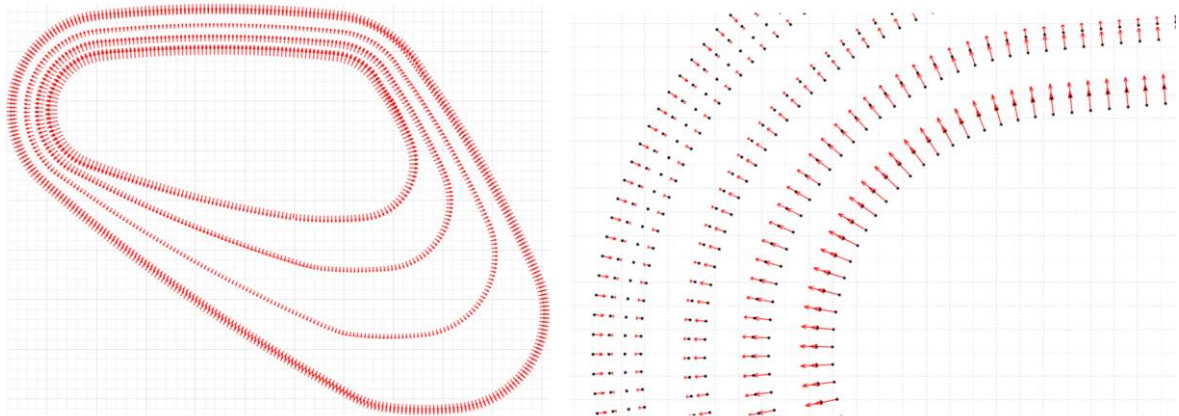


Fig. 6.28 – Vector representation of the Lorentz forces at discrete locations along the coil.

From this image it can be qualitatively appreciated that the forces tend to expand the coil in the plane. This finds its proof in the mechanical calculations made with ANSYS: stresses that were oriented longitudinally are even more increased, even if by only a fraction of the original values. Overall the stress increase accounts for about only 20 MPa and seems like it is not causing any further problems for the coils' integrity. Cables in delicate regions such as the jumps tend to approach together rather than separating and menacing delamination.

The second effect of Lorentz forces can be grasped if considering the two planar coils composing the magnet as a set of parallel conductors, in which current runs through. This leads to the same attractive forces observed by Ampere and then explained by Biot-Savart's law, accounting in our case for about 109 kN.

If dividing it by the surface area of the windings, that is around 41'830 mm², we obtain an ideal contact pressure increase of 2.6 MPa. Unfortunately such a small pressure increase is hard to grasp by means of the FE model, since geometric and mesh irregularities lead to a non-even contact pressure distribution along the windings: spikes of 10 MPa are followed by unperturbed zones, where stress sits low to 0 MPa.

For all these reasons the powering phase of the magnet is not considered so far as a crucial moment of the tests, and on the other hand much care must be put in the geometric tuning to minimize the stresses developed during the cool down process.

6.5 Second design iteration

The final phase of the design process sees further geometrical changes, spurred both from the stress state assessment and from new technological requirements.

Regarding the structural behavior, main concern is the cable instability that arose in the last simulations of Side 2. The rest of the coil is instead interested by an even stress state that does not seem harmful if considering the direction of action and the intensity. Therefore only minor details need to be defined, while the general configuration of the magnet can be considered stable.

Such minor changes are driven by technological necessities that arise mainly in the manufacturing process. Among them, the winding tension plays a major role, since it must be ensured that each tape composing the cable is constantly kept under a predefined tension during winding. Consequently, the two rims have been adapted to let the cable inlet and outlet run in a straight line from the coil to the outside.

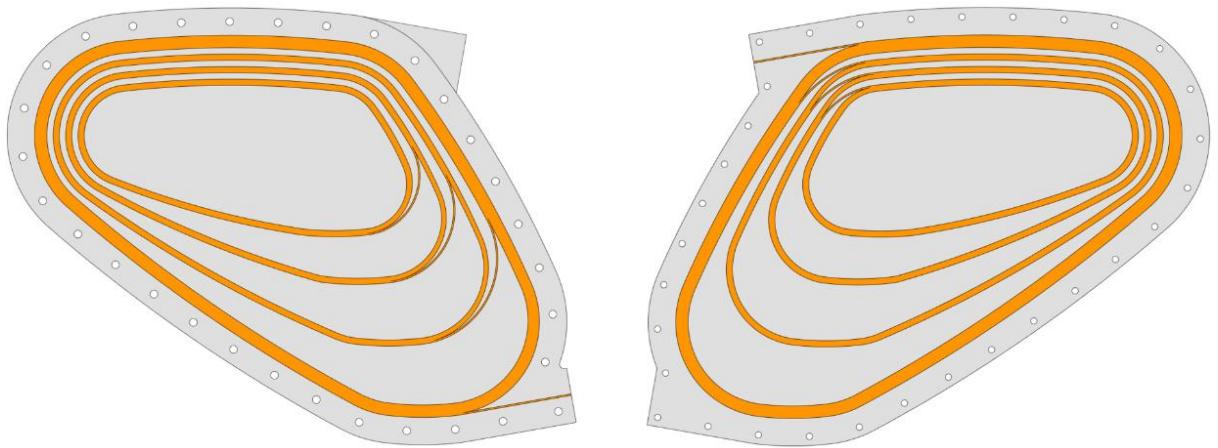


Fig. 6.29 – Final geometric configuration of the demonstrator magnet.

6.5.1 Results

Considering that the cool down phase is the most crucial for the stress state, it emerges that also a 2D analysis may be sufficient to grasp the interactions that develop during this phase. The advantage of a 2D analysis is mainly the reduced complexity of the model, both from the modeling point of view and from the computational one. It allows therefore to reach more accurate in-plane results, since the mesh density can be much increased.

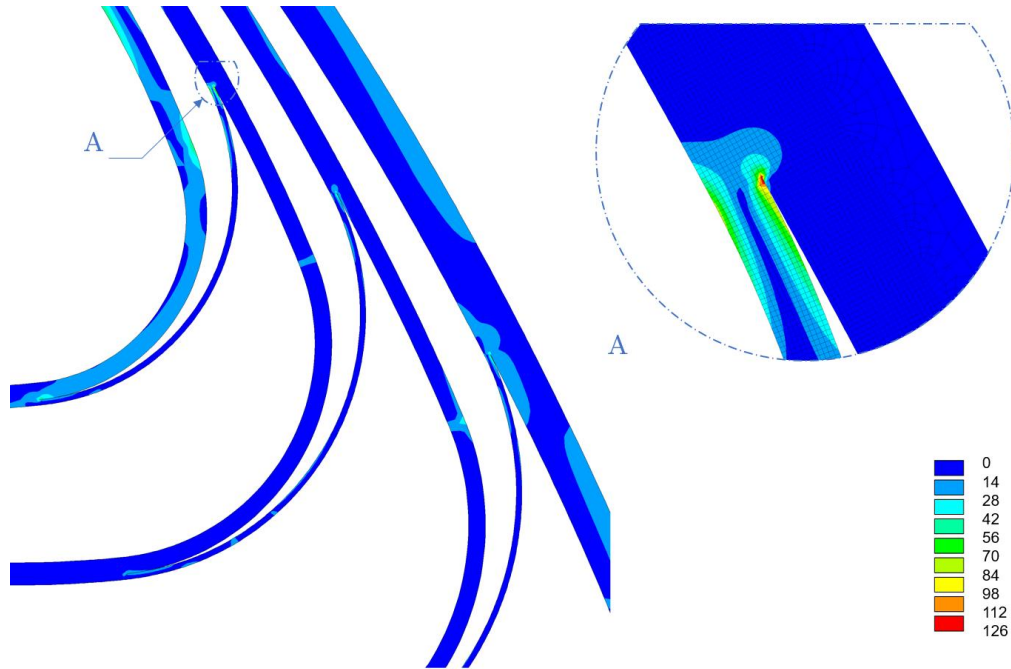


Fig. 6.30 – Visual representation of the maximum Von Mises equivalent stress inside the windings. Stresses expressed in [MPa].

Results are briefly represented in Fig. 30, showing once again an even stress state inside the coil, and a very localized stress peak in the proximity of a grade jump. By investigating on the principal stress directions along the cable thickness it emerges that the stress state can be reconducted to the case of a bending load summed to a tension load, as schematized in Fig. 31.

Despite the phenomenological aspects of this stress peak being not evident, it can be stated that both the stress intensity and its direction (longitudinal along the cable) are not harmful for the cable integrity.

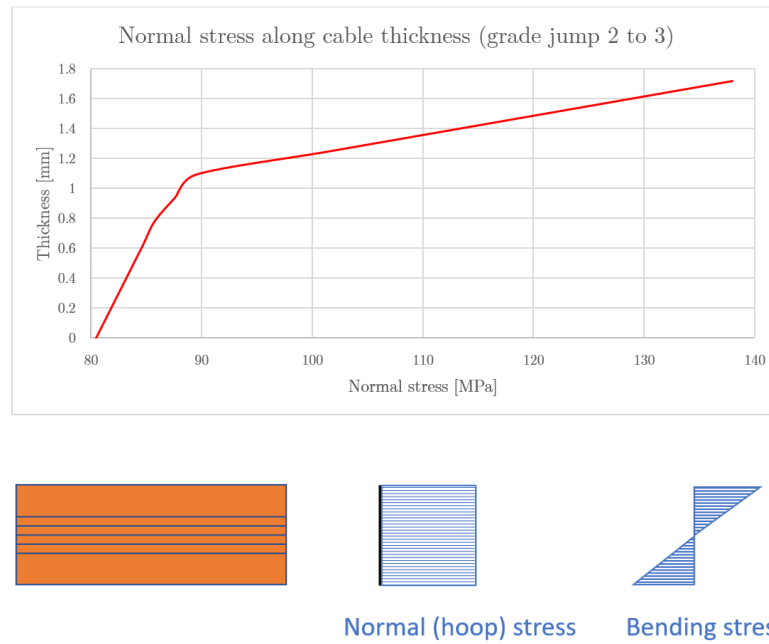


Fig. 6.31 – Plot of the maximum principal stress along the along cable thickness, and schematization of the stress state origins.

Moving to the 3D approach, the results just showed can be taken as a reference, key-point of which is the localized stress peak. The model is now able to simulate the magnet in its integrity, accounting for bolting, cryogenic and powering loads.

First observation worth mentioning is that the stress peak values after bolting have decreased from 380 MPa to 145 MPa as can be seen in Fig. 32.

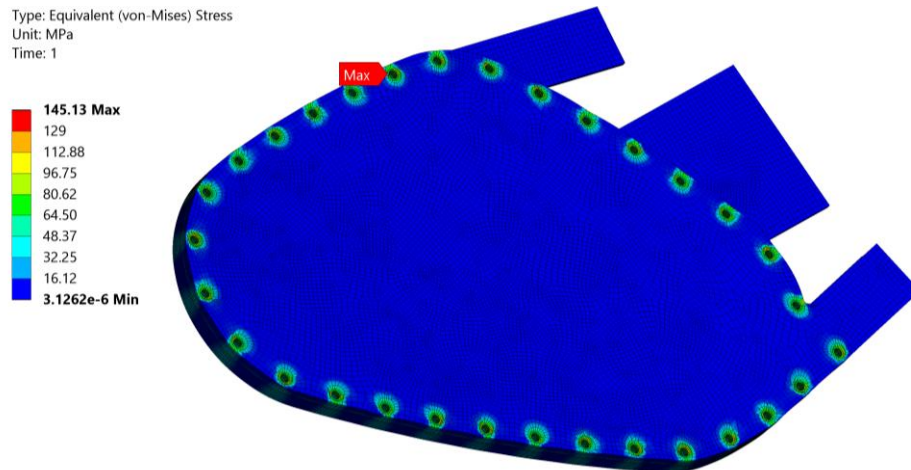


Fig. 6.32 – Stress state on cover plate after bolt pretensioning.

The reason for this shall be sought in the new boundary conditions applied to the bolts, as the design has moved from threaded holes inside the intermediate plate to through holes. As a result, the previously threaded regions inside the intermediate plate are no longer affected by such high stresses. The stress peaks are now registered on top of the cover plate, in the regions where the washers come to contact with it.

Moving to the second and third phases of the analyses the attention goes to the coil only, considering that it is the most delicate component in the assembly and also because it is the one seeing the more dramatic stress increase. The evolution of the maximum principal and minimum principal stress peaks in the windings is presented in the graph in Fig. 6.33.

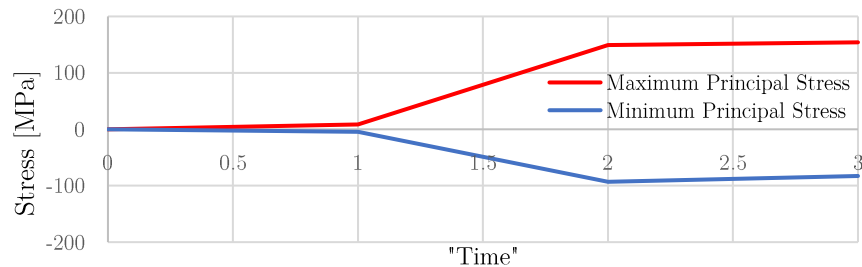


Fig. 6.33 – Evolution of the maximum and minimum principal stresses inside the windings after the three consecutive load steps.

Once again, the cooldown to 20.4 K (from time = 1 to time = 2) determines the majority of the stress state inside the coils, moving from 8 MPa to 149 MPa for the maximum principal stress, and from -4 MPa to -93 MPa for the minimum principal one.

Interesting fact is that even though the maximum stress peak registered is in the order of magnitude of the one foreseen by the 2D analyses, its position inside the coils has changed from one grade jump to another, Fig. 6.34 . There are no immediate explanations to this fact, apart that this phenomenon emerges from the CTEs differences. As a consequence, coils are subjected to a system of internal forces that discharges itself in the more flexible regions, the two grade jumps being ones of which. The unpredictability of the exact position is due to the problem nonlinearity, and the only parameter of interest becomes the stress magnitude. As mentioned earlier, values of the order of 149 MPa are by far inside the cables' resistance, and therefore should not represent a major concern. Along the rest of the windings the stresses distribution remains even, with values ranging on average from 30 to 40 MPa.

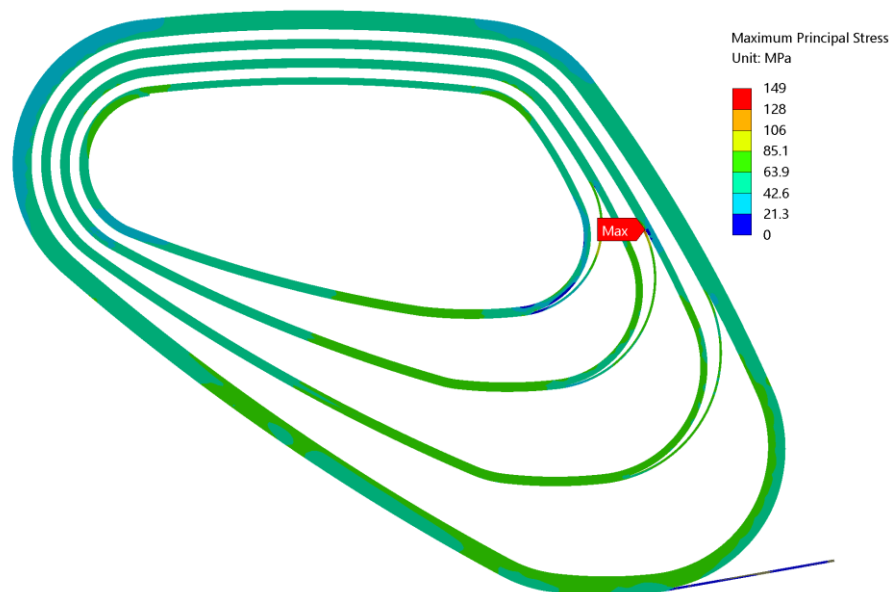


Fig. 6.34 – Overall stress state inside the windings after cryogenic cooldown.

The influence of Lorentz forces can be grasped already in the graph of Fig. 6.33, where we can see that the stress increase is relatively low. However, a better overview of the stress state inside the whole magnet is offered from the graph in Fig. 6.35, which reports the evolution of the Von Mises-equivalent stress during the various load steps.

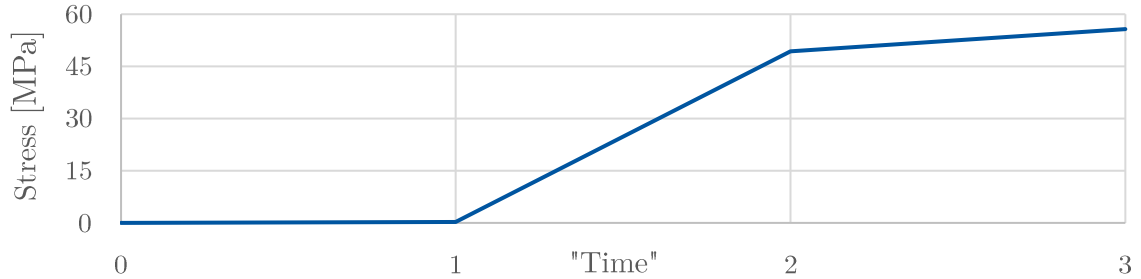


Fig. 6.35 – Evolution of the mean value of Von Mises Equivalent stress state inside the windings over the three load steps.

The average stress passes from 49 MPa to 55 MPa, and by looking at the principal stresses we can see that the overall stress state in the windings remains the usual tension one. Fig 6.36b shows this situation, with red arrows representing the maximum principal stress directions aligned longitudinally to the windings.

Moreover, since the effects of these forces is mainly tending to expand the coils, eventual dangerous stress states around the cable jumps are mitigated, tending to close the two flaps. Fig. 6.36a schematizes this situation, showing with blue arrows the minimum principal stress directions. In this case we can see that the tendency is to act in compression, thus closing the gap.

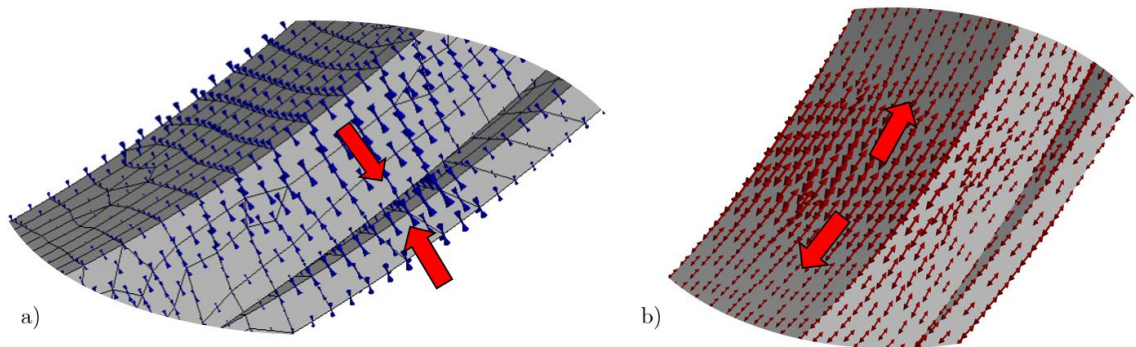


Fig. 6.36 – Effects of the Lorentz forces on the windings: closure of the cable separation regions (left) and increment of longitudinal stresses along the windings (b).

7. Demonstrator magnetics

In chapter 3, it has been pointed out that the demonstrator magnet is being built to assess the technology status and the adherence of its numerical models to reality. This is a crucial aspect in the design process, as a complete understanding of the phenomena at a smaller scale is mandatory before moving to the large-scale models, where the complexity could eventually turn out to be overwhelming. In a superconducting magnet, besides the mere structural and technological aspects, the major milestone is to achieve a precise prediction of the actual magnetic field map as it must be well-known to make predictions on the beam path.

In this framework, electromagnetic simulations are led, evaluating the field expected from the demonstrator with different degrees of accuracy. By following an incremental procedure in the models' complexity, these studies also give a mean for estimating the committed error with different approximations. Three models representing the same side of the magnet are subsequently analyzed, and each time the model has been enriched of details. Finally, the most precise field map is shared between different working groups to study the optimal positioning of magnetic sensors and perform particle tracking simulations.

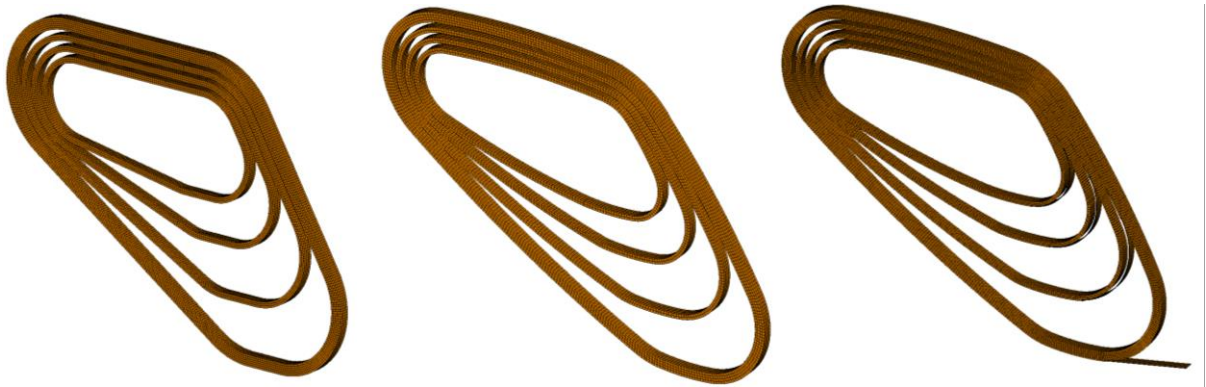


Fig. 7.1 – Presentation of the three finite element models approximating the windings of the demonstrator magnet.

7.1 Preliminary studies and validation of the finite element approach

The need for a finite element model for computing the field map arises when the geometry is too complex to be modeled through analytical expressions. During the design process of the demonstrator magnet, this occurs when moving from the ideal coil, composed of straight grades only, to the curved one, where the analytical definition of all the arcs requires much handwork. The benefits that an analytical formulation would offer become therefore less important when compared to the ones of the finite element modeling. This latter not only allows the rapid definition of new geometries, but also lets the door open to create a multiphysics simulation tool in which electromagnetic and structural analyses can be coupled. For this reason, ANSYS APDL has been chosen as the finite element tool to address this task. The starting point of the FEM calculations is to validate the tools being used, and

this is done by comparing results with the analytical model on the latest geometry analyzed Fig. 7.2.

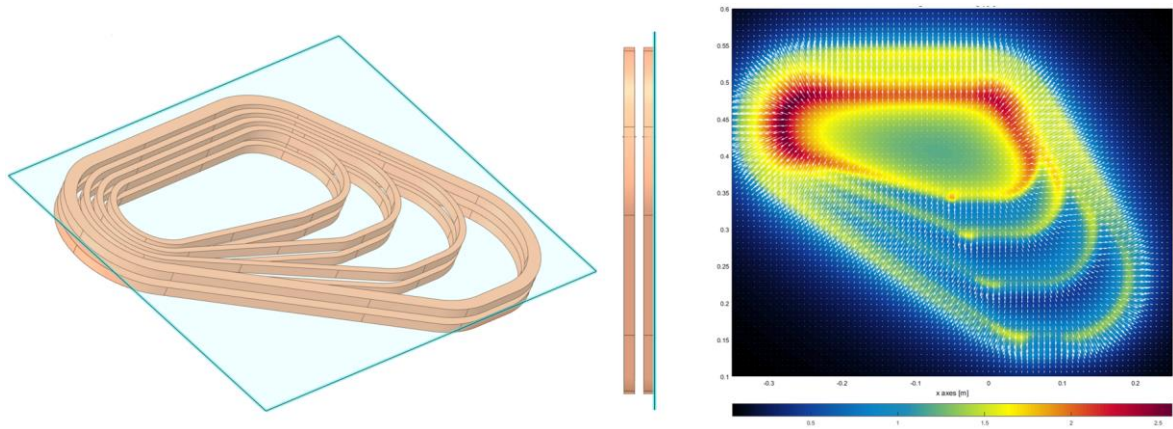


Fig. 7.2 – Schematization of the reference plane (left) on which the magnetic field map is presented (right).

Fig. 7.2 illustrates the coil's configuration, the position of a reference plane, and the calculated field map on such a plane. The field is represented using arrows to plot the local field direction and a color band to quantify the field intensity. By combining the two, the general field pattern can be understood, at least qualitatively.

It must be remarked that if the maximum field intensity is in the order of magnitude of the full-size proton gantry magnet, the shape of the field is much different. When isolated from the rest of the torus, a double pancake magnet acts similarly to a solenoid, though having a very low number of loops, and the field lines must turn around the magnet to close on themselves. In a toroidal situation instead, field lines would go round the torus, and since the magnetic reluctance is smaller near the internal radius, the field intensity tends to increase in this region, as showed in Fig. 2.2. The grades in this case lose their purpose of homogenizing the field intensity, and as we can see in Fig. 7.2, regions between the grades are characterized by significant field intensity reduction.

At this stage, the FEM simulations in ANSYS are meant only to evaluate if the results are qualitatively coherent to the analytic ones, namely in the order of magnitude of the field intensity and the direction of the field lines. Therefore, the accuracy of the model in terms of element shape and dimension has been chosen accordingly.

The first step in preparing a magnetostatic analysis is an electric simulation, that computes the current density distribution at each element inside the windings. Then the model is enclosed by the air volume of interest and the infinite boundary elements. The results of the two simulations, respectively the electric one and the magnetostatic one, are qualitatively represented in the Fig. 7.3 below.

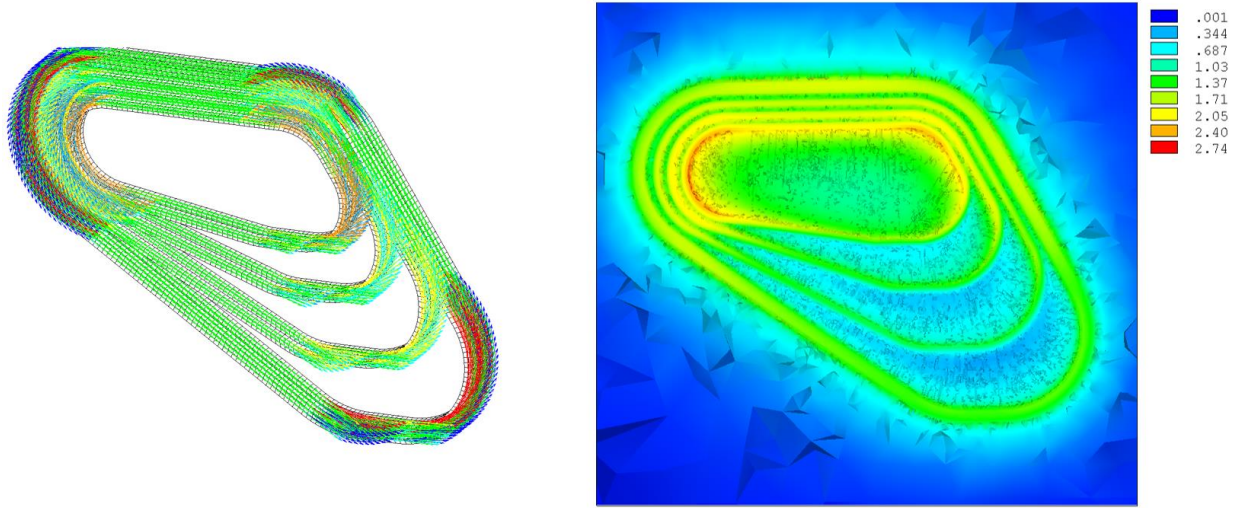


Fig. 7.3 – Vector plot of the current density distribution inside the windings (left) and resulting magnetic field map (B_z) on the reference plane (right). Flux density units: [T].

With a calculated peak field of 2.74 T on the reference plane, against the 2.6 T out of the analytic formulae, the error committed accounts for 5 %, which is within the threshold set for this model. Moreover, the post processing of these results shows complete adherence in terms of field lines directions, and the modeling technique is therefore considered validated.

7.2 Field calculations on the curved geometry

Having established the validity of the procedure, the calculations are then replicated on the curved coil. The modeling technique in this case requires much more care in the details of the mesh, since the purpose of these calculations is to provide finer results that will serve as the new reference field and force map.

Since the coils are identical and the whole problem can be considered symmetric, only one pancake layer is modeled, applying adequate boundary conditions on the symmetry plane. This is done by constraining the normal component of the magnetic vector potential \mathbf{A} to be zero on the symmetry plane. In more practical terms this means that the magnetic field lines are constrained to be perpendicular to the symmetry plane.

The discretization procedure is such that the model is entirely constituted of structured mesh, obtained by meshing planar surfaces and extruding them to obtain all hexahedrons, or at most wedges. Extruded elements are also enlarged by means of the bias option, that allows the definition of the ratio between the desired element size at the end of the extrusion and the original size. This reduces usage of computational resources, though covering a large air region is necessary for accurate results. The aspect ratio of the elements has been therefore controlled to never exceed 1:4, guaranteeing an ideal numerical approximation. Fig. 7.4 shows a portion of the magnetic model. In blue, cables can be distinguished from the dark grey-colored spacers, and white elements represent instead the surrounding air region. Around the air region, infinite boundary elements are employed as shown in Fig. 5.3.

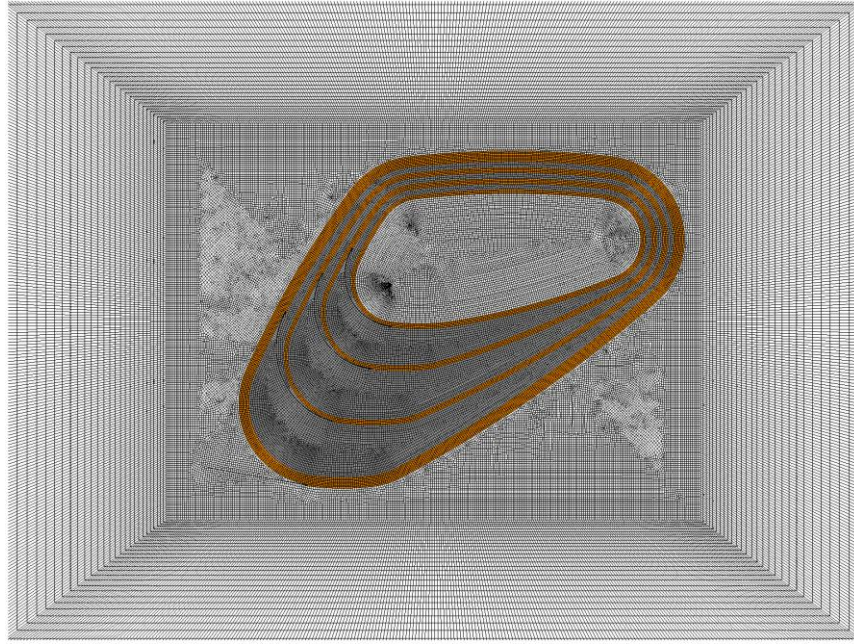


Fig. 7.4 – Visual representation of the discretized coils, spacers, and air regions.

The results of this model show higher accuracy already in the ANSYS post-processor. No singularities were present due to deformed elements, and the field map seems already very homogeneous with contained gradients.

However, by manipulating the results in Matlab, a much more understandable representation can be achieved in the format of a color band plot. The procedure involves significant mathematic manipulation, of which only the principles will now be presented. First, the results are obtained on a scattered grid of points, whose location in the plane is by no means regular, and it is dictated by the ANSYS mesher. These points are reported in fig. 7.5, colored depending on the field intensity at each location.

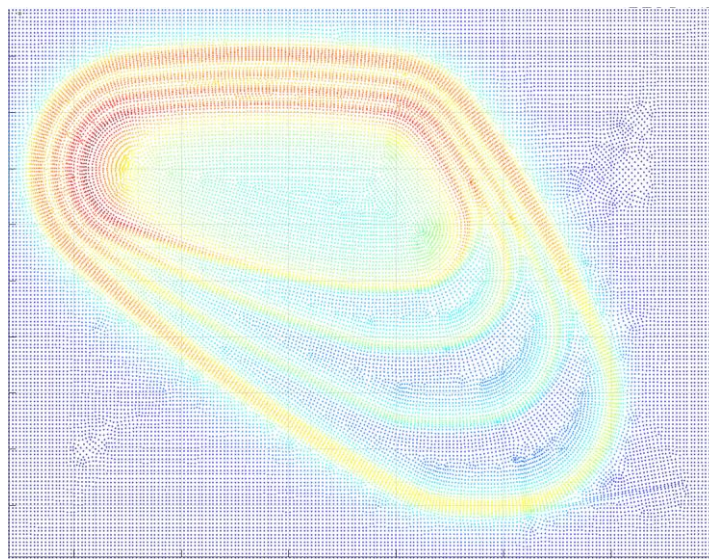


Fig. 7.5 – Color representation of the field intensity at discrete locations (nodes) resulting from FE calculations.

A grid of interest may be created in the plane coordinates x-y. This will range from x_{min} to x_{max} and from y_{min} to y_{max} in a discrete set on $N \times M$ increments, Δx , Δy . Then the field variables (B_x, B_y, B_z) can be approximated by a bi-cubic spline interpolation inside each grid element ($\Delta x, \Delta y$). With this numerical technique, two third degree-polynomials, in the variables x and y, are multiplied together and their coefficients are calculated imposing the passage of the curves through the datum points. Now, a combined color band-arrow plot can be produced, Fig.7.6, to qualitatively compare the new results with the previous ones from analytic calculations.

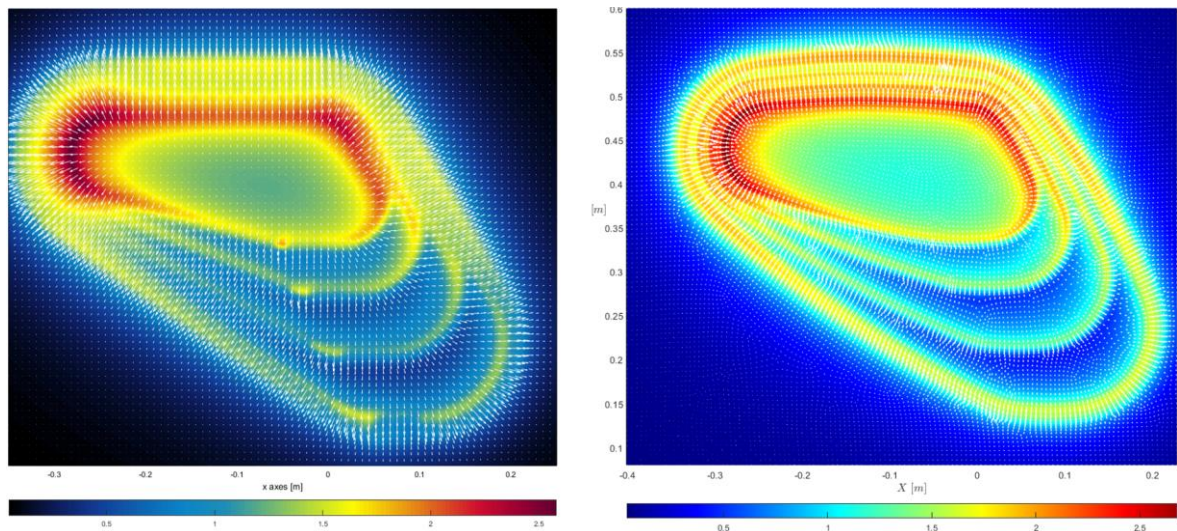


Fig. 7.6 – Visual comparison of the analytic field map (left) and the one resulting from FE calculations on curved grades windings (right). Flux density units: [T].

It must be remarked that in this case differences between the field intensity of the two models are expected, since the geometry has effectively changed. Therefore, these shall not be considered as errors but more likely as a deviation from the ideal field map. However, despite some minor differences that are characteristic of the coil geometry, it can be noticed how the two models are coherent in terms of field quality.

Another important output of these simulations, apart from the magnetic field itself, is the Lorentz forces map acting on the coils. These are fundamental for having a complete understanding of the magnet response during powering and therefore the must be calculated accurately.

Since the conductors are to form closed loops, the integral of equation 6.1 is closed in this calculation domain, and therefore equals zero. This means that the force system F_g acting on all coils should be equilibrated.

However, accumulated errors in numerical solutions always lead to relatively unprecise results. In this case, the in-plane component of the forces' sum differs from 0, with a magnitude of 45 N. On the other hand, if compared to the 109'100 N acting on a pancake layer in the out-of-plane direction, this forces unbalance accounts for the 0.04 % of the total forces. These values are considered unavoidable and are representative of a great accuracy of the FE model.

7.3 Field calculations with cable jumps

Finally one side of the magnet is considered, with the addition of grade jumps and a current outlet. The scope of this analysis is to quantitatively estimate the error committed when approximating the cables as if composed of grades only. Even though the expected differences are small, it is important to understand the deviation from the most accurate model when making different approximations.

As mentioned already in chapter 6, in this case the field perturbation is given by two factors. First, the jumps between grades are included, giving birth to the typical field distribution around the conducting wire. Secondly, the model accounts for the actual number of cables turns along each grade. It happens in fact that near the jumps, grades see a number of turns lower than the nominal one.

The colored field maps of the two models are presented in Fig. 7.7 for a visual comparison. Effects that can be immediately grasped in the Fig. to the right are due to the presence of a conductor making the current outlet, and some perturbations in the regions near the cable jumps. However, from a global perspective, the two maps seem identical both in peak values and in field quality.

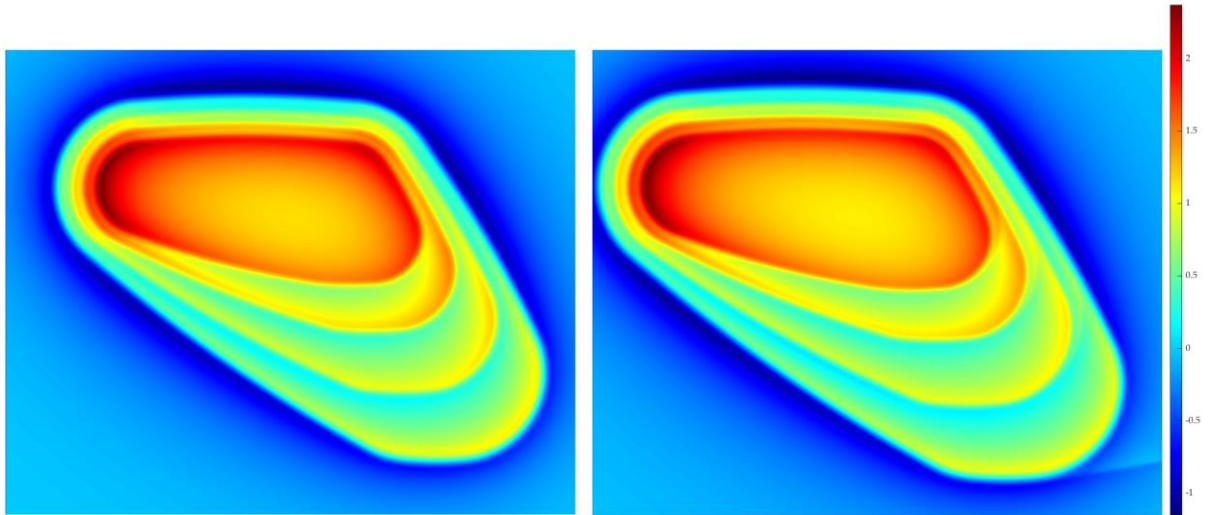


Fig. 7.7 - Visual comparison of the field map from FE calculation on curved grades windings (left) and the one including grade jumps (right). Flux density units: [T].

To have a more quantitative overview of the different results, the two maps can be overlapped and subtracted the one from the other. Fig. 7.8 reports the differences ΔB_z computed as

$$\Delta B_z = B_{z_c} - B_{z_j} \quad (7.1)$$

where B_{z_c} is the z-component of the magnetic field computed with curved grades only, and B_{z_j} is the one accounting also for the grade jumps.

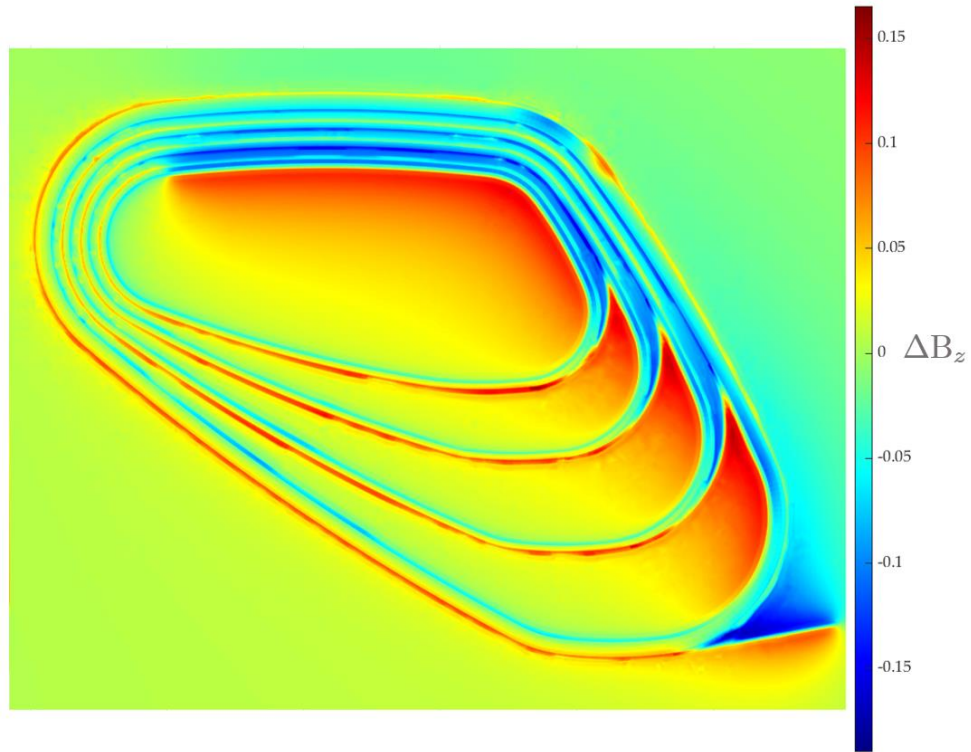


Fig. 7.8 – Colorband representation of ΔB_z . Units: [T].

With this convention the representation shows some significant evidence. Regions characterized by negative ΔB_z values (green to blue), are a sign of underestimated field intensity in z-direction. This can be easily understood considering the current outlet cable and applying the rule of the right hand. This effect replicates in the regions characterized by positive ΔB_z values (green to red), where the field is in fact overestimated. As it can be appreciated visually, this is mostly the case. The cause is mainly the fact that grades are not always composed of the nominal number of cable turns, and neglecting this fact leads to a maximum overestimation of approximately 0.158 T.

With the three models of Fig. 7.1 been analyzed a global comparison between them can be made. Once again, this can be interpreted as the result of various degrees of approximations, starting from straight grades, moving to curved ones, and finally adding the jumps.

Some values of engineering interest are extracted and presented in table 7.1.

The value of maximum field intensity developed on the cables by themselves is an important indication for quench protection studies. Together with the current density J and the temperature T , it defines the operating point of the superconductor as $\{T, J, B\}$. It is therefore interesting to note that the first two models, the ones without jumps, underestimate the peak field on the conductor by approximately the 7 %, which is a relatively significant error.

This error reflects also on the peak field developed in the whole domain and its component perpendicular to the reference plane, B_z . However, the differences now are less than 5 % in both cases.

Table 7.1 – Summary table of parameters of engineering interest calculated with different approximations.

Parameter		<i>Straight Cables</i>	<i>Curved (no jumps)</i>	<i>Final</i>
$ \mathbf{B} _{\max}$ on cables	[T]	2.89	2.87	3.09
$ \mathbf{B} _{\max}$	[T]	3.02	3.03	3.13
$B_{z_{\max}}$	[T]	2.97	3.00	3.10
F_x	[N]	80	20	680
F_y	[N]	130	40	550
F_z	[N]	101'500	109'100	104'500

Another important engineering aspect emerges when considering the forces. As mentioned earlier, the in-plane component of the total force acting on the windings must be null if considering closed-loop coils. Therefore F_x and F_y for the first two models should be zero, and the fact that they are not is due to numerical errors. On the other hand, the non-zero values for the third model are not sign of numerical imprecision, but really are the forces acting on the magnet. The resultant in the plane accounts for a significant value 875 N, therefore the design process must account for them, identifying some adequate components to withstand them.

7.4 Magnetic instrumentation positioning

Through the design process the geometry of the coil has been subjected to many changes, starting from the ideal one of Fig. 6.1, to the final one represented in Fig. 6.29. At this stage, it is of fundamental importance to assess the validity of the models through comparison with experimental results.

In this section we briefly describe the magnetic instrumentation that will be used during the cold tests of the demonstrator, and we explain the techniques adopted to find their best positioning scheme. The sensors that will be used are printed circuit boards (PCB), of which Fig. 7.9 offers a schematization.

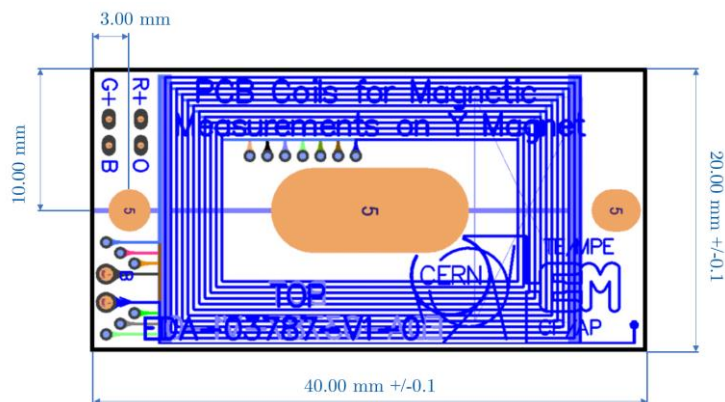


Fig. 7.9 – Schematization of the PCB used for the magnetic measurements on the demonstrator magnet during cold test.

The primary transducer comprises a set of 14 layers of coils, made of 17.5 μm thick copper wires, surrounded by two other layers with 35 μm thick copper coils. With this shape, the coils are sensitive to the magnetic flux variations over time. The goal is to produce a valuable signal during the discharging phase of the test. It is by integrating the voltage signal over time that we are able to retrieve the magnetic field intensity.

Moreover, to have a baseline to which we can compare the coils' signal, the PCB is predisposed to host a Hall probe in its central region (the one colored in orange in Fig. 7.9). This will work under static conditions, giving a voltage signal proportional to the field intensity.

It is necessary to find some suitable positions for the sensors, where the geometric tolerances and positioning inaccuracies would have a minor impact on the signal measured. Mathematically speaking, this coincides with regions where the gradient of the field component B_z is close to zero. For this purpose, 3D interactive plots of B_z over the region of interest have been produced in Matlab, of which Fig. 7.10 reports an extracted static image.

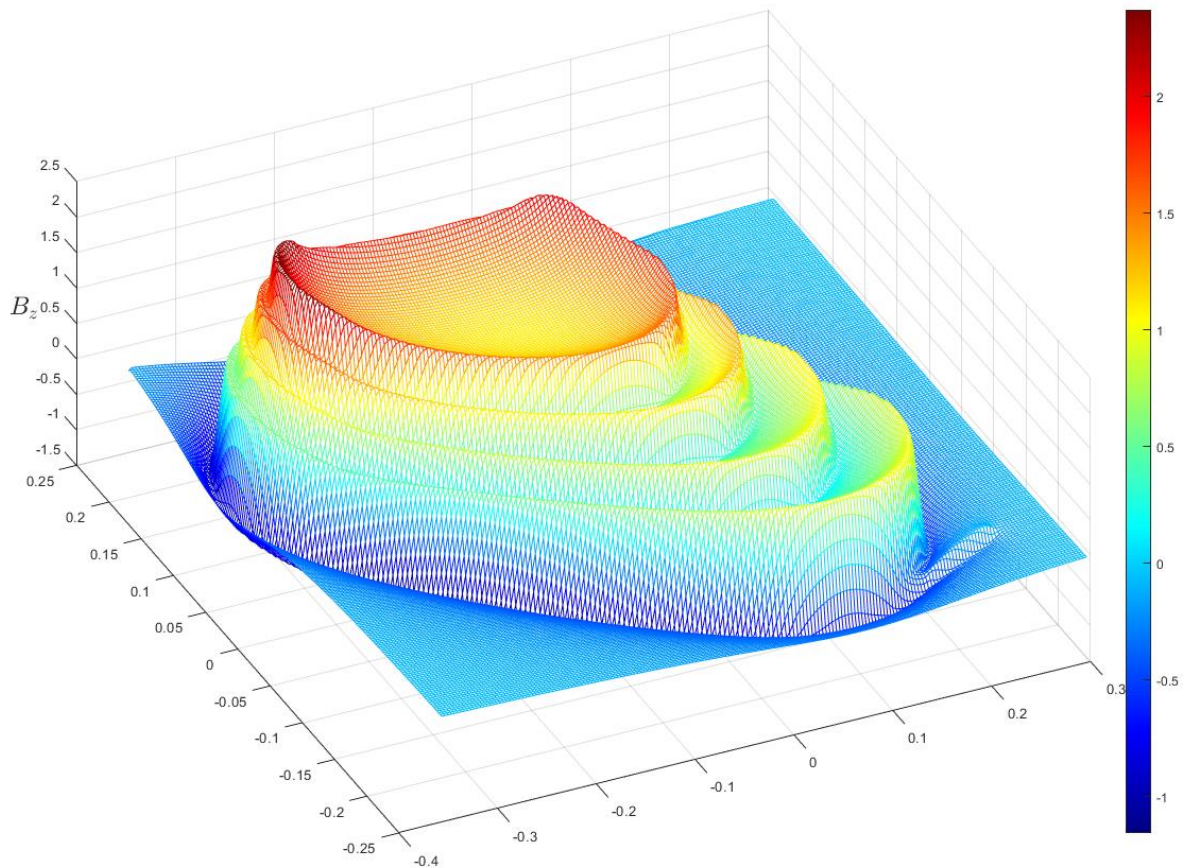


Fig. 7.10 – 3D representation of the B_z component over the reference plane. Units: [T].

By mean of this representation, the information about the field intensity and spatial gradients are offered at the same time, therefore making it easy to choose a position where the field intensity is sufficient and the gradients are low enough.

Another way of visualizing the component B_z over the reference plane is by means of the iso-intensity field lines, of which Fig. 7.11 gives an example.

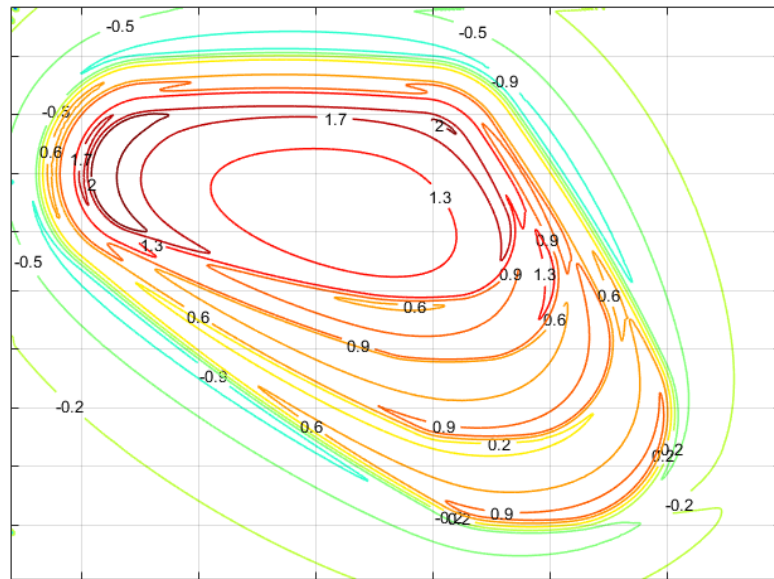


Fig. 7.11 – Color representation of iso-intensity field lines over the reference plane, and relative magnitude. Units: [T].

A first attempt of some suitable positions for five PCBs' has been defined. Some pockets to host the sensors have been modeled in the CAD environment, and some further results analyses have been done in Matlab, as shown in Fig. 7.12.

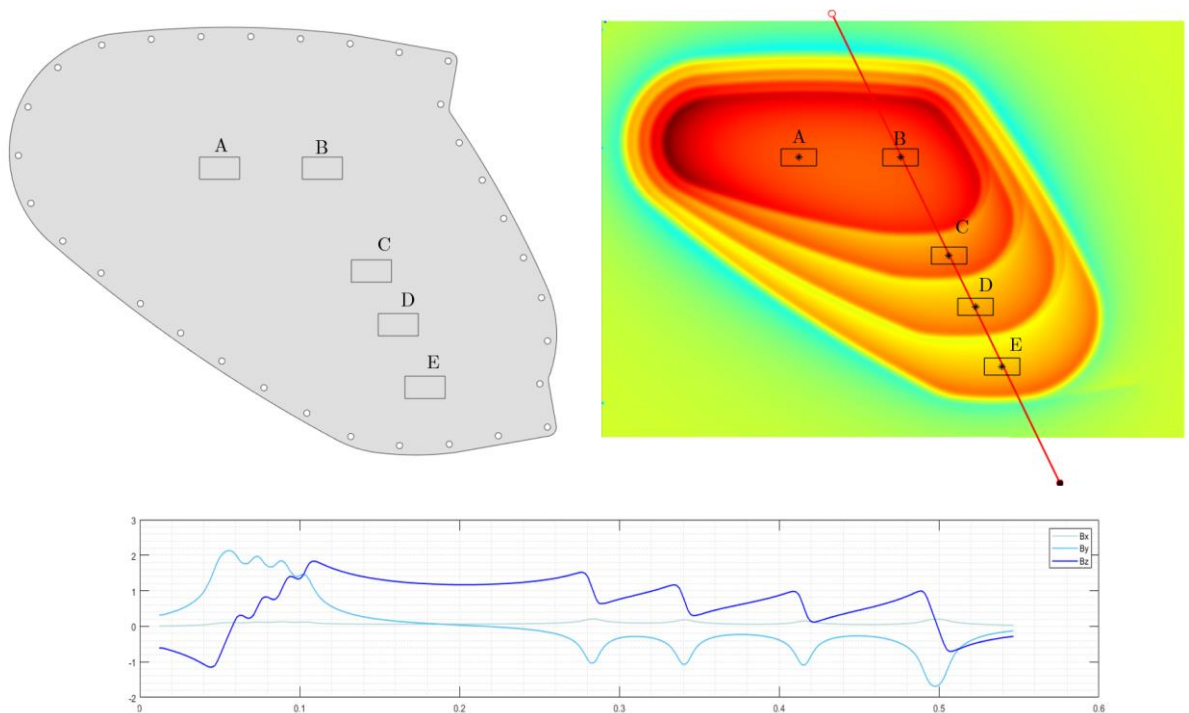


Fig. 7.12 – Preliminary positions of PCBs' and plot of the field components along a defined path. Units: [T].

The graph in Fig. 7.12 reports the trends of the field components B_x , B_y and B_z over the path defined by the red line, from the white point to the black one. As we can see, not only the gradient of B_z differs from zero in the positions C, D and E, but also there is a non-negligible presence of the in-plane components B_x , B_y . These components may significantly alter the measurement process, as the coils inside the PCB have a parasitic sensitivity for parallel field components, B_p .

To estimate the measured value of the perpendicular component of the field B_z , and the parallel field component B_p , numerical integration procedures can be led, computing the approximated values B_z and B_p as:

$$B_z = \frac{\phi}{A} = \frac{1}{A} \iint_{PCB} B_z \cdot dA \quad (7.2)$$

$$B_p = \frac{1}{A} \iint_{PCB} \sqrt{B_x^2 + B_y^2} \cdot dA \quad (7.3)$$

The calculated values are listed in table 7.2.

Table 7.2 – Results of the numerical integration procedures over the PCBs' regions.

Parameter	A	B	C	D	E
B_z [T]	1.165	1.188	0.935	0.672	0.549
B_p [T]	0.036	0.089	0.312	0.247	0.297

If values for PBCs A and B satisfy all the requirements, the parallel component for the rest of the PCB clearly shows some weaknesses. The expected B_p 's are of the same order of magnitude of the relative B_z , therefore efforts shall be put to limit as much this effect.

By manipulating the data, we can visualize regions where B_p is below a certain threshold, and by lowering the latter, the optimum position of the PCB centroids can be identified. Fig. 7.13 schematizes this procedure, showing both the optimal X-Y coordinates of each PCB, and the best inclination α in the plane.

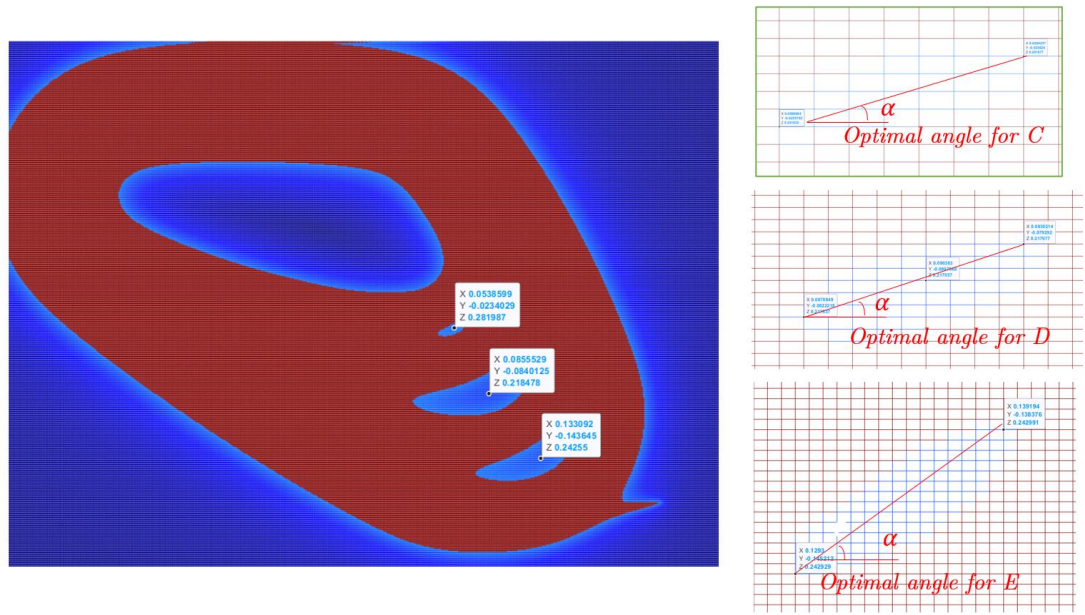


Fig. 7.13 – Visual representation of candidate regions to host the PCBs and relative inclinations.

Once these positions have been set, the grid must be rotated to perform once again the numerical integrations of eq. 7.2 and 7.3. This can be rapidly done by an adequate rotation matrix $[R]$ that allows to rotate the coordinate system in which data are read.

By referring to the original coordinates as \bar{x}_o , and the rotated ones as \bar{x}_n , the matrix operation that needs to be computed is:

$$\bar{x}_n = \bar{x}_o \cdot [R] = \bar{x}_o \cdot \begin{bmatrix} \cos(-\alpha) & \sin(-\alpha) \\ \sin(\alpha) & \cos(-\alpha) \end{bmatrix} \quad (7.4)$$

Fig. 7.14 gives a visual representation of the equation just described.

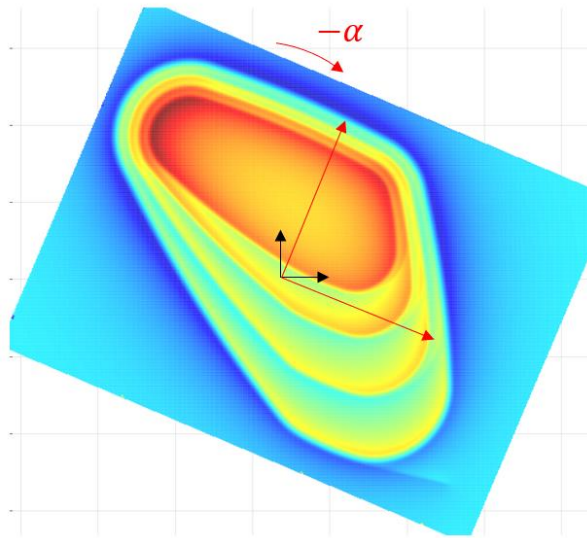


Fig. 7.14 – Visual representation of the rotation operation in expressed in Eq. 7.4.

The values of B_z and B_p can be integrated in these new positions and angles and table 7.3 gives a summary of the new results.

Table 7.3 – Summary table of new PCBs' positions and numerical integration results.

Parameter	A	B	C	D	E
X-position ¹⁰ [mm]	* ¹¹	*	53	90.5	135
Y-position [mm]	*	*	316.5	260	200
α [deg]	-	-	23	26	35
B_z [T]	1.16	1.12	0.94	0.70	0.47
B_p [T]	0.04	0.09	0.29	0.23	0.24

The benefits that this procedure has brought to the sensor's positioning can be grasped if comparing these values to the ones in table 7.2. For PCBs C, D, and E, the expected B_z has been increased, while the in-plane component B_p has been lowered as much as the field allowed to.

¹⁰ X and Y positions are to be considered in the CAD reference coordinate system.

¹¹ * These values remained unchanged.

Conclusions

The work done throughout the design process of the demonstrator magnet has brought to a final geometric configuration that is going to be manufactured in the short term.

Starting from an ideal coil, whose shape is driven by only functional requirements, geometric variations have been implemented to address different requirements, coming from the structural, the manufacturing and the operating necessities.

The new features have defined new boundary conditions to the finite element models with which the response of the magnet has been evaluated. The stress state assessment has evidenced the presence of possibly harmful phenomena for the integrity of the coil, and design changes have been suggested to mitigate such effects.

With this final geometry, electromagnetic analyses have been performed to evaluate the magnetic field quality, taking as a reference the desired field map for optimal beam delivery. Moreover, these calculations offered an assessment of the impact of different modeling approximations onto the field map, representing a reference for further decisions in electromagnetic modeling.

Finally, the field map has found direct practical application in the decision of the magnet sensor's positioning, and it will represent the reference map to which experimental measurements will be compared.

Bibliography

- [1] U. Linz, Ion beam therapy. Fundamentals, Technology, Clinical Applications, Berlin Heidelberg: Springer, 2012.
- [2] P. C. H. Becquerel, «Action physiologique des rayons du radium,» *C.R.T.* 132, pp. 1289-1291, 1901.
- [3] R. R. Wilson, «Radiological Use of Fast Protons,» *Radiology*, vol. 1, n. 47, pp. 487-491, 1946.
- [4] V. Marx, «Sharp shooters,» *Nature*, pp. 133-138, 2014.
- [5] «THE BRAGG PEAK,» Protom, proton therapy technologies, 18 June 2018. [Online]. Available: <https://www.protominternational.com/2018/06/bragg-peak/>.
- [6] W. R. Hendee, Proton and Carbon Ion Therapy, Boca Raton: CRC Press, 2013.
- [7] E. Rørvik, «A Comparison of Biological Dose Estimates in Proton and Carbon Ion Therapy Based on Averaged and Full Linear Energy Transfer Spectra,» Norwegian University of Science and Technology, Trondheim, 2015.
- [8] L. Leksell, «The stereotaxic method and radiosurgery of the brain,» *Acta Chir Scand*, vol. 1, n. 102, pp. 316-319, 1951.
- [9] C. D. e. Al., «Optimization of Carbon Ion Treatment Plans by Integrating Tissue Specific α/β -Values for Patients with Non-Resectable Pancreatic Cancer,» *PLOS one*, 2016.
- [10] U. L. H. Eickhoff, «Medical Applications of Accelerators,» *Reviews of Accelerator Science and Technology*, vol. 1, pp. 143-161, 2008.
- [11] P. George B. Coutrakon, «Accelerators for Heavy-charged particle Radiation Therapy,» *Technology in Cancer Research and Treatment*, pp. Volume 6, Number 4, August 2007.
- [12] «New Cyclotron Accelerator Technology that Provides Several Ion Species in a Short Time Period,» [Online]. Available: <https://rdreview.jaea.go.jp/tayu/ACT97E/03/0303.htm>.
- [13] [Online]. Available: <https://agenda.infn.it/event/6951/contributions/65186/attachments/47231/>.
- [14] H. U. Hospital, «Heidelberg Ion Beam Therapy Center,» Corporate Communication and Press Office, Heidelberg, 2012.
- [15] «Medizin & technik. Riesige Strahlenkanone beschießt Krebs,» 5 November 2012. [Online]. Available: <https://medizin-und-technik.industrie.de/medizin/news-medizin/riesige-strahlenkanone-beschiesst-krebs/>.
- [16] Y. I. e. Al., «Design of a superconducting rotating gantry for heavy-ion therapy,» *Physical Review Special Topics - Accelerators and Beam*, n. 15, 2012.
- [17] J. B. e. Al., «How many new cancer patients in Europe will require radiotherapy by 2025? An ESTRO-HERO analysis,» *Radiotherapy & Oncology*, vol. 119, n. 1, pp. 5-11, 2016.
- [18] «Particle Therapy Co-Operative Group,» [Online]. Available: <https://www.ptcog.ch/index.php/patient-statistics>.

- [19] «Directory of Radiotherapy Centres,» International Atomic Energy Agency, 28 02 2021. [Online]. Available: <https://dirac.iaea.org/Query/Map2?mapId=2>. [Consultato il giorno 19 03 2021].
- [20] E. Palmieri, «Applied Superconductivity,» CERN Academic Training Lectures, 17 January 2007. [Online]. Available: <http://cdsweb.cern.ch/record/986419/#>.
- [21] T. N. Prize, 21 September 2019. [Online]. Available: https://pbs.twimg.com/media/EFAAgBWWwAA_Ms5?format=jpg&name=large.
- [22] H. K. Onnes, «Commun. Phys. Lab. Univ. Leiden,» vol. 122b, May 1911.
- [23] OpenLearn, «Course on Superconductivity,» [Online]. Available: <https://www.open.edu/openlearn/science-maths-technology/engineering-technology/superconductivity/content-section-0?active-tab=content-tab>.
- [24] S. Prestemon, «Basics of superconductivity,» USPAS, Berkeley, 2015.
- [25] L. Bottura, «A Practical Fit for the Critical Surface of NbTi,» European Organization for Nuclear Research, Geneva, 1999.
- [26] M. N. Wilson, Superconducting Magnets, Claredon Press, 2010.
- [27] R. Prozov, «Equilibrium Topology of the Intermediate State in Type-I Superconductors of Different Shapes,» Ames Laboratory and Department of Physics & Astronomy, Iowa State University, July 2007. [Online]. Available: <https://www.researchgate.net/profile/Ruslan-Prozorov/publication/6161416/figure/fig1/AS:281024517951492@1444012874517/Structure-of-the-intermediate-state-in-a-disc-shaped-Pb-single-crystal-at-5-K-Left.png>.
- [28] J. v. Nugteren, High Temperature Superconductor Accelerator Magnets, Geneva: CERN Theses, 2016.
- [29] F. P. A. W. X. e. a. Wells, «Analysis of low-field isotropic vortex glass containing vortex groups in YBa₂Cu₃O_{7-x} thin films visualized by scanning SQUID microscopy,» *Nature, Scientific Reports*, vol. Sci Rep 5, n. <https://doi.org/10.1038/srep08677>, p. 8677, 2015.
- [30] L. Bottura, «Introduction to Accelerator Physics Superconducting Magnets,» 2012.
- [31] M. S. Barth, «Electro-Mechanical Properties of REBCO Coated Conductors from various Industrial Manufacturers at 77 K, self-field and 4.2 K, 19 T,» *Supercond. Sci. Technol.*, 2015.
- [32] THEVA, «THEVA PRO-LINE HTS WIRE,» Ismaning, 2020.
- [33] O. C. Zienkiewicz, «Generalization of the Finite Element Concepts - Weighted Residuals and Variational Approaches,» in *The Finite Element Method, 3rd Ed.*, London, McGraw Hill, 1977, pp. 42-91.
- [34] J. Szmelter, «The energy method of networks of arbitrary shape in problems of the theory of elasticity,» in *Proc. I.U.T.A.M., Symposium on Non-Homogeneity in Elasticity and Plasticity*, 1959.
- [35] O. C. Zienkiewicz, «Finite Elements of an elastic continuum,» in *The Finite Element Method, 3rd Ed.*, London, McGraw Hill, 1977, pp. 32-33.
- [36] O. C. Zienkiewicz, «'Standard' and 'hierarchical' element shape functions,» in *The Finite Element Method, Vol. 1, The basis*, Oxford, Butterworth Heinemann, 2000, pp. 168 - 177.

- [37] Y. Iwasa, *Case Studies in Superconducting Magnets*, New York: Springer, 2009.
- [38] N. A. D. e. Al., «Three dimensional finite element vector potential formulation of magnetic fields in electrical apparatus,» *IEEE Transactions on Power Apparatus Systems*, Vol. 1 di PAS-100, n. 8 August 1981.
- [39] Cryocomp, «Cryogenic properties,» v5.2, . [Online]. Available: <http://www.eckelsengineering.com/>.

List of Symbols

Symbols

n_0	Electron density of a target material
Z_{eff}	Effective charge of projectile ions
β	Relative velocity of projectile ions with respect to the speed of light
c	Speed of light
I	Mean ionization energy of target atoms
m_e	Mass of the electron
ω	Revolution frequency of a particle rotating in a uniform magnetic field
\mathbf{B}	Magnetic flux density
B	Magnitude of the magnetic flux density
q	Charge of a particle
m	Mass of a particle
f	Frequency of a particle rotating in a uniform magnetic field
p	Momentum of a particle
X-Y-Z	Reference cartesian coordinates
θ	Circumferential direction around the torus axis
α_e	Direction angle of a particle beam
ρ	Electrical resistivity of a material
T_c	Critical temperature
B_c	Critical magnetic field strength
λ	Penetration depth
\mathbf{J}	Current density
\mathbf{J}_c	Critical current density
ϕ_0	Quantum of magnetic flux
h	Planck's constant and is
e	Charge of the electron
\mathbf{u}	Unknown solution of a physical problem
\mathbf{F}	System of differential equations
\mathbf{B}	System of boundary conditions
$\partial\Omega$	Boundaries of a physical domain
\mathbf{a}^e	General finite set of variables
\mathbf{N}	Matrix of shape functions
ξ, η	Normalized coordinates inside a finite element
$l(\xi), (\eta)$	Lagrange polynomials for a finite element
\mathbf{K}	Stiffness matrix
\mathbf{f}	Vector of external loads

ϵ	Strain vector
\mathbf{D}	Elasticity matrix
σ	Stress vector
ϵ_0	Initial strains vector
σ_0	Initial stresses vector
\mathbf{k}^e	Elementary stiffness matrix
f^e	Vector of internal loads
\mathbf{H}	Magnetic field
\mathbf{A}	Magnetic vector potential
ν	Reluctivity diagonal matrix
\vec{f}_{mag}	Magnetic forces density
Φ	Circumferential direction around the torus axis
F_c	Centering force
F_ϕ	Fault force
I_q	Quenching current
E_{SS}	Young modulus of steel substrate
E_{Cu}	Young modulus of copper
E_{HTS}	Young modulus of ReBCO tapes
$\Delta L/L_{293}$	Relative contraction over temperature from 293 K
$\Delta x, \Delta y$	Numerical integration increments
ΔB_z	Magnetic flux differences
B_z	Integrated perpendicular component of the magnetic flux
B_p	Integrated parallel component of the magnetic flux

Subscripts and superscripts

ph	Phonon
res	Residual resistivity
c	Critical
0	Initial
e	Electron
e	Elementary
mag	Magnetic
c	Centering
Φ	Circumferential
q	Quenching
SS	Stainless steel
z	Perpendicular
p	Parallel

Abbreviations and acronyms

DNA	Deoxyribonucleic acid
SOBP	Spread Out Bragg Peak
LET	Linear Energy Transfer
RBE	Relative Biological Effectiveness
HIT	Heidelberg Ion-Beam Therapy Center
RFQ	Radiofrequency quadrupole accelerator
linac	Linear accelerator
RF	Radio frequency
HIMAC	Heavy Ion Medical Accelerator
MRI	Magnetic resonance imaging
LHC	Large Hadron Collider
EN	Engineering
MME	Mechanical and Material Engineering
EDS	Engineering Design and Simulation
TE	Technology
MSC	Magnets Superconductors and Cryostats
MDT	Magnet Design and Technology
HTS	High Temperature Superconductor
CTE	Coefficient of Thermal Expansion
RRR	Residual Resistivity Ratio
YBCO	Yttrium-Barium-Copper-Oxide
LTS	Low Temperature Superconductors
BCS	Bardeen, Cooper, Schrieffer
BSSCO	Bismuth Strontium Calcium Copper Oxide
REBCO	Rare-Earth-Barium-Copper-Oxide
NMR	Nuclear Magnetic Resonance
OHFC	Oxygen-Free-High-Thermal-Conductivity
FEM	Finite Element Method
m.v.p.	Magnetic vector potential
APDL	Ansys Parametric Design Language
PCB	Printed Circuit Board
CAD	Computer Aided Design

Appendix A

Table 1 – European treatment facilities in February 2021 [18].

Country	Where	Particle	Accelerator type* and max energy [MeV]	Begin of treatment
Austria	MedAustron	p	S 253	2016
	MedAustron	C-ion	S 403/u	2019
Belgium	Leuven	p	SC 235	2020
Czech Republic	Prague	p	C 230	2012
Denmark	Aarhus	p	C 250	2019
England	Clatterbridge	p	C 62	1989
	Newport	p	C 230	2018
	Manchester	p	C 250	2018
	Berkshire	p	C 230	2019
	Northumberland	p	C 230	2019
France	Nice	p	C65, SC 235	1991, 2016
	Orsay	p	SC 230	1991, 2014
	Caen	p	SC 230	2018
Germany	Berlin	p	C 250	1998
	Munich	p	C 250	2009
	Heidelberg	p	S 250	2009, 2012
	Heidelberg	C-ion	S 430/u	2009, 2012
	Essen	p	C 230	2013
	Dresden	p	C 230	2014
	Marburg	p	S 250	2015
	Marburg	C-ion	S 430/u	2015
Italy	Catania	p	C 60	2002
	CNAO, Pavia	p	S 250	2011
	CNAO, Pavia	C-ion	S 480/u	2012
	APSS, Trento	p	C 230	2014
Poland	Krakow	p	C 230	2011, 2016
Russia	Moscow	p	S 250	1969
	Dubna	p	C 200****	1999
	Saint-Petersburg	p	C 250	2018
	Obninsk	p	S 250	2016
	Dimitrovgrad	p	C 230	2019
Spain	Madrid	p	SC 230	2019
	Madrid	p	S 220	2020
Sweden	Uppsala	p	C 230	2015
Switzerland	Villigen	p	C 250	1984, 1996, 2013, 2018
The Netherlands	Groningen	p	C 230	2018
	Delft	p	C 250	2018
	Maastricht	p	SC 250	2019

Appendix B

Table A.2 – [1] List of clinical applications of proton therapy.

Ablative intent with single and hypofractionated therapy

- Pituitary tumors
- Arteriovenous malformations
- Vestibular schwannomas

Organ Preservation

- Choroidal melanoma

Dose escalation around critical structures with highly fractionated treatment

- Base of skull
- Prostate cancer
- Soft tissue and bone sarcomas
- Head and neck cancer

Reduction in morbidity and secondary malignancies

- Pediatric tumors

Investigational

- Low grade glioma
- Lung cancer
- Pancreatic adenocarcinoma
- Hepatocellular carcinoma
- Esophageal cancer
- Breast Cancer
- Lymphoma